Synthesis and Characterization of MOF-Derived Structures: Recent Advances and Future Perspectives

Link to publication record in Ulster University Research Portal

Document Version
Publisher's PDF, also known as Version of record

Synthesis and Characterization of MOF-Derived Structures: Recent Advances and Future Perspectives

Amir Farokh Payam,* Sameh Khalil, and Supriya Chakrabarti*

Due to their facile tunability, metal–organic frameworks (MOFs) are employed as precursors and templates to construct advanced functional materials with unique and desired chemical, physical, mechanical, and morphological properties. By tuning MOF precursor composition and manipulating conversion processes, various MOF-derived materials commonly known as MOF derivatives can be constructed. The possibility of controlled and predictable properties makes MOF derivatives a preferred choice for numerous advanced technological applications. The innovative synthetic designs besides the plethora of interdisciplinary characterization approaches applicable to MOF derivatives provide the opportunity to perform a myriad of experiments to explore the performance and offer key insight to develop the next generation of advanced materials. Though there are many published works of literature describing various synthesis and characterization techniques of MOF derivatives, it is still not clear how the synthesis mechanism works and what are the best techniques to characterize these materials to probe their properties accurately. In this review, the recent development in synthesis techniques and mechanisms for a variety of MOF derivates such as MOF-derived metal oxides, porous carbon, composites/hybrids, and sulfides is summarized. Furthermore, the details of characterization techniques and fundamental working principles are summarized to probe the structural, mechanical, physiochemical, electrochemical, and electronic properties of MOF and MOF derivatives. The future trends and some remaining challenges in the synthesis and characterization of MOF derivatives are also discussed.

1. Introduction

The metal–organic frameworks (MOFs), also recognized as porous coordination polymers (PCPs), are porous crystalline materials with infinite lattices synthesized by coordination chemistry using metal cations and polydentate organic ligands.[1–4]

A. F. Payam, S. Khalil, S. Chakrabarti
Nanotechnology and Integrated Bioengineering Centre (NIBEC)
School of Engineering
Ulster University
2–24 York Street, Belfast BT15 1AP, UK
E-mail: a.farokh-payam@ulster.ac.uk; s.chakrabarti@ulster.ac.uk

Easy tunability in MOFs structure can be attained via the selection of various combinations of metal cations and organic linkers and also by post-synthesis modification.[5] Ultrahigh porosity, high thermal stability, ability to tailor framework platform properties, and high surface area are the main characteristics of MOFs. As an example, MOFs possess ultrahigh Brunauer−Emmett−Teller (BET) surface areas up to $10\,000$ m^2 g^{-1}, which is much higher than zeolites and activated carbons.[6] After the discovery in the late 1990s by the groups of Robson,[7] Moore,[8] Yaghi,[9] Kitagawa,[10] and Férey[11]; MOFs were found to be promising due to their unique structure and have been widely investigated according to their structural properties and synthesis methods. In the last two decades, over $20\,000$ different MOFs in various structural forms like 1D, 2D, and 3D were synthesized[1] via an unlimited combination of metal and organic linkers to suit various specialized applications. Due to the flexible selectivity in structure, shape, modularity, and porosity, MOFs can be utilized in diverse applications including inter alia gas storage, energy conversion, chemical sensing, adsorption and desorption of gas molecules,[12] drug delivery,[13] optoelectronics,[14] catalysis,[15] proton conductivity, energy storage, food industry, and health care systems.[1–4,16,17]

Recently, MOF-derived porous structures have attracted much attention from research and the scientific community due to the ease of synthesis techniques and the possibility of tuning the properties of the derived porous structures to achieve improved performances in various applications. MOF-derived processing is a less complex synthesis method that can easily provide porous structured materials with controlled shape, size, phase, and physiochemical properties. For the synthesis of MOF-derived structures, MOFs are utilized as a precursor or template to provide a variety of porous structures. MOF can furnish different derivatives such as MOF-derived porous carbons,[18–20] metal, metal oxides, metal sulfides, metal phosphide,[21–29] and composites[30–60] with tuneable desired properties which are otherwise difficult to synthesize through other processes due to multistep complex processing. Because of the immense possibility of applications in a variety of advanced technologies, understanding the structural, mechanical,

physiochemical, electrochemical, and electronic properties of MOF and MOF-derived structures is equally important. The detailed understanding of these properties unfolds the possibility of further optimization of the derived structures suitable for desired applications. To investigate all the above-mentioned properties of complex structured MOFs and their derivatives, it is important to have a thorough understanding of various characterization techniques and the working principals of characterization instruments used for probing those properties. In this review, we concentrate on the current state-of-the-art methods for the synthesis and characterization of MOF-derived porous structures, describe their working principle, report recent findings, and discuss the current challenges that need systematic study to overcome.

2. Synthesis of MOF-Derived Materials

MOF derivatives have attracted significant attention in the areas of materials science research due to their excellent properties appropriate for diverse applications in energy, sensing, biomedical, catalytic, and food industry. So far, much literature has been published describing the MOF-derivatives synthesis process primarily governed by two techniques: heat treatment and chemical solution treatment. Recent studies indicate that MOFs are promising precursors or templates to produce nanoscale porous structures including MOF-derived oxides, carbides, nitrides, sulfides, phosphides, and composites with unique and predetermined properties. In this section, we will discuss various synthesis techniques of different MOF-derived structures.

2.1. Synthesis of MOF-Derived Porous Carbon

2.1.1. Direct Carbonization through Pyrolysis

MOF has been extensively used as a template to produce porous carbon using thermal (often between 600 and 1000 °C) treatment and chemical processing. This process is advantageous over other conventional nanocasting methods, as improved controllability in the pore size, and surface area can be achieved simply by controlling the temperature, time, heating rate, and annealing atmosphere. **Table 1** summarizes the synthesis parameters of various MOF-derived porous carbon structures. As shown in Table 1, same precursor (MOF-5) is used to obtain different porous carbon with varying surface area simply by changing the pyrolysis temperature, heating rate, and duration. By pyrolyzing MOF-5 in N_2 atmosphere at 900 °C for 1–5 h, BET surface area above 1500 $m^2 g^{-1}$[61–64] can be obtained in the derived porous carbon. The pyrolysis of the same MOF-5 precursor with additional precursor furfuryl alcohol can result in the formation of porous carbon with very high BET surface area close to 3000 $m^2 g^{-1}$.[65,66] This novel method was first proposed by Liu et al. in 2008[65] where zinc-based MOF (MOF-5) was selected in the first attempt to synthesize nanoporous carbon via MOF-templated method. MOF-5 has intrinsic properties for instance high surface area (2900 $m^2 g^{-1}$), calculated from Langmuir model, and very high pore volume (1.04 $cm^3 g^{-1}$),[67] both of which make it an appropriate self-sacrificial template for deriving porous carbons. Huang et al.[18] Bakhtiari et al.[68] and Xu et al.[69] reported successful syn-

thesis of nanoporous carbon using simple pyrolytic carbonization of MOF. Zhao et al. reported facile carbonization of MIL-88B-NH2 at different temperatures[70] for the synthesis of carbonized nanoparticles (CNPs-T) with ultrahigh surface area and ordered porous structure. These indicate the sustainable ability to synthesize porous carbon structures through direct carbonization of MOF precursors in simple steps.

2.1.2. Indirect Carbonization Using Additional Carbon Precursor

The synthesis of MOF-derived porous carbons is also possible with indirect carbonization[71] employing secondary precursors, e.g., ethylenediamine,[72] furfuryl alcohol,[65] and Glycerol.[73] The high surface area close to or above 3000 $m^2 g^{-1}$ can be attained in porous carbon synthesized by pyrolysis of MOFs in an inert atmosphere followed by chemical etching of surface metal ions. A novel example of this is the work by Jiang et al.[74] who employed zeolite-type MOF (ZIF-8) and furfuryl alcohol to synthesize nanoporous carbon and achieved an unexpectedly high BET surface area of 3405 $m^2 g^{-1}$. Another outstanding example is the work by Hu et al. who demonstrated the synthesis of nanostructured porous carbon with an even superior surface area (5500 $m^2 g^{-1}$) through the easy pyrolysis of Al-based MOF and successive acid removal of Al species.[75]. Xiaokun Pei et al.[76] summarized the synthesis and performance of MOF-derived porous carbons, porous carbons doped with heteroatoms, and porous carbons decorated with metal or metal oxide and discussed the effect of processing parameters e.g. temperature of calcination, supplementary precursor loading, and post-synthetic treatment on the properties of the resultant products.

2.1.3. Doped and Hybridized Porous Carbon

Porous carbon doped with heteroatoms (e.g., nitrogen (N), phosphorus (P), and/or sulfur (S)) can be synthesized using MOF as a precursor to enhance their functional performances like oxygen reduction reaction.[77,78] F. C. Zheng et al.[79] reported a simplistic strategy for fabricating microporous carbon polyhedrons with high-level nitrogen doping by simple pyrolysis of ZIF-8 polyhedrons at 500–900 °C in a nitrogen atmosphere. Li, Yang et al. reported the synthesis of N-doped carbon nanotubes by facile pyrolysis of Zn–Fe–ZIF at 900 °C in an N_2 atmosphere for 4 hrs and consequent acid leaching.[80] In 2014, Aijaz et al. synthesized N-decorated nanoporous carbons with high surface area employing ZIF-8 as a template and furfuryl alcohol as the secondary source of carbon besides NH_4OH as an extra nitrogen source.[81] These carbons exhibited remarkable CO_2 adsorption capacities and CO_2/N_2 and CO_2/CH_4 selectivity. The N-decoration in these carbons resulted in excellent activity for the oxygen reduction reaction.

There are reports of synthesizing porous carbons, metal-based compounds, and their hybrids to enhance the electrocatalytic performance[82–90] using transition metal (Fe, Co, Ni, Zn, etc.)-based MOFs as a precursor. As examples, Yin and co-authors described the synthesis of Co or nitrogen-doped porous carbon (Co Single atom/N–C) from Zn/Co–ZIF.[90] Hou et al. produced nanoparticles of Co-embedded N-doped porous carbon polyhedra by the pyrolysis of ZIF-67/GO composite.[91] These works

Table 1. Synthesis parameters of various MOF-derived porous carbons.

Obtained material	MOF precursor	Additional Precursor	Carbonization treatment conditions				S_{BET} [m² g⁻¹]	Reference
			Temp. [°C]	Gas	Heat rate	Duration		
3D porous carbon	MOF-5	–	900	N₂	5 °C min⁻¹	1 h	1880	[61]
HPCN	MOF-5	–	900	N₂	5 °C min⁻¹	3 h	1645	[62]
C-MOF-5	MOF-5		900	N₂	10 °C min⁻¹	5 h	1673	[63]
C-MOF-5	MOF-5	–	900	N₂	10 °C min⁻¹	5 h	1674	[64]
Mof-DC	MOF-5	–	1000	Ar	5 °C min⁻¹	8 h	2714	[72]
Porous carbon (1C)	MOF-5	–	1100	Ar	5 °C min⁻¹	8 h	1480	[92]
NPC	MOF-5	Furfuryl alcohol	1000	Ar	–	8 h	2872	[65]
NPC530	MOF-5	Furfuryl alcohol	530	Ar	–	8 h	3040	[66]
NPC650	MOF-5	Furfuryl alcohol	650	Ar	–	8 h	1521	[66]
NPC800	MOF-5	Furfuryl alcohol	800	Ar	–	8 h	1141	[66]
NPC900	MOF-5	Furfuryl alcohol	900	Ar	–	8 h	1647	[66]
NPC1000	MOF-5	Furfuryl alcohol	1000	Ar	–	8 h	2524	[66]
MC	MOF-5	–	600, 900	N₂	4 °C min⁻¹	6 h, 6 h	1812	[93]
MPC	MOF-5	Phenolic resin	600, 900	N₂	4 °C min⁻¹	4 h, 2 h	1543	[93]
MDC-1	IRMOF-1	–	900	N₂	5 °C min⁻¹	3 h	3174	[94]
MDC-3	IRMOF-3	–	900	N₂	5 °C min⁻¹	3 h	1678	[94]
MDC-8	IRMOF-8	–	900	N₂	5 °C min⁻¹	3 h	1978	[94]
WMC	MOF-5	Glycerol	1000	N₂	–	8 h	2587	[73]
C800	ZIF-8	Furfuryl alcohol	800	Ar	–	8 h	2169	[74]
C1000	ZIF-8	Furfuryl alcohol	1000	Ar	–	8 h	3405	[74]
MDC-1000	ZIF-8	–	1000	N₂	5 °C min⁻¹	5 h	1964	[95]
BF-1000	ZIF-8	Furfuryl alcohol	1000	N₂	3 °C min⁻¹	8 h	1067	[96]
BF-1100	ZIF-8	Furfuryl alcohol	1100	N₂	3 °C min⁻¹	8 h	1131	[96]
Nanoporous carbon	ZIF-67	–	800	N₂	5 °C min⁻¹	5 h	–	[97]
NPC@CNT	MOF-199	CNT	900	N₂	–	5 h	1370	[98]
CDM-6	MAF-6	–	800	N₂	5 °C min⁻¹	6 h	1642	[99]

HPCN: hierarchically porous carbon nanoplates, MOF-DC.: MOF-derived carbon, NPC: Nanoporous carbon, MDC: MOF-derived carbon, IRMOF: Isoreticular metal−organic frameworks, WMC: Worm-like mesoporous carbon, CNT.: Carbon nanotube, CDM: Carbon Derived framework, MOF-5 or IRMOF-1: $Zn_4O(BDC)_3$; BDC = 1,4-benzenedi-carboxylate), IRMOF-3: $Zn_4O(BDC-NH_2)_3$; BDC = benzenedicarboxylic), IRMOF-8: $Zn_4O(NDC)_3$; NDC = 2,6 naphthalenedicarboxylate), ZIF-8: (Zeolitic imidazolate framework-8 of Zn(MeIM)2; MeIM = 2-methylimidazole), ZIF-67: (Zeolitic imidazolate framework-67 of Co(MIM)2; MIM = 2-methylimidazole), MOF-199: (HKUST-1 Or Cu_3BTC_2; BTC = 1,3,5- benzenetricarboxylates), and MAF-6: (Metal-azolate frameworks with Zn(eim)₂; eim = 2-ethylimidazole).
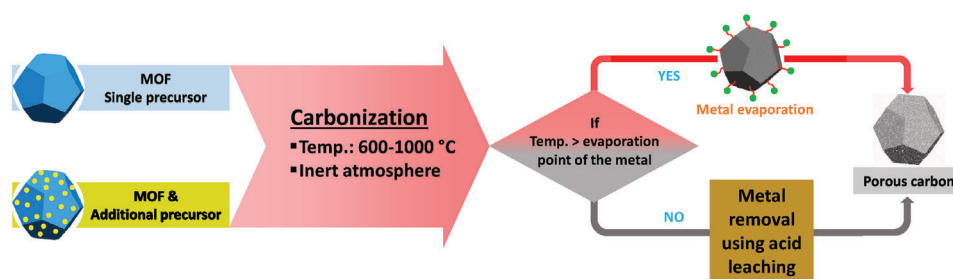
Figure 1. Schematic diagram of MOF-derived porous carbon synthesis process with improved controllability in the porous architecture, pore size, surface area, and composition.

are important as they demonstrated the successful synthesis of MOF-derived doped porous carbon with superior electrocatalytic and energy storage properties. Owing to the versatility of MOF structures and the flexibility of the process, MOF-derived porous carbon materials would significantly broaden the family of nanoporous carbon materials and provide new structures and multifunctional properties for use in electrocatalysts, sensors, supercapacitors, and batteries.

2.2. Synthesis Schemes for MOF-Derived Porous Carbon

MOF-derived porous carbon synthesis is mainly governed by two techniques, 1) Direct pyrolysis of MOFs and 2) Pyrolysis of MOFs encapsulating guest species.

2.2.1. Direct Pyrolysis of MOFs

The MOF precursors or templates have been typically carbonized under an inert (such as Ar, N_2) atmosphere followed by subsequent leaching of metal species to produce porous carbon structures with predefined properties. As a pioneering work, Jiang et al. synthesized porous carbons with a surface area as high as 3067 m^2 g^{-1}[74] by directly pyrolyzing ZIF-8. It has been observed that the introduction and polymerization of furfuryl alcohol into ZIF-8 MOF can improve the surface area (3405 m^2 g^{-1}) of resultant porous carbons. Following that Hu et al. synthesized nanoporous carbons with very high surface area (5500 m^2 g^{-1}) by the simple and direct pyrolysis technique.[75] **Figure 1** shows the synthesis scheme of MOF-derived porous carbon structures through direct pyrolysis of MOFs.
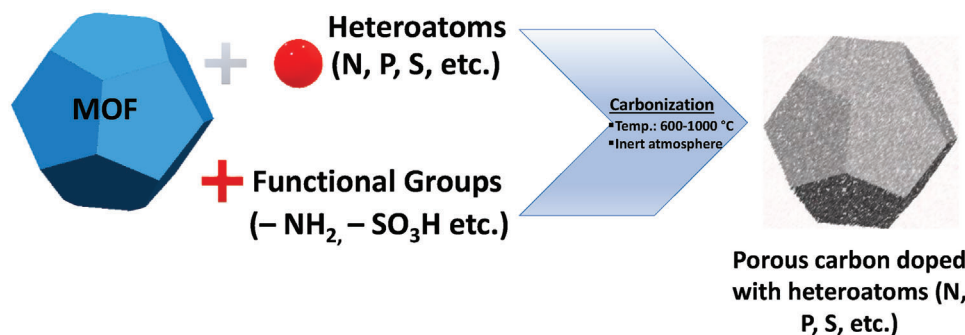
Importantly, porous carbon doped with various heteroatoms (N, P, S, etc.) can also be synthesized by direct pyrolysis of MOFs with heteroatom and functional groups ($-NH_2$, $-SO_3H$, etc.) as shown in **Figure 2**.

### 2.2.2. Pyrolysis of MOFs Encapsulating Guest Species

Another popular synthesis strategy to produce MOF-derived porous carbon nanoparticles is the inclusion of guest species into MOF pores accompanied by pyrolysis.[65,81,100–108] Pyrolysis of MOFs possibly will produce limited active sites, whereas the inclusion of guest species into MOF pores followed by pyrolysis provides the scope for synthesizing porous carbons with additional active sites useful for numerous energy storage, gas adsorption, and catalytic applications. Xu's group applied the pyrolysis of furfuryl alcohol-incorporated MOF-5 as an appropriate precursor[65] to synthesize porous carbons with a high surface area (2872 m^2 g^{-1}). Throughout the pyrolysis of MOF-5 under inert atmosphere, the produced ZnO species was decreased by carbon to generate evaporative Zn at high temperatures (>700 °C), providing highly porous carbon. Arshad et al.[81] described the synthesis of high surface area N-decorated nanoporous carbons employing the N-rich metal–organic framework ZIF-8 as a template and precursor along with furfuryl alcohol and NH_4OH as the secondary carbon and nitrogen sources, respectively.

2.3. Synthesis of MOF-Derived Porous Metal Oxides

Porous metal oxide with tuneable properties like shape, porosity, pore volume, and surface area can be synthesized by simple

Figure 2. Schematic of the synthesis process of MOF-derived porous carbon doped with heteroatoms.

ADVANCED
SCIENCE NEWS

www.advancedsciencenews.com

NANO · MICRO
small
www.small-journal.com
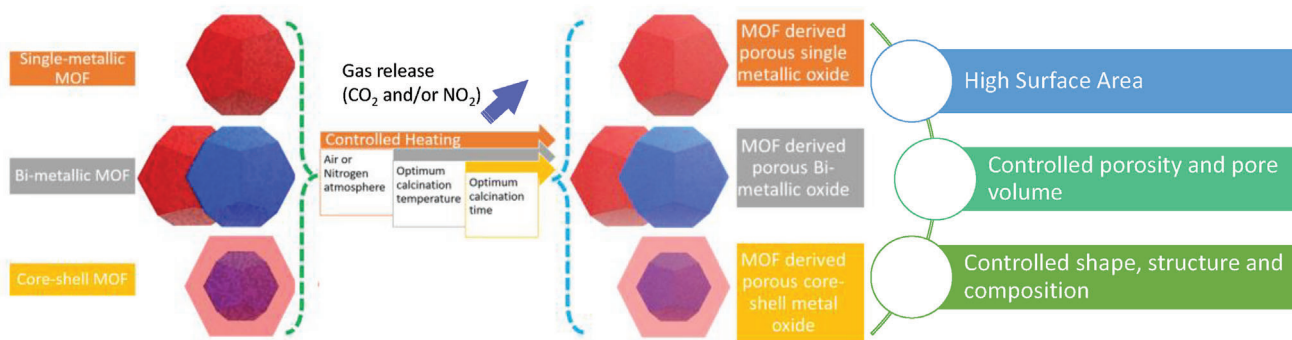
Figure 3. Schematic diagram of MOF-derived porous metal oxide synthesis process with tuneable properties like surface area, porosity, structure, and composition.

calcination of MOFs in air and/or nitrogen atmosphere (**Figure 3**). In comparison with other chemical and physical synthesis approaches, the synthesis of metal oxides using MOFs as a template has several benefits. MOF structure contains metal ions at the centers coordinated with organic linkers. Controlled oxidation of MOFs in air or nitrogen atmosphere causes the decomposition of organic linkers and releases CO_2 and NO_2 gases during heating to produce porous metal oxides. By optimizing the heating conditions and time, the original porous structure of parent MOF can be preserved in the derived metal oxide leading to high surface area and porosity.[71,109] Simply by adjusting annealing time and temperature, it is possible to achieve effective control over the composition, pore size, and surface area of MOF-derived metal oxides.[71,110] MOF template-based synthesis process provides flexibility in producing single- and bi-metallic metal oxides and/or core–shell metal oxides simply by choosing the single- and bi-metallic MOFs and/or combination of MOFs (Figure 3).

To date, various porous metal oxides with controlled properties have been synthesized using MOF as a sacrificial template via thermolysis.[76,124,125] Su et al.[127] synthesized porous Co_3O_4 hexagonal nanorings from MOF precursors and reported excellent lithium storage performance. Banerjee et al.[128] utilized controlled pyrolysis of Cu-based MOF (MOF-199) at 550°C in air for the synthesis of phase pure porous CuO spherical nanoparticles. Lei Zhang et al.[110] synthesized Fe_2O_3 microboxes with hierarchically structured shells by one-step annealing of Fe-based MOF (Prussian blue (PB)). They show a scalable synthesis strategy of anisotropic hollow structures of Fe_2O_3 with numerous architectures. X Xu et al.[111] used two-step calcination of iron-based metal–organic framework (MIL-88-Fe) template for the synthesis of spindle-like porous α-Fe_2O_3. Briefly, MIL-88-Fe was initially annealed at 500 °C in N_2 atmosphere to get black FeO_x-C composite and later calcined at 380 °C in air to obtain the dark red α-Fe_2O_3 (**Figure 4**) by removing residual carbon. MOFs can also be employed as templates to create a novel category of functional porous metal oxides.[112] As an example, Cho et al. reported the fabrication of numerous hollow and multi-ball-in-ball hybrid metal oxides using MOFs as a template and exploiting their distinctive reactivity and thermal behavior.[113]

S Maiti et al.[112] reported the growth of crystalline nanobar-like mesoporous Mn_2O_3 via a simple exo-templating of Mn-BTC MOF and using thermal calcination at 650 °C for 3 h, where the

MOF structure was preserved in the developed metal oxide with more voids and spaces. All these works show the versatility of the MOF calcination process to derive porous structured metal oxides of choice by selecting the right MOF as the starting precursor and the optimum calcination parameters.

Until now many works have been performed toward the synthesis of single and bi-metallic metal oxides with ultra-high surface area and porosity simply by one/two-step thermal
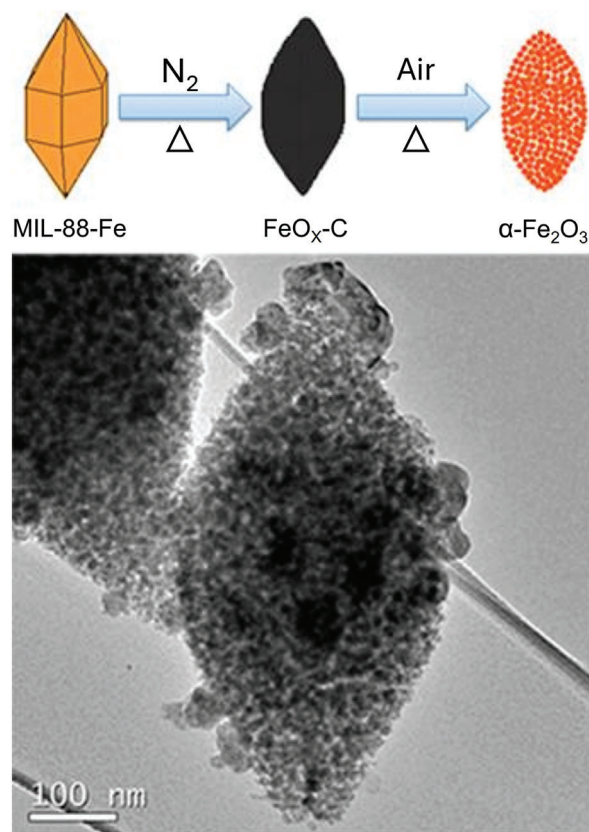
Figure 4. Top image shows the schematic diagram of the synthesis process and bottom image shows the transmission electron micrograph of synthesized spindle-like porous α-Fe_2O_3. Reproduced with permission.[111] Copyright 2012, American Chemical Society.
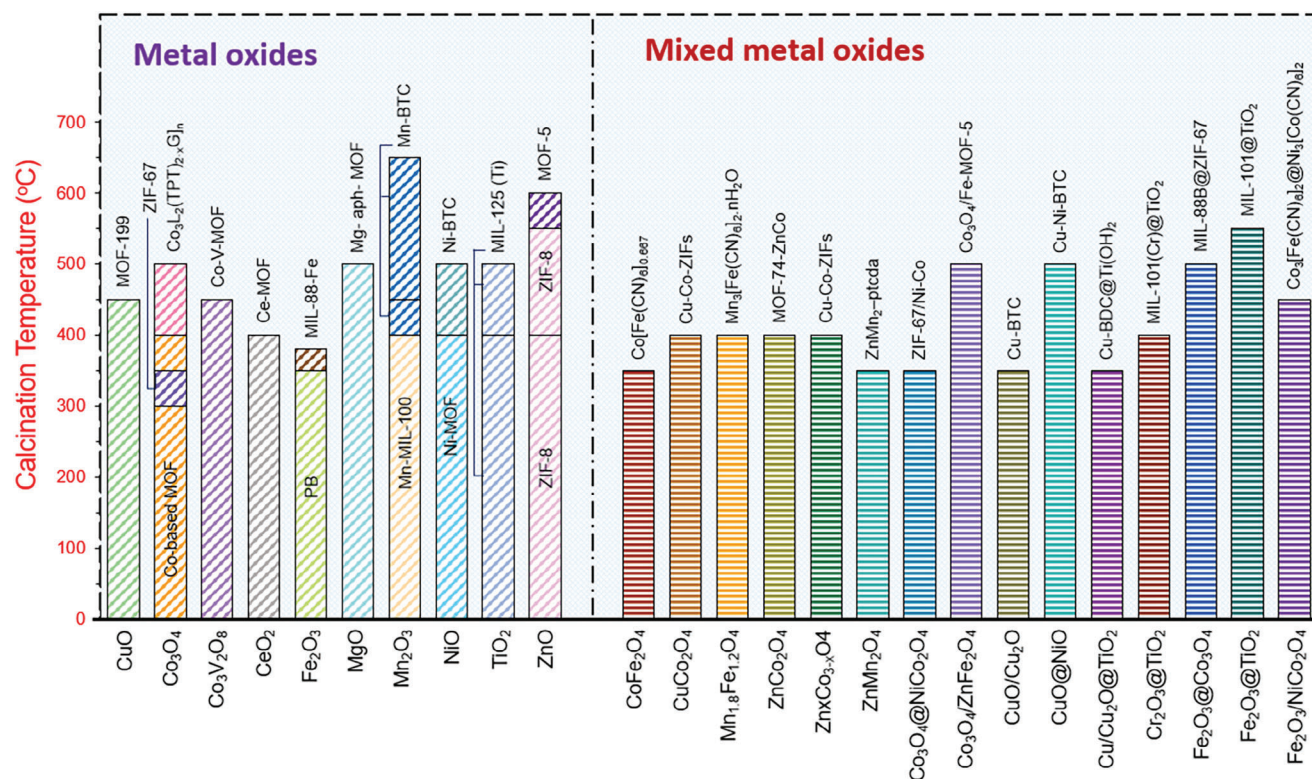
Figure 5. Bar graph demonstrating a diversity of MOF precursors that have been employed to produce metal oxide nanostructures (CuO,[115] Co_3O_4,[116–118] $Co_3V_2O_8$,[119] CeO_2,[120] Fe_2O_3,[110,111] MgO,[121] Mn_2O_3,[112,122,123] NiO,[124–126] TiO_2,[127–130] ZnO[131–133]) and nanocomposites (CoFe$_2$O$_4$,[134] CuCo$_2$O$_4$,[135] Mn$_{1.8}$Fe$_{1.2}$O$_4$,[136] ZnCo$_2$O$_4$,[137] ZnxCo$_{3-x}$O$_4$,[138] ZnMn$_2$O$_4$,[139] Co$_3$O$_4$@NiCo$_2$O$_4$,[140] Co$_3$O$_4$/ZnFe$_2$O$_4$,[141] CuO/Cu$_2$O,[142] CuO@NiO,[143] Cu/Cu$_2$O@TiO$_2$,[144] Cr$_2$O$_3$@TiO$_2$,[145] Fe$_2$O$_3$@TiO$_2$,[146] and Fe$_2$O$_3$/NiCo$_2$O$_4$[147]) as well as the calcination temperature to get the single and mixed metal oxide nano structures.

decomposition of MOFs as precursor or template, (**Figure 5**). Many examples of MOF-derived single and mixed metal oxide nanostructures are listed in Figure 5 and it gives a quick overview of the MOF precursor and calcination temperature requirement for getting desired metal oxides. Also, mixed metal oxides with complex structures can be easily synthesized through calcination of mixed metal MOFs which is otherwise difficult to obtain using other conventional physical and chemical synthesis processes. It can also be noted from Figure 5 that for single metal oxide formation the calcination temperature varies with the choice of MOF precursor. For example, Mn_2O_3 can be derived at 400 °C by calcination of the MOF precursor Mn-MIL-100 whereas it requires a much higher calcination temperature of ≈650 °C if the starting precursor is MN-BTC. Similar phenomenon is observed for other single metal oxides such as ZnO, TiO_2, NiO, Co_2O_3, and Fe_2O_3.

It is evident from the above studies that this MOF template-based synthesis is highly attractive and gives a large amount of flexibility and simplicity to achieve complex metal oxide structures with tuneable properties like controllable porosity, large surface area, morphology, and composition, which are advantageous for various practical applications. The synthesis parameters of some of the previously reported MOF-derived porous metal oxides are tabulated in **Table 2** which shows the MOF precursor, calcination parameters e.g., temperature, atmosphere, time and heating rate, morphology, and the BET surface area of the synthesized metal oxides. Close look at Table 2 reveals that there

is no direct correlation between the BET surface area of derived metal oxide and the calcination parameters as it varies randomly with the starting MOF precursor. However, annealing temperature of 500 °C in air with a heating rate of 5 °C m^{-1} is more favorable for synthesizing Co_3O_4 with a high BET surface area of 148 m^2 g^{-1}.[97] Similarly, for MOF-derived Fe_2O_3 the calcination temperature of 500 °C in air with a heating rate of 5 °C m^{-1} is most suitable to achieve a high BET surface area close to 100 m^2 g^{-1}.[114] Considering all results shown in Table 2, it can be inferred that a calcination temperature between 400 and 500 °C in air with a heating rate of 2 or 5 °C m^{-1} is most preferable for synthesizing MOF-derived metal oxides (Co_3O_4, TiO_2, Fe_2O_3, NiO, CeO_2, CuO, ZnO, and Mn_2O_3) with a high surface area close to or above 100 m^{2}g^{-1}.

2.4. Synthesis Schemes for MOF-Derived Porous Metal Oxides

MOFs can be tailored with diversified compositions and structures, which makes MOF derivation a promising and facile method to produce porous metal oxides. The elemental composition, morphologies, pore sizes, pore density, and surface area of MOF-derived metal oxides can be partially retained from MOF precursors and to a degree tailored by the prudent design of the MOF precursors and extrinsic control of the synthetic procedures, e.g., annealing temperature, time, heating atmosphere,

ADVANCED
SCIENCE NEWS
www.advancedsciencenews.com

NANO · MICRO
small
www.small-journal.com

Table 2. Synthesis parameters of various MOF-derived porous metal oxides.

Obtained material	Morphology	MOF used	Oxidation treatment conditions				S_{BET} [m² g⁻¹]	Reference
			Temp. [°C]	Gas	Heat rate	Duration		
Co_3O_4	Hexagonal nanorings	Co-NTCDA	500	Air	1 °C min⁻¹	1 h	20	[148]
Co_3O_4	Microsheets	Co-BDC	450	Air	5 °C min⁻¹	2 h	21	[149]
Co_3O_4	Hollow microfibers	Co–BTC	550	Air	2 °C min⁻¹	2 h	38	[150]
Co_3O_4	Hollow parallelepipeds	$Co_3(HCOO)_6$	400	Air	5 °C min⁻¹	3 h	43	[118]
Co_3O_4	Nanoparticles	$Co_3(abtc)_3(bpy)_{1.5}(H_2O)_3$	550	Ar	4 °C min⁻¹	3 h	47	[151]
Co_3O_4	Hollow dodecahedra	ZIF-67	350	N_2, Air	5 °C min⁻¹	0.5 h	54	[152]
Co_3O_4	Mesoporous nanostructured	Co-BDC	300	Air	10 °C min⁻¹	12 h	59	[153]
Co_3O_4	Concave nanoparticles	ZIF-67	350	Ar, Air	5 °C min⁻¹	3 h	61	[154]
Co_3O_4	Nanocages	$Co(MIM)_2$	300, 300	Ar, Air	2 °C min⁻¹	0.5 h, 2 h	110	[116]
Co_3O_4	Polyhedral shape	ZIF-67	500, 350	N2, Air	5 °C min⁻¹	0.5 h, 2 h	148	[97]
TiO_2	hierarchical porous anatase	MIL-125 (Ti)	400	Air	5 °C min⁻¹	4 h	147	[127]
SnO_2	SnO_2 nanomaterial	Sn-MOF	400	Air	5 °C min⁻¹	2 h	15	[155]
MgO	Nanoporous	Mg-aph-MOF	500	N_2	5 °C min⁻¹	12 h	200	[121]
α-Fe_2O_3	Mesoporous spindle-like	MIL-88-Fe	380	Air	5 °C min⁻¹	2 h	37	[111]
Fe_2O_3	Hierarchical microboxes	Prussian blue	350	Air	2 °C min⁻¹	6 h	52	[110]
α-Fe_2O_3	Mesoporous spindle-like	MIL-88-Fe	500, 380	N_2, Air	5 °C min⁻¹	1 h	75	[111]
Fe_2O_3	Yolk-Shell Octahedron	MIL-53(Fe)	500	Air	5 °C min⁻¹	0.5 h	93	[114]
NiO	Nanoparticle	$Ni_3(HCOO)_6$	400	Air	4 °C min⁻¹	3 h	34	[126]
CeO_2	Nanoporous	Ce-aph-MOF	500, 380	N_2, Air	5 °C min⁻¹, 1 °C min⁻¹	12 h, 2h	100	[121]
CeO_2	Hierarchical Dumbbell-like	Ce-BTC	RT	Air	–	2 h	205	[120]
CuO	Polyhedron	MOF-199	450	Air	1 °C min⁻¹	2 h	39	[115]
CuO	Hollow octahedra	Cu-BTC	300	N_2, Air	10 °C min⁻¹	0.5 h, 1 h	49	[156]
Mn_2O_3	hollow microspheres	Mn-BTC	450	Air	2 °C min⁻¹ / 5 °C min⁻¹ / 10 °C min⁻¹	2h	24 / 34 / 38	[123]
Mn_2O_3	Octahedrons	Mn-MIL-100	400	Air	5 °C min⁻¹	2 h	40	[122]
Mn_2O_3	Mesoporous nanobars	Mn-BTC	650	Air	2 °C min⁻¹	3 h	44	[112]
ZnO	hierarchical 3D cubic	MOF-5	600	Air	5 °C min⁻¹	3 h	11	[157]
ZnO	mesoporous structures	ZIF-8	450	Air	2 °C min⁻¹	4 h	579	[158]

Co-NTCDA: $(Co(NTCDA))_2$; NTCDA = 1,4,5,8-naphthalenetetracarboxylic dianhydride), $Co_3(abtc)_3(bpy)_{1.5}(H_2O)_3$: (CO-based MOF; abtc = azobenzene-3,5,4′ -tricarboxylic; bpy = 4,4′-bipyridine), MIL-125 (Ti): $Ti_8O_8(OH)_4(BDC)_6$, Sn-MOF: (formed by mixture of H_2O, $C_8H_6O_4$, NaOH, and $SnSO_4$), Mg-aph-MOF: (is a crystal of $[Mg_4(adipate)_4(DMA)- (H_2O)]5DMA-2MeOH-4H_2O$; aph = aliphatic ligand), MIL-88-Fe : $Fe_3O(H_2O)_2Cl(BDC)_3·nH_2O$, MIL-53(Fe): Fe(OH)BDC, Ce-aph-MOF: $Ce_2(adipate)_3·2DEF·5H_2O$; DEF = N,N-diethylformamide), Mn-MIL-100: $[Mn_3(O)(BTC)_2]·$.
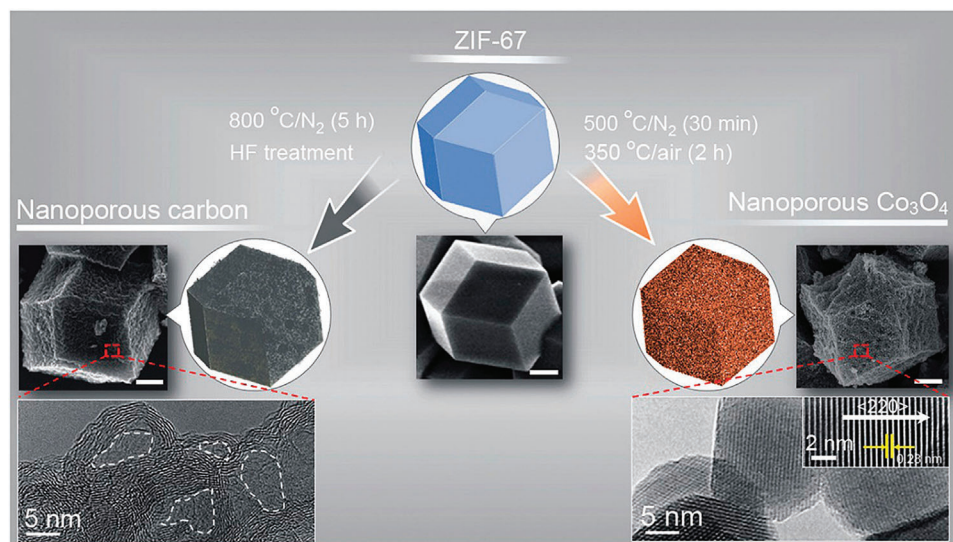
Figure 6. Schematic presentation showing the synthesis of nanoporous Co_3O_4 and carbon from ZIF-67 by optimized thermal treatment. The corresponding SEM and TEM images are shown below their illustrations. Reproduced with permission.[97] Copyright 2015, American Chemical Society.

and heating rate. Based on the experimental conditions the synthetic schemes of MOF-derived metal oxides can be classified into two types, 1) direct thermal decomposition of MOFs and 2) transformation of MOF by chemical solution reaction.

2.4.1. Direct Thermal Decomposition of MOFs

This is an effective and simple method to produce numerous porous metal oxides through direct pyrolysis of MOF precursors or templates. The composition, structure, and properties of MOF-derived oxides are highly dependent on the heating conditions such as temperature level, heating rate, gas atmosphere, and duration of heat treatment. These parameters are crucial parameters as these can alter the final product acquired through calcination of the same MOF precursor. For instance, CoO and Co_3O_4 are procured by calcination of the same MOF at 400 °C in different gas environments like N_2 and air, respectively.[159] Even at the same atmosphere, there is a possibility to obtain different MOF derivatives with different calcination temperatures. Therefore, the annealing temperature during heat treatment should be optimized to get the desired product of derivatives.[109,160] Salunkhe et al.[97] reported the selective synthesis of nanoporous carbon (at 800 °C) and nanoporous Co_3O_4 (at 500 °C) using ZIF-67 MOF just by changing the annealing conditions (**Figure 6**) and the porous structure of MOF precursor was somewhat retained. The selectivity of annealing atmosphere and temperature can significantly influence the final output even if the same MOF precursor is used as the starting material. The heating rate is another factor that affects the morphology, particle size, and the graphitization degree of carbon of MOF-derived material. Yang et al. reported that hierarchical ZnO/NiO microstructure can be obtained with different morphologies at a different ramping rate of the calcination process. As reported, the seaweed-like morphology consisting of a large number of nanosheets was achieved with a heat treatment rate of 5 °C min^{-1}, while aggregates composed of

nanoparticles were obtained at a heating rate of 1 °C min^{-1}.[161] Heat treatment conditions like temperature level, heating rate, gas atmosphere, and duration of heat treatment affect the decomposition mechanism of MOFs thus various derived structures can be obtained by varying these conditions.

2.4.2. Transformation of MOF by Chemical Solution Reaction

Instead of heating, MOF could also be transformed into different functional materials by chemical solution reaction treatment at room temperature.[162,163] During this process, MOF produces metal cations that react with liberated anions from other chemicals added to the solution. The dissolution process of MOFs could be affected by the MOF type, concentration, and pH value of the solution which will directly affect the dissolution rate. While rapid rate dissolution of the MOF could collapse the structure of the framework, a slow rate might lead to the coexistence of the MOF in the final derivatives.[164] The treatment of MOFs in a solution with suitable pH leads to the release of both the organic linker and metal cations.[152] The metal cations start to release gradually through the dissolution of MOFs by reacting with anions in the solution and forming a metal compound shell around the MOF surface. Then by manipulating the diffusion rate of ions by temperature and the concentration of the reactants, it is possible to control the morphology of MOF derivatives.[165] During this process, multiple elements can be combined into the MOF-derived material from a multi-metallic compound.[117] **Table 3** summarizes some MOF-derived metal oxides produced by solution-based chemical techniques.

2.5. Synthesis of MOF-Derived Nanocomposites/Hybrid Structures

MOFs precursors have a high potential for facile and efficient synthesis of different nanocomposites and/or hybrid

ADVANCED
SCIENCE NEWS
www.advancedsciencenews.com

NANO · MICRO
small
www.small-journal.com

Table 3. MOF-derived functional materials by solution-based technique.

| Obtained material	Precursor MOF	Solution reagents	Refs.
TiO$_2$	MIL-125 (Ti)	NaOH	[166]
CuO	Cu-BTC	NaOH	[162]
Gd-Si oxide mesoporous nanoparticles	Gd(H$_2$O)$_4$[Fe(CN)$_6$]	sodium silicate	[167]
Microporous silica	HKUST-1	HCl	[168]
Porous δ-MnO$_2$ nanoboxes	Mn$_3$[Co(CN)$_6$]$_2$·9H$_2$O	NaOH	[169]

porous structures. The formation of MOF-derived porous hybrids can be attributed to MOF decomposition for the formation of various void spaces in the crystal structure. By choosing the right combinations of MOFs and using an optimized heat treatment process, porous hybrid materials or nanocomposites with complex structures[113,143,170] can be synthesized. This scalable technique facilitates the production of various porous hybrids structures e.g. multi-shelled hollow spheres,[113] and cube-in-box hollow structures,[170] in simple ways which are otherwise difficult to achieve by other conventional physical or chemical synthetic methods. Some examples of MOF-derived hybrids formation are CuO/Cu$_2$O polyhedra,[142] CoFe$_2$O$_4$ nanocubes,[134] ZnO/ZnFe$_2$O$_4$/C octahedra,[171] and NiCo$_2$O$_4$/NiO dodecahedra.[172] Bi-component metal oxide hybrids,[143,147,170,173] such as NiO/Co$_3$O$_4$ hybrid spheres[113] and CuO@NiO,[143] can be synthesized effectively using MOFs as templates. Core–shell hybrid structures can be formed by core–shell MOFs as a template, which gives high flexibility in the formation of complex nano-hybrid structures compared to other conventional chemical synthesis techniques.

T. Wang et al.[132] described the process of seed-mediated growth by two-step calcination to synthesize porous ZnO@Co$_3$O$_4$ composites via the transformation of core-shell ZIF-8@ZIF-67 MOFs. Firstly the ZIF-8@ZIF-67 core-shell MOF in the form of lilac particles ($\approx$450 nm) was synthesized using the method developed by Y. Yamauchi et al.[174] After that, the lilac powder was heat treated in a tubular furnace at 400 °C for 2 h in N$_2$ to achieve the desired precursor for synthesizing ZnO@Co$_3$O$_4$ core–shell hybrid. Finally, the obtained precursor was annealed at 400 °C for 2 h in the air to obtain ZIF-8@ZIF-67 MOF-derived ZnO@Co$_3$O$_4$ hybrid (**Figure 7**).

2D MOF nanosheets can be used as a template for synthesizing porous hybrid 2D nanostructures. 2D MOFs nanosheets also known as 2D coordination polymers have attracted enormous attention due to their modular nature and tuneable structures, furthermore, these layered structures have fascinating topological networks and entanglements. 2D MOFs nanosheets can be synthesized using two different methods and those are 1) top-down stratification strategy and 2) bottom-up method or the combination of two methods. Some examples of 2D MOF nanosheets are 2D metal–porphyrin MOF nanosheets and 2D NiCo bimetallic MOF nanosheets. MOF-derived ultrathin sheet-like 2D hybrids can be formed via the thermal processing of MOF thin films coated on a graphene template accompanied with acid wash for the removal of metallic ions.[175] Easy replacement of metal ions in 2D MOF nanosheets facilitates the formation of more complex MOF nanosheets which can be utilized as a precursor to synthesize MOF-derived 2D hybrid structures with tuneable structure and composition.

Carbon nanocomposites and metal oxides hybrids with different morphologies, compositions, and functionalities can be synthesized using MOFs as precursors or templates. Chen et al.[176] synthesized a core-shell type hybrid i.e. graphene sheet supported porous nano box structured nitrogen-doped Fe/Fe3C@C via thermal processing of graphene oxide-supported iron-based MOF Prussian blue. By directly pyrolyzing MOFs under an inert atmosphere and excluding the metal removal steps, one can produce multi-component hybrid structures, e.g., carbon-metal, carbon-metal oxides, and numerous metal-based hybrids. For
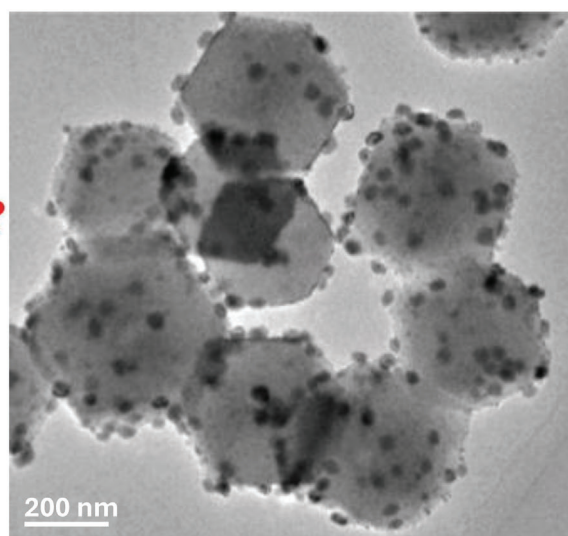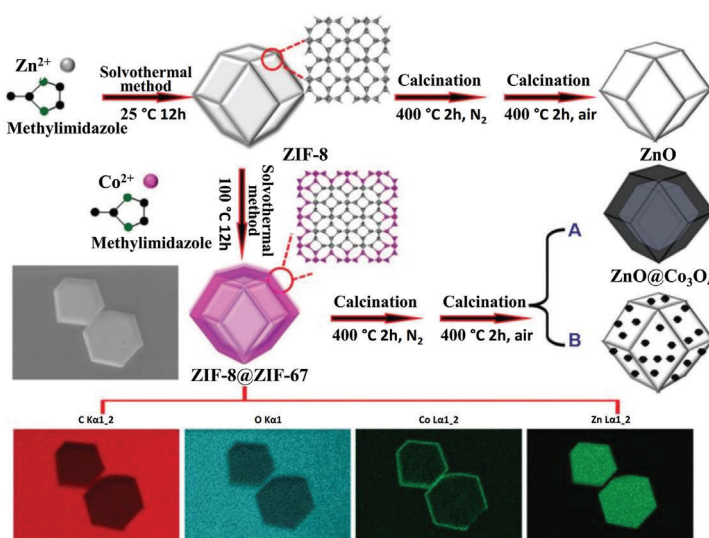
Figure 7. Left image shows the schematic presentation of the formation of ZnO@Co$_3$O$_4$ hybrid using ZIF-8@ZIF-67 MOF as precursor along with SEM elemental mapping of C, O, Co, and Zn; the right image shows the TEM image of ZnO@Co$_3$O$_4$ hybrid. Reproduced with permission.[132] Copyright 2016, The Royal Society of Chemistry.

**ADVANCED
SCIENCE NEWS**

www.advancedsciencenews.com

NANO · MICRO

small

www.small-journal.com

example, Wei et al. reported pyrolysis of HKUST-1 MOF under N_2 atmosphere to synthesize anthill-like Cu@C hybrid materials with preserved octahedral morphology.[177] Long et al. utilized hetero-dinuclear MOFs[41] as a template and created a simple method to synthesize a porous hybrid of nitrogen-doped graphene implanted with transition metal alloy nanoparticles. Using simple thermal processing researchers have demonstrated the fabrication of precious metal, metal oxide, and carbon hybrids such as Au/ZnO[178] and Co_3O_4/GN,[179] C–N-doped ZnO,[180] and Fe_2O_3/C.[181] Recently, Chen et al. proposed the synthesis of a metal oxide@carbon core–shell-type hybrid using direct pyrolysis of a hollow ZIF-67@ZIF-8 matrix under an inert atmosphere.[182] The attained ZnO@C–N–Co has been constructed with uniform ZnO particles as the core and N-doped graphitized carbon embedded with Co NPs as the shell layer. The pyrolysis temperature was very important for the formation of ZnO@C–N–Co with ZnO as the core of the structure.

Furthermore, recent reports indicate the possibility of producing numerous MOF-derived three or more components hybrids, such as ZnO/$ZnFe_2O_4$/C hollow structured hybrid octahedra,[171] core–shell structured ZnO/$ZnCo_2O_4$/C hybrids,[183] and yolk–shell structured ZnO/$Ni_3ZnC_{0.7}$/C hybrid microspheres.[184] Li et al.[185] demonstrated multi-step synthesis of a four-component MOF-derived hybrid structure where the components are reduced graphene oxide (rGO) sheets, polyhedral structured carbon, Co nanoparticles, and sulfur. All these reports demonstrate the versatility of the MOF-derived synthesis process to produce complex hybrid structures with customized structure, composition, and morphology. The synthesis parameters of some of the previously reported MOF-derived porous hybrid structures are tabulated in **Table 4**. A quick overview of MOF precursors and heating parameters for the synthesis of MOF-derived hybrid structures can be seen in Table 4, which also indicates various applications of these hybrids in supercapacitors, batteries, and catalysis.

2.6. Synthesis Schemes for MOF-Derived Hybrids/Nanocomposites

MOF-derived hybrids synthesis is primarily governed by three preparation methods: 1) Thermal processing of MOFs with predesigned composition and morphology; 2) thermal processing of hybridized MOFs with other materials; and 3) thermal processing and post-treatment of MOFs for obtaining the desired hybrid structures. **Figure 8**[209] shows the schematic illustration of MOF-derived hybrid synthesis strategies.

2.6.1. Thermal Processing of MOFs with Predesigned Composition and Morphology

Predesigned MOFs can be heat treated at optimum conditions to get control over the structures and physio-chemical properties of derived hybrid structures. After the heating process, MOFs have been converted to a combination of carbon, metal oxides, and/or metal carbides leading to the formation of hybrids with pre-designed features. MOFs with pre-designed compositions and morphologies can be synthesized

by various techniques like the cation exchange process,[113,143] hydro/solvothermal process,[172,183] and self-assembly.[210] Easy thermal processing of these predesigned MOFs results in the growth of various multi-component MOF-derived hybrid structures. As an example, octahedron structured ZnO/$ZnFe_2O_4$/C hybrid with a porous shell has been synthesized using a direct heating procedure of predesigned Fe-doped MOF-5 crystals under N_2 atmosphere.[171] A similar synthetic scheme was used to produce ZnO/$Ni_3ZnC_{0.7}$/C hybrid microspheres using predesigned Ni-doped Zn–MOFs.[184] By altering the reaction conditions of the MOF preparation technique, other morphologies such as core-shell type hybrids can also be synthesized. For example, CuO@NiO microsphere hybrid with three-layer ball-in-ball hollow morphology was synthesized through simple pyrolysis of Cu–Ni bimetallic organic frameworks.[143] Various other multi-shell type structures of metal oxides such as CuO-ZnO, NiO/Co_3O_4, and Co_3O_4/ZnO hybrid microspheres were synthesized through similar cation exchange reactions of Co-, Ni-, or Zn-based MOFs followed by calcination.[113] This synthesis scheme can be applied for the preparation of other mixed metal oxides hollow porous hybrid structures using predesigned bimetallic MOF crystals.

2.6.2. Thermal Processing of Hybridized MOFs with Other Materials

So far, there are plenty of reports of growing many hybridized MOFs, e.g., MOF hybridized with carbon[175,176,191] and metal oxides[147,197] through different synthesis methods which include template-supported methods,[173,175,196,199] ball-milling,[211] and small molecules incorporation into the MOFs pores.[212] These hybridized MOFs can be used as precursors for the formation of various MOF-derived hybrids with desirable properties. MOF–carbon hybridized nanostructure enables the synthesis of derived hybrids with varied morphologies, porosity, and improved electrical properties which are promising for a wide range of applications in energy storage devices.[196,199] A similar synthetic strategy can be employed for a number of MOF-derived hybrid structures using different MOFs and carbon materials as building blocks.

Furthermore, the in situ growth of MOFs on their ascribed metal compound structures is another promising approach to simplify the formation of MOF-derived hybrids.[173] For example, the formation of a ZnO quantum dot-carbon-ZnO nanorod core-shell structured hybrid can be possible through the thermal processing of ZIF-8-coated ZnO nanorod.[197] Here ZIF-8 was in situ grown on the ZnO nanorod surface and the ZnO nanorod acted as substrate as well as the precursor for the growth of ZIF-8. The advantage is that using this process the characteristics like composition, structure, and morphology of MOF-derived hybrids can be well predicted by controlling the features of MOF hybrid precursors. This synthesis technique furnishes a controllable and viable approach to obtaining MOF-derived hybrids with essential properties.

2.6.3. Thermal Processing and Posttreatment of MOFs

Simple thermal processing and posttreatment of MOFs can result in the formation of MOF-derived hybrid structures, in which

Table 4. Synthesis parameters of various MOF-derived porous hybrid structures.
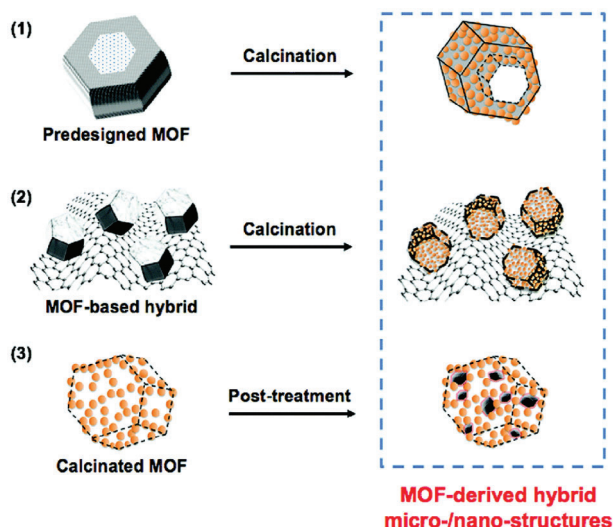
Hybrid-structure obtained	MOF used	Heating parameters				Post-treatment	Application	Reference
		Temp. [°C]	Gas	Heat rate	Duration			
2D CoSNC	(PPF-3) MOF	650	Ar	5 °C min⁻¹	5 h	–	Supercapacitor	[186]
ZnCo$_2$O$_4$	JUC-155	400	Air	2 °C min⁻¹	2 h	–	supercapacitors	[187]
Fe$_3$O$_4$/C	Fe-MIL-88B NH$_2$	500	N$_2$	5 °C min⁻¹	1 h	–	Supercapacitors	[188]
Cr$_2$O$_3$/C$_{900}$	MIL-101(Cr)	900	Ar	–	6 h	–	Supercapacitors	[189]
NiO/ZnO	Ni-Zn-BDC	500	Air	1 °C min⁻¹	20 min	–	Supercapacitors	[190]
Co$_3$O$_4$/ZnFe$_2$O$_4$	Fe^{III}-MOF-5	500	Air	1 °C min⁻¹	2 h	–	supercapacitor	[141]
rGO-Wrapped MoO$_3$	Mo-imidazole	600, 340	Ar Air	3 °C min⁻¹, 5 °C min⁻¹	3 h, 2 h	–	Supercapacitor	[191]
NiCo$_2$O$_4$/Co$_3$O$_4$	ZIF-67 coated on Co$_3$O$_4$ & Ni(NO3)2	300	Air	3 °C min⁻¹	3 h	–	Supercapacitor	[173]
Co$_3$O$_4$/ZnO	ZIF-8@ZIF-67	500, 350	N$_2$ Air	3 °C min⁻¹	1 h	–	supercapacitors	[192]
CuO@NiO	Cu-Ni-BTC	500	Air	5 °C min⁻¹	2 h	–	LIB	[143]
Sulfer/carbon	ZIF-8	1000	N$_2$	2 °C min⁻¹	8 h	Sulphur embedding	LIB	[193]
Carbon/ZnO QD	IRMOF-1	550	N$_2$	10 °C min⁻¹	–	–	LIB	[194]
ZnO/ZnFe2O4/C	Fe-doped MOF-5	500	N$_2$	1 °C min⁻¹	–	–	LIB	[171]
ZnO/Ni$_3$ZnC0$_{.7}$/C	ZN-BTC	450	Ar	1 °C min⁻¹	2 h	–	LIB	[184]
ZnO/ZnCo$_2$O$_4$/C	ZnCo-BDC	400	N$_2$	–	2 h	–	LIB	[183]
NiCo$_2$O$_4$/NiO	ZIF-67 & Nickel	400	Air	2 °C min⁻¹	1 h	–	LIB	[172]
β-NiS NP-porous carbon	MOF-74 (Ni)	400	Ar & H$_2$	10 °C min⁻¹	5 h	Sulphur embedding	LIB	[195]
ZnO or Co$_3$O$_4$, Ni foam/Carbon fiber	Zn or Co-MIM	300	Air	1 °C min⁻¹	1 h	–	LIB	[196]
ZnO@ZnO Quantum Dots/C	ZIF-8 & carbon cloth	650	N$_2$	–	2 h	–	LIB	[197]
Fe$_2$O$_3$ nanotubes@Co$_3$O$_4$	MIL-88B@ZIF-67	500	Air	5 °C min⁻¹	2 h	–	LIB	[198]
ZnO/3DGN or Fe$_2$O$_3$/3DGN	ZIF-8 or MIL-88-Fe	380	Air	–	1 h	–	Photocatalyst or LIB	[199]
ZrO$_2$ and Al$_2$O$_3$ coated LiCoO$_2$	UiO-66 & MIL-53 (Al)	600	Air	5 °C min⁻¹	5 h	–	Li–S battery	[200]
HPCS/Se	Ni-BTC	800	Ar	–	3 h	Selenium embedding	Li–S battery	[201]
carbon/ sulfur	MOF-5	900	N$_2$	5 °C min⁻¹	3 h	Sulphur embedding	Li–S battery	[62]
RGO/C-Co-S	ZIF-67	600	Ar, Ar +H$_2$	5 °C min⁻¹	3 h, 2 h	GO coating followed by Sulphur embedding	Li–S battery	[185]
GNPCSs	ZIF-8 & GO	800	Ar	3 °C min⁻¹	5 h	Zn removal	ORR	[175]
N-doped Fe/Fe$_3$C@C/RGO	Prussian blue	800	Ar	2 °C min⁻¹	3 h	–	ORR	[176]
ZnO@C	MOF-5	600	N$_2$	5 °C min⁻¹	3 h	–	Photodegradation	[157]
CuO/Cu$_2$O	Cu-BTC	350	Air	–	20 min	–	CO oxidation	[26]

(*Continued*)

Table 4. (Continued)

Hybrid-structure obtained	MOF used	Heating parameters				Post-treatment	Application	Reference
		Temp. [°C]	Gas	Heat rate	Duration			
Cu/CuOx/C	Cu-BTC	350–700	N_2	5 °C min^{-1}	0.5 h	–	CO oxidation	[27]
CuO/CeO$_2$	Cu-BTC	500–800	Air	–	6 h	–	CO oxidation	[23]
ZnO@NPC	ZIF-8	700–1000	N_2	5 °C min^{-1}	2 h	–	CO$_2$ fixation	[46]
ZnO@Co$_3$O$_4$	ZIF-8@ZIF-67	400, 400	N_2, Air	1 °C min^{-1}	2 h,2 h	–	CO$_2$ photoreduction	[132]
POM@Co$_3$O$_4$	POM@ ZIF-67	350	Air	5 °C min^{-1}	3 h	–	Water Oxidation	[154]
Co$_3$O$_4$/TiO$_2$	Co- (PA, SA, DHTA, and TA)	500	Air	–	5 h	–	hydrogen production	[202]
Fe$_2$O$_3$@TiO$_2$/Pt	MIL-101(Fe)@TiO$_2$	550	Air	–	16 h	Pt particles deposition	Hydrogen Production	[146]
Pd/NPC-ZIF-8	ZIF-8	900	N_2	5 °C min^{-1}	2 h	H$_2$PdCl$_4$ solution	Biofuel upgrade	[32]
CuNPs@C	Cu-BTC	400	N_2	5 °C min^{-1}	2 h	–	TMB oxidation	[31]
ZnO–calcium silicate	C-S-H@ZIF-8	450	Air	2 °C min^{-1}	4 h	–	Photocatalysis	[158]
Ag/ZnO@C	ZIF-8	500	–	5 °C min^{-1}	2 h	–	Photo-oxidation	[203]
CuOx-C	Cu-BTC	550	N_2	3 °C min^{-1}	2 h	–	Electrochemical degradation	[204]
NiO@C	Ni-BDC	600	N_2	–	2 h	–	Electrochemical degradation	[205]
Fe-C500	Fe-PTA	500	N_2	1 °C min^{-1}	1 h	–	Degradation of 4-NP	[206]
FeCu@C	[Fe, Cu]-BDC	600	Ar	5 °C min^{-1}	2 h	–	Sulfamethazine degradation	[207]
CoFe$_2$O$_4$ nanocrystal	Co/Fe bi-BDC	400	Air	1 °C min^{-1}	1 h	–	Degradation of bisphenol A	[208]

2D CoSNC: Two-Dimensional CoS$_{1.097}$/Nitrogen-Doped Carbon, LIB: Lithium-Ion Batteries, Li-S- battery: lithium-sulfur battery, HPCS/Se.: hierarchical porous carbon spheres, RGO/C–Co-S : Reduced graphene oxide/ cobalt doped porous carbon polyhedrons/ sulfur, GNPCSs: graphene-based nitrogen-doped porous carbon sheets, ORR : Oxygen reduction reaction, POM : Polyoxometalate, TMB: 3,3′,5,5′-tetramethylbenzidine, C-S-H: Calcium silicate hydrate, 4-NP: 4-nitrophenol, (PPF-3) MOF: porphyrin paddlewheel framework-3 (C$_{68}$H$_{40}$N$_9$O$_{11}$Co$_3$), JUC-155: ZnCo$_2$O(BTC)$_2$(DMF)·H$_2$O, Fe-MIL-88B NH2 : Fe(OH)[C$_4$H$_2$O$_4$(NH$_2$)], MIL-101(Cr) : Cr$_3$(O)(OH)(BDC)$_3$(H$_2$O)$_2$]25H$_2$O, MOF-74 (Ni) : Ni$_2$(dobdc); dobdc = 1,4-Dioxido-2,5-Benzenedicarboxylate, UiO-66: Zr$_6$O$_4$(OH)$_4$(BDC)$_6$, MIL-53 (Al): Al(OH)(BDC), Co- (PA, SA, DHTA, and TA): Co-MOFs; PA = pamoic acid; SA = salicylic acid; DHTA = 2,5-dihydroxyterephthalic acid; TA = terephthalic acid, and Fe-PTA: Fe-MOF; PTA = p-phthalic acid.

**ADVANCED
SCIENCE NEWS**

www.advancedsciencenews.com

NANO · MICRO
small

www.small-journal.com

Figure 8. Schematic illustration of the general preparation strategies from MOFs to their derived hybrid. Reproduced with permission.[209] Copyright 2017, The Royal Society of Chemistry.

other functional materials can be incorporated into the annealed MOFs to synthesize complex hybrid structures. This synthesis process for MOF-derived hybrid structures can retain the original structure of MOFs precursor even after the post-treatment for the incorporation of secondary materials. Many post-treatment methods of annealed MOFs have been reported so far, such as additional transformation of the thermally processed MOFs composition,[195] foreign materials incorporation inside porous structures of thermally processed MOFs,[62,193] and surface decoration of thermally processed MOFs with other materials.[146] Numerous MOF-derived porous carbon materials can be utilized as host materials to stack secondary elements e.g. sulfur,[62,193] and selenium[201] to form complex hybrid structures, which are otherwise complicated to produce using other techniques. As an example, a Se-embedded porous carbon hybrid sphere was synthesized using the post-treatment of thermally processed Ni-BTC.[201] The annealed Ni-BTC MOFs were first processed through acid removal of Ni ions to produce porous carbon spheres, subsequently, the porous carbon structure was processed through melt-diffusion to integrate Se into the structure, and finally the Se–carbon hybrid sphere was obtained.[201] Various other post-treatment methods like spin coating, mechanical mixing, electrostatic adsorption, and electrophoretic deposition can also be used to thermally process MOFs for the formation of MOF-derived complex hybrid structures with desired properties and predetermined functionalities. Thus, MOFs can be exploited as precursors or templates as well as foundation blocks to hybridize with other functional materials for the construction of complex hybrid structures with novel properties and predetermined functionalities. This will create enormous opportunities for the simplistic growth of unique functional materials for a wide range of applications in energy, gas sensing, catalysis, and biomedical.

2.7. Synthesis of MOF-Derived Metal Sulfides and Other

Solution infiltration of MOFs followed by mild heat treatment can produce porous metal sulfides and retain the original MOF

structure to some extent. In this synthesis process, for the sulfidation of MOF precursors, numerous sulfur-containing chemicals are utilized such as sodium sulfide, sulfur powder, and thioacetamide.[185,213] Here, heat treatment after solution-based sulfidation is an important step to achieve well crystallinity in the derived metal sulfide structure otherwise it remains amorphous.[213] Cho et al. reported the synthesis of Cu–MOF (HKUST-1) derived CuS nanoparticles using thioacetamide as a sulfur source and demonstrated the effect of heat treatment at different temperatures.[214] Su et al. reported microwave-assisted hydrothermal synthesis of yolk-shell CdS microcubes using Cd–Fe PBA as a precursor.[215] Growth of ZnS nanocages has been reported using ZIF-8 precursor and thioacetamide as a source of sulfur.[163] The nanocasting process[216] has been used to derive metal sulfides through the transformation of metal oxide replicas obtained using various metal nitrates and MOFs as precursors. X Sun et al. indicated that cobalt-based MOF can be transformed by thermal treatment (700 °C) to the mixed phase of Co_9S_8 and $CoS_{1.097}$ under an Ar environment while the same precursor MOF could produce Co_9S_8 as a single phase with mixed Ar and H_2 atmosphere at the same temperature by increasing the length of heating time to 2 h.[217]

Several other MOF derivatives such as transition metal oxides, phosphides, and nitrides,[91,101,106,213,218–222] have also been synthesized for their superior application possibility as electrocatalysts for Hydrogen generation, potentially replacing the Pt-based electrode materials. Porous structured Co-nitrides with regularly distributed $Co–N_4$ centers[223] were synthesized using Cobalt Imidazolate MOF as a precursor template. Proietti et al. synthesized Fe-based FeN_4 implanted into carbon planes using ZIF-8[224] as a precursor. **Table 5** summarizes various synthesis parameters of MOF-derived sulfides, carbides, and nitrides using heat treatment process and solution-based techniques respectively.

3. Characterization of MOF and Its Derivatives

The intrinsic functionalities and porous structures of metal–organic frameworks and their derivatives alongside their superficial properties make them appropriate for a variety of advanced emerging technologies. Most of the MOFs based applications involve the interaction of constituted materials with guest molecules. Optimization of an existing process or designing novel mechanisms requires a thorough understanding of the physicochemical characteristics of involved MOF substances and their interaction with guest molecules.

This section provides a concise overview of characterization techniques for MOFs and their derivatives (**Figure 9**). Various instruments are used to explore physical properties, structures, chemical states, elemental composition, as well as thermal, optical, electronic, magnetic, mechanical, and electrochemical attributes. Due to MOFs' structural complexity, a range of physicochemical techniques is necessary, as summarized in **Table 6**.

3.1. Characterization of Structural and Mechanical Properties

Understanding the fundamental structural properties of MOFs and their derivatives such as crystallinity, porosity, and precise

ADVANCED
SCIENCE NEWS
www.advancedsciencenews.com

NANO · MICRO
small
www.small-journal.com

Table 5. MOF-derived sulfides, carbides, and nitrides using heat treatment process.

Obtained material	MOF used	Heat treatment conditions				Refs.
		Temp. [°C]	Gas	Heat rate	Treatment Duration	
Iron carbide	MIL-100(Fe)	700	N_2	–	4 h	[225]
PtCu-Mo2C	NENU-5	800	Ar	5 °C min^{-1}	–	[226]
Molybdenum carbide Mo2C	Mo- imidazole	650–750	H_2+Ar	1 °C min^{-1}	2 h	[227]
molybdenum carbide-based hollow structure	Mo- Ni-BTC	800	N_2	2 °C min^{-1}	6 h	[228]
carbon nitride/ N-doped carbon polyhedral composite	ZIF-8	800	N_2	–	3 h	[229]
Nickel Nitride	Ni- imidazole	300–400	NH_3	2 °C min^{-1}	3 h	[230]
CuCeO2@NC	CuCe-BTC	650	H_2+Ar	3 °C min^{-1}	4 h	[231]
vanadium nitride	vanadium- imidazole	650	N_2+NH_3	5 °C min^{-1}	2 h	[232]
CoS$_{1,097}$	Co–MOF	700	Ar	5 °C min^{-1}	1 h	[217]
Co9S8	Co–MOF	700	H_2+Ar	5 °C min^{-1}	2 h	[217]
Co9S8/CoS$_{1,097}$	Co–MOF	700	Ar	5 °C min^{-1}	2 h	[217]
3D hollow cobalt sulfides	ZIF-67	600	Ar	2 °C min^{-1}	2 h	[233]

MIL-100(Fe): $Fe_3O(H_2O)_2OH(BTC)_2$; NENU-5: $Cu_2(BTC)_{4/3}(H_2O)_2|_6[H_3PMo_{12}O_{40}]$, Co-MOF: $Co(NCS)_2(H_2O)_2(4'4\text{-bipy})\cdot4'4\text{-bipy})$; bipy = dipydine.

high specific surface area is essential to move forward in optimizing the MOF characteristics. So, to establish the crystallinity and phase purity of MOFs, the fundamental characterization data needs to be collected and analyzed using X-ray diffraction (XRD) patterns. The morphology and crystal size of MOF and its derivatives can be studied using various microscopy techniques including transmission electron microscopy (TEM), scanning electron microscopy (SEM), and atomic force microscopy (AFM), as well as profilometry. Moreover, AFM could also be employed to characterize the mechanical properties of MOFs. Furthermore, to detect the crystal defects, vacancy, and defect types; fluorescent microscopy, electron paramagnetic resonance, and positron annihilation spectroscopy techniques have been employed. This section represents a details discussion of the above-mentioned structural and mechanical characterization techniques for MOFs and their derivatives. **Table 7** discusses the details, advantages, and limitations of characterization techniques used for MOF/MOF-derivatives study.

3.1.1. X-Ray Diffraction

To understand the functional properties of MOFs and their derivatives for applications in advance technologies, it is essential to determine their structures accurately. Due to the periodic structure of MOFs, X-ray diffraction techniques, especially single-crystal X-ray diffraction (SC-XRD) and powder X-ray diffraction (PXRD), are extensively used to identify the molecular structure and crystallinity of MOFs at the atomic or subatomic level.[234,235] SC-XRD analysis of MOFs requires large, high-quality single crystals, but their complex crystallization process poses challenges. MOFs may also exhibit structural heterogeneity, containing multiple polymorphs or crystallographic domains, making a single crystal insufficient to fully represent the MOF's structure. Achieving the right size and quality in MOF crystal growth can be challenging due to the involved reactions and gas temperatures. In such cases, powder X-ray diffraction (PXRD) patterns are a valuable alternative. In PXRD, all of the diffraction data are compressed into 1D space, specifically the 2θ diffraction angle.[234] This compression of reciprocal 3D space into 1D space results in significant peak diffraction overlap, making the accurate determination of 2θ peak positions and intensities challenging.[234,236] Therefore, a crucial step in PXRD analysis is to produce a high-purity and crystalline polycrystalline sample to obtain a reliable diffraction dataset. Inaccurate determination of peak positions and intensities can lead to difficulties in unit cell determination and the identification of space groups for MOFs and their derivatives. Once a crystalline sample is confirmed, crystallographic parameters such as lattice parameters, unit cell size, and crystallite size can be extracted from the powder diffraction pattern.[237] This process can be divided into three sequential steps: indexing, structure solution, and structure refinement (**Figure 10**). Indexing involves determining the lattice cell dimensions, vectors, and angles from peak position analysis in the powder diffractogram. Structure solution and refinement follow, where the intensity data are used to determine the space group and refine diffraction patterns.[234] In the structure refinement stage, PXRD pattern fitting is achieved using various refinement variables, including peak widths, shapes, positions,

ADVANCED
SCIENCE NEWS

www.advancedsciencenews.com

NANO · MICRO
small
www.small-journal.com
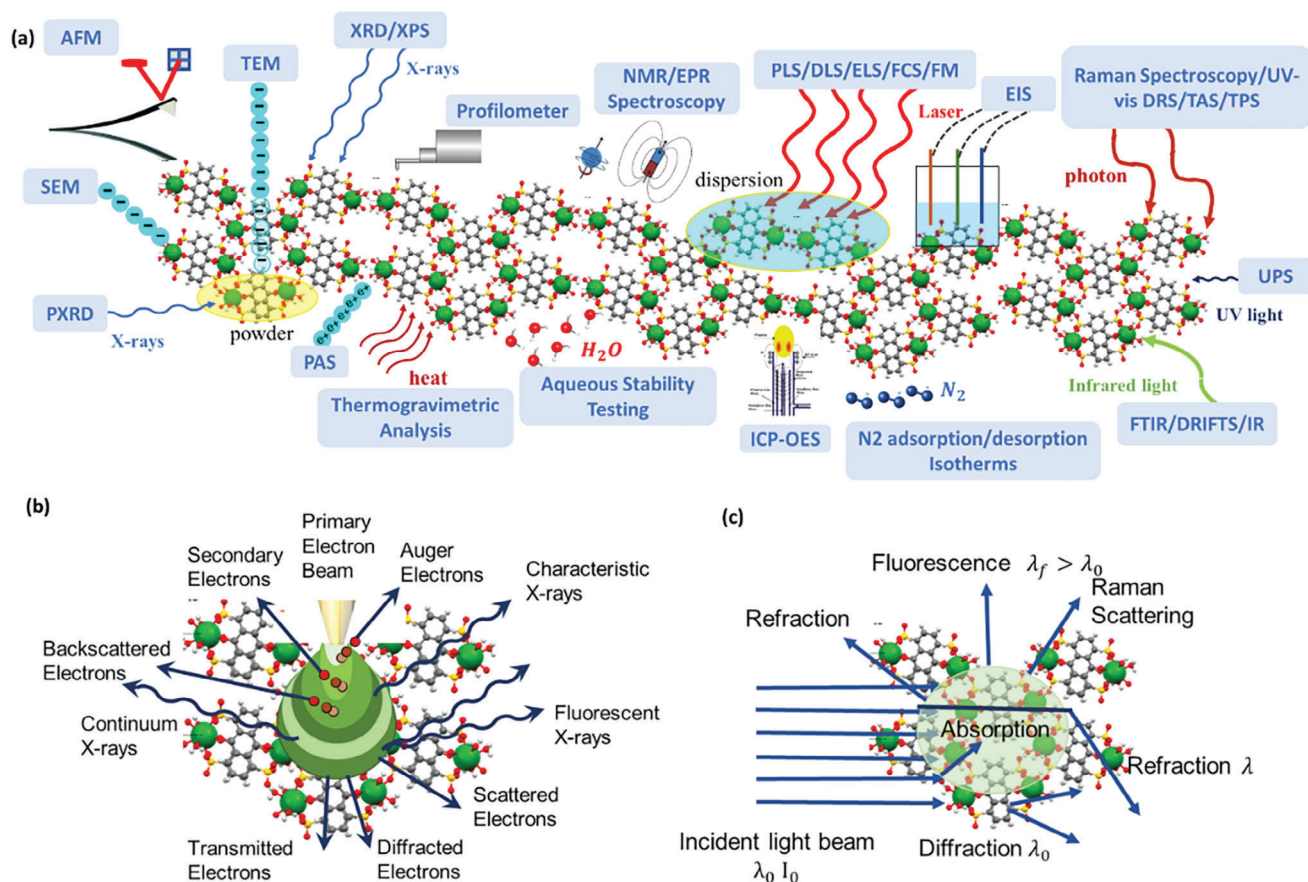
Figure 9. a) Schematic of characterization techniques used to study and explore MOFs/MOFs-derivatives properties. b) The mechanisms of electron matter interactions; c) the mechanism of light–matter interactions.

Table 6. A tabular representation of the physicochemical characterization methods for MOFs/MOFs-derivatives.

MOFs/MOFs derivatives Properties	Features	Characterization techniques
Structural properties	Crystallography properties	XRD, PXRD, TEM, SEM
	Surface topography & Microstructure	AFM, Profilometer, SEM, TEM
	Crystal defects	TEM, SEM, FM, PAS, EPR
Mechanical properties	Elasticity	AFM
Physical and electrochemical properties	Surface area, porosity	BET, BJH, DFT, HK, ESW
	Optical properties	UV-DRS, PLS
	Charge dynamics	PLS, TAS, TPS, EIS
	Thermal stability	TGA
	Colloidal stability	DLS, ELS, FCS
	Adsorption properties	Volumeter, Calorimeter
	Bulk porosity, linkers properties	BET, NMR
Chemical properties	Elemental state, composition	Raman, FTIR, EDS, DRIFTS, ICP-OES
Electronics properties	Bandgap potential, band-edge, and bandgap offset	UV–vis–NIR, XPS, UPS, PLS
	Fermi level	XPS, UPS

XRD: X-ray Diffraction, PXRD: Powder X-ray diffraction, TEM: Transmission Electron Microscope, SEM: Scanning Electron Microscope, AFM: Atomic Force Microscope, FM: Fluorescent Microscopy, PAS: Positron Annihilation Spectroscopy, EPR: Electron Paramagnetic Resonance, BET: Brunauer—Emmett—Teller for, BJH: Barrett-Joyner-Halenda, DFT: Density Functional Theory, HK: Horwath-Kawazoe, ESW: Excess Sorption Work, UV-DRS: Ultra Violet– Diffuse Reflectance Spectroscopy, UV-VIS-NIR: Ultra Violet–Visible– Near Infrared Spectroscopy PLS: Photoluminescence Spectroscopy, TAS: Transient Absorption Spectroscopy, TPS: Transient Photocurrent Spectroscopy, EIS: Electrochemical Impedance Spectroscopy, TGA: Thermogravimetric Analysis, DLS: Dynamic light scattering, ELS: Electrophoretic Light Scattering, FCS: Fluorescence Correlation Spectroscopy, NMR: Nuclear Magnetic Resonance, FTIR: Fourier-Transform Infrared, DRIFTS: Diffuse Reflectance Infrared Fourier Transform Spectroscopy, ICP-OES: Inductively Coupled Plasma Optical Emission Spectroscopy, XPS: X-ray Photoelectron Spectroscopy, UPS: Ultraviolet Photoelectron Spectroscopy.

ADVANCED
SCIENCE NEWS

www.advancedsciencenews.com

NANO · MICRO
small
www.small-journal.com

Table 7. Comparison of high-resolution characterization techniques for structural and mechanical properties of MOF-derivatives.

Technique	TEM/SAED	SEM	FM/Super resolution microscopy	AFM	XRD
Resolution	0.1–5 Å	2–10 nm	20–50 nm	≤1–50 nm	0.2–3.5 A°
Advantage/application	• High-resolution imaging with magnification • Crystallographic information • Elemental analysis • Ability to visualize guest molecules and defects	• Imaging surfaces at nanoscale resolution with magnification • Coupled with EDS for elemental analysis as well as surface composition • Porosity analysis • In-situ study • Surface functionalization	• Visualization with spatiotemporal resolution • Localization of guest molecules • Multiplexing capabilities	• Extract multiple properties • High spatial and lateral resolution • Functional mapping • In-situ imaging/characterization	• Atomic structure • Crystallization • Phase identification • Stability • Guest-host interactions
Disadvantage	• Sample preparation • Sample size • Beam damage • Depth resolution • Sample contamination	• Beam damage • Vacuum environment • Resolution	• Photobleaching • Background autofluorescence • Expensive	• Tip artifact • Surface sensitivity which is challenging for 3D-MOFs and their derivatives • Imaging speed	• Sample preparation * Expensive • Size limitation • Time resolution • Sensitivity to disorder structure of MOF-derivatives

intensities, and background intensity profiles. MOF phase purity can be confirmed by comparing experimental powder patterns with simulated patterns generated from single-crystal X-ray data or by using computational modeling.[238]

The initial solution preparation for PXRD follows a similar procedure to single-crystal diffraction, with some adjustments like histogram matching to the chemical composition.[239] Applying the charge-flipping method to powder diffraction data can be improved by providing primary phase sets upfront, avoiding random initial phase assignments in the first charge-flipping cycle.[237] These initial phase sets can be obtained from high-resolution electron microscopy[240] or by using the charge flipping method on subsets of low-resolution 2D projection reflections.[241] Utilizing this data in subsequent charge-flipping iterations leads to significantly enhanced electron density maps.[242]

Various XRD techniques, particularly SC-XRD and PXRD, have been successfully employed to determine the crystal structures of MOFs and their derivatives.[234,236,237] Notable applications of XRD analysis in MOFs include UiO-66,[243] the flexi-ble framework MOF-derivatives like MIL-53,[244] MOF-5,[245] and HKUST-1.[246] For UiO-66,[247] XRD reveals its 3D framework with hexagonal pores, providing lattice parameters, atom positions, and pore size/connectivity information crucial for understanding adsorption and diffusion properties.

In the case of UiO-66, high-quality synchrotron radiation data analyzed using the EXPO program yields structural information without prior knowledge.[248] A similar approach using the charge-flipping technique is applicable to the metal-triazolates (METs) class of MOFs (**Figure 11a,b**).[237]

SC-XRD is a key tool for obtaining precise information on the locations of metal ions, organic linkers, and guest molecules within MOF pores. It also sheds light on structural changes during MOF and MOF derivative synthesis. For instance, SC-XRD plays a vital role in monitoring thermal activation and guest-host interactions in divalent metal-based MOFs like MOF-74 (Mg^{2+}, Co^{2+}, Ni^{2+}),[249] UTSA-74 (Zn^{2+}),[250] and MFM-170(Cu).[251] Chen et al.[251] recently used in situ variable-temperature SC-XRD to capture structural changes in PCN-250 during thermal activation. As the temperature increased from 323 to 473 K, they
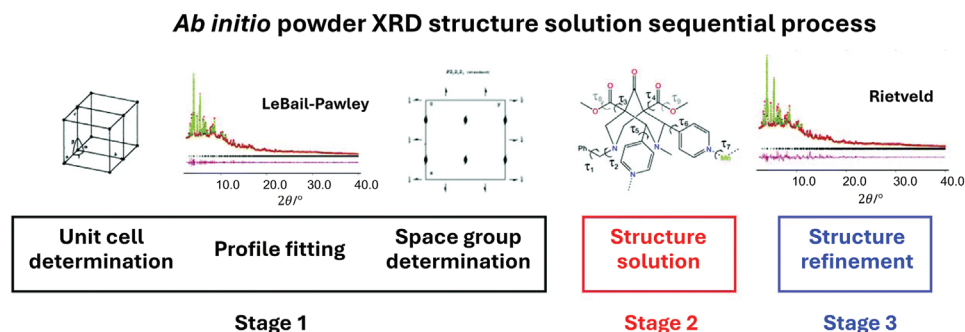
Figure 10. Showing the three different stages in the structure determination from powder XRD. Stage 1 has been divided into three substages highlighting the importance of each point. Reproduced with permission.[234] Copyright 2020, The Royal Society of Chemistry.

**ADVANCED
SCIENCE NEWS**

www.advancedsciencenews.com

**NANO · MICRO
small**

www.small-journal.com
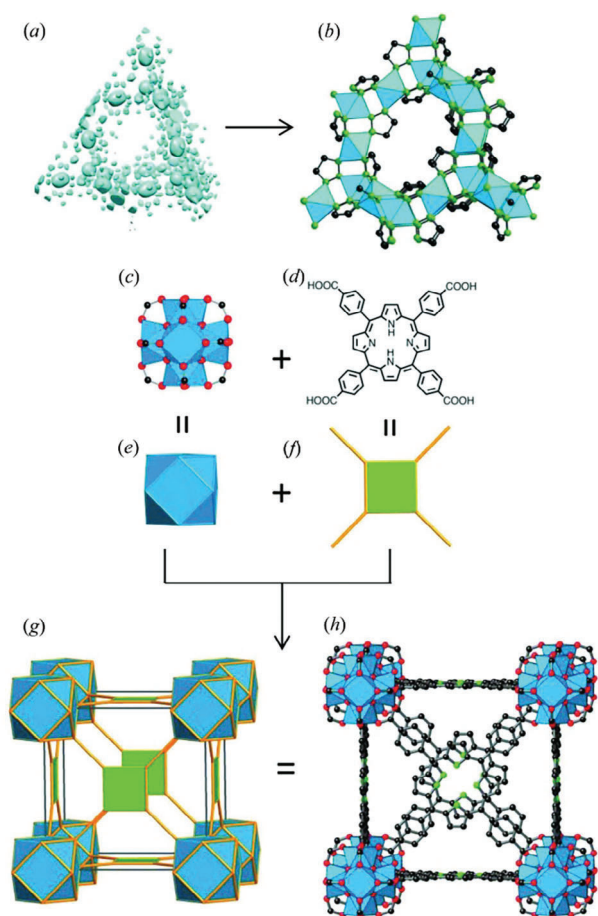
Figure 11. Interpretation of structure data from PXRD data analysis: charge-flipping method applied to PXRD data leads to the electron density map (a) from which the structure of metal-triazolates, METs (b), has been attained. Subsequent to the reticular method, the 12-connected zirconium SBU (c) and the tetracarboxyphenylporphyrin organic linker (d) are simplified to a cuboctahedron (e) and a square (f), respectively. Their integration generates the edge transitive net ftw (g), from which the structure of MOF-525 (h) is directly derived [Crystallography of metal–organic frameworks]. Reproduced with permission.[237] Copyright 2014, IUCrJ.

observed gradual exposure of two Fe^{3+} sites, accompanied by elongation of terminal $Fe-OH/H_2O$ bonds and shortening of Fe-μ3-O bonds (**Figure** 12). Additionally, they found that partially replacing Fe^{3+} with divalent metals (M = Ni^{2+}, Co^{2+}, Zn^{2+}, Mg^{2+}) lowered the activation temperature and increased the number of open metal sites, allowing for a comparison of different metals' effects on thermal activation.

In a study by Maliuta et al.[252] both SC-XRD and PXRD measurements were used to explore the particle size-dependent flexibility of DUT-8(Cu), a pillared layer metal–organic framework. This investigation cantered on the unique d9-configuration of Cu(II) as the metal center in [Cu2(2,6-ndc)2dabco]n (DUT-8(Cu)), which results in a stiffer paddle wheel structure but weaker Cu-N bonds. These differences in configuration lead to substantial variations in flexibility compared to DUT-8 structures based on Zn, Co, or Ni. As an example of MOF-derived porous carbon materials, **Figure** 13a displays XRD diffraction patterns for UIO-66,

NC-600, and PANI@NC-600.[253] The characteristic peaks of the pure UiO-66 precursor demonstrate excellent crystallinity. After carbonization at 600 °C and subsequent etching, the appearance of two peaks in the 20°–30° and 40°–50° range is attributed to carbon signals, confirming the formation of a graphitic carbon structure. PXRD is also useful for studying the influence of carbonization temperatures on carbon formation in MOF-derived materials (Figure 13b). Cz-MOF-253 was carbonized at various temperatures from 700 to 1000 °C in an argon atmosphere, resulting in numerous MOF-derived carbons.[254] As shown in Figure 13b, PXRD patterns of Cz-MOF-253 carbons exhibit weak and broad peaks, with three peaks around 12°, 24°, and 44°. The first peak corresponds to (001) of graphene oxide, with its intensity decreasing as the pyrolysis temperature exceeds 800 °C, while the others are associated with the diffraction peaks (002) and (101) of graphitic carbon.[254]

Figure 13c presents the composition and structure of MIL-53(Fe)-X and their derived Fe_2O_{3-X} (X = 0.5, 1, 2, 3, 6, 12), representing MOF-derived porous metal oxides, as determined by X-ray diffraction measurements.[114] With an increase in reaction time from 0.5 to 3 h, similar characteristic peaks emerge around 6.8°, 11.2°, and 17.9°, corresponding to reported peaks for MIL-53(Fe).[201] Enhanced peak intensity with prolonged reaction time indicates improved crystallinity from MIL-53(Fe)-0.5 to MIL-53(Fe)-3. MIL-53(Fe)-6 exhibits weak characteristic peaks attributed to its yolk–shell structure.[114] After 12 h of reaction time, MIL-53(Fe)-12 shows slightly different characteristic peaks around 9.2°, 12.7°, 17.7°, and 25.5°.

As a representative example of MOF-derived porous hybrid structures, Figure 13d compares the XRD patterns of Cu–Ni–BTC and CuO@NiO with Ni–BTC and NiO.[143] Cu–Ni–BTC exhibits characteristic peaks associated with $Cu_3(BTC)_2(H_2O)_3$.[255] The Ni–BTC composite appears largely amorphous, with no related peaks observed in the XRD patterns. Upon calcination of the Cu–Ni–BTC precursor, two characteristic peaks corresponding to CuO and NiO appear in the final product, indicating that CuO@NiO is a mixture of NiO and CuO.

Table 8 summarizes the advantages and disadvantages of the main XRD techniques for studying MOF-derived materials.

Worth to mention the main difference between SC-XRD and PXRD in studying MOF-derivatives lies in their analytical scope and sample preparation requirements. SC-XRD provides detailed structural information by analyzing single crystals, offering precise atomic arrangements and crystallographic symmetry. In contrast, PXRD offers bulk analysis of powdered samples, providing information on crystallinity, phase purity, and overall structural characteristics. While SC-XRD requires high-quality single crystals and can be time-consuming, PXRD is faster and can analyze polycrystalline samples, making it more suitable for rapid screening and characterization. Both techniques, however, are crucial for understanding MOF-derived materials' structural properties, facilitating their design and optimization for various applications such as gas storage, catalysis, and drug delivery.

3.1.2. Transmission Electron Microscopy (TEM)

TEM, a versatile nanoscale microscopy method, uses a high-energy electron beam to create images. TEM offers magnification

ADVANCED
SCIENCE NEWS

www.advancedsciencenews.com

NANO · MICRO
small
www.small-journal.com
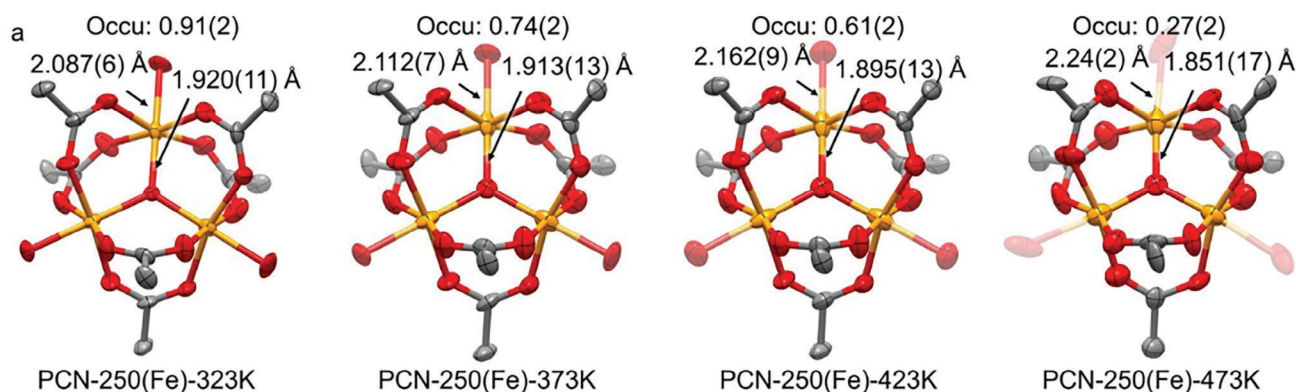
Figure 12. In situ variable-temperature SC-XRD analysis of PCN-250(Fe). Single-crystal structures of the $[Fe_3(\mu_3\text{-}O)]$ cluster at 323, 373, 423, and 473 K. Reproduced with permission.[251] Copyright 2023, American Chemical Society.

from 50 to 10^6, providing both images and diffraction patterns to confirm MOF/MOFs derivative morphology and crystallinity. Using TEM, surface defects and facets can be identified. TEM reveals MOF and derivative morphology, size distribution, and, through electron tomography, generates 3D images. Additionally, TEM precisely locates guest components within MOFs. As an ex-

ample, **Figure 14a** demonstrates high-resolution TEM can visualize the single-molecule magnets $[Mn_{12}O_{12}(O_2CCH_3)_{16}(OH_2)_4]$ ($Mn_{12}Ac$) inside the NU-1000 MOF.[256,257] Although conventional TEM can characterize the guest components of numerous guest@MOFs, characterization of volatile guest molecules at room temperature is impossible. In this case, due to
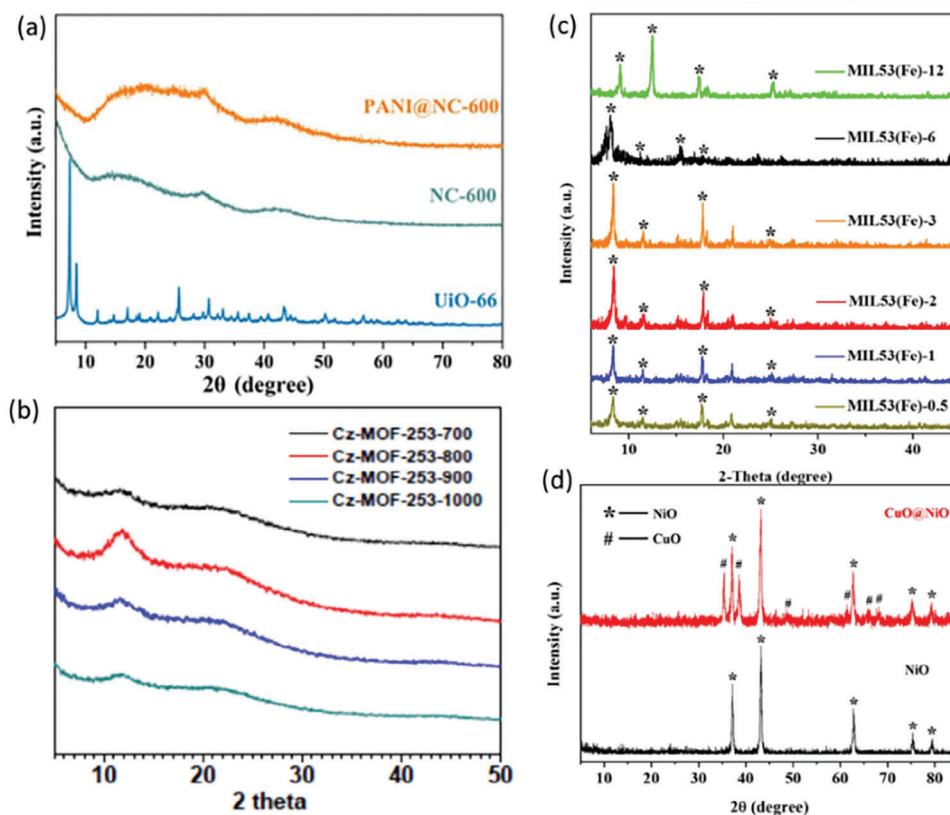
Figure 13. a) XRD diffraction patterns of UiO-66, NC-600, and PANI@NC-600. Reproduced with permission.[253] Copyright 2019, Elsevier. b) PXRD patterns of Cz-MOF-253 derived from the pyrolysis of MOF-253 at different temperatures. Reproduced with permission.[254] Copyright 2017, Wiley. c) XRD patterns of MIL-53(Fe)-0.5, MIL-53(Fe)-1, MIL-53(Fe)-2, MIL-53(Fe)-3, MIL-53(Fe)-6, and MIL-53(Fe)-12, respectively. Reproduced with permission.[114] Copyright 2017, American Chemical Society. d) XRD patterns of MOF-derived CuO@NiO and NiO microsphere. Reproduced with permission.[143] Copyright 2015, American Chemical Society.

**ADVANCED
SCIENCE NEWS**

www.advancedsciencenews.com

NANO · MICRO

small

www.small-journal.com

Table 8. Comparison between SC-XRD and PXRD as main XRD techniques in the study of MOFs and MOFs derived materials.

Technique	SC-XRD	PXRD
Advantages	• Determining the positions of individual atoms within the crystal lattice with high resolution • Determination of the complete 3D crystal structure of a MOF • Analysis of bonding interactions, coordination environments, and geometric features in the MOF • Determine the absolute configuration of chiral MOFs	• Identifying different phases present in MOF samples • Quantitative analysis of MOF samples, such as determining phase composition, crystallinity, and phase ratios • Non-destructive technique • Allowing for repeated measurements and further characterization on the same MOF sample • High-throughput screening of MOF libraries • Provide information about the presence and quantity of amorphous material in MOF samples • Allowing for characterization of their degree of crystallinity
Disadvantages	• Requires the availability of high-quality single crystals of the MOF • Process of growing suitable single crystals can be time-consuming and may require expertise in crystallography • Requires relatively large single crystals • Limiting the study of MOFs with limited crystal size or stability	• Does not provide precise atomic positions or detailed structural information at the atomic level unlike single-crystal X-ray diffraction • Overlapping diffraction peaks making it difficult to extract precise information about individual phases or structural features especially in cases of complex or highly disordered MOFs • Exhibit preferred orientation where the particles tend to align in a certain way • Limitations in characterizing nanoscale features, such as defects, surface reconstruction, or small crystallite size effects • Grinding the MOF into a fine powder can introduce sample artifacts or alter the properties of the material

cooling the specimen to liquid nitrogen temperature, the cryo-EM is an appropriate candidate. By equipping cryo-EM with a direct electron detection camera, it is possible to analyze the structure and composition of CO_2-encapsulated ZIF-8[256,258] (Figure 14c). Moreover, the step-edged defects in pristine ZIF-8 are extracted using cryo-EM (Figure 14e–h).
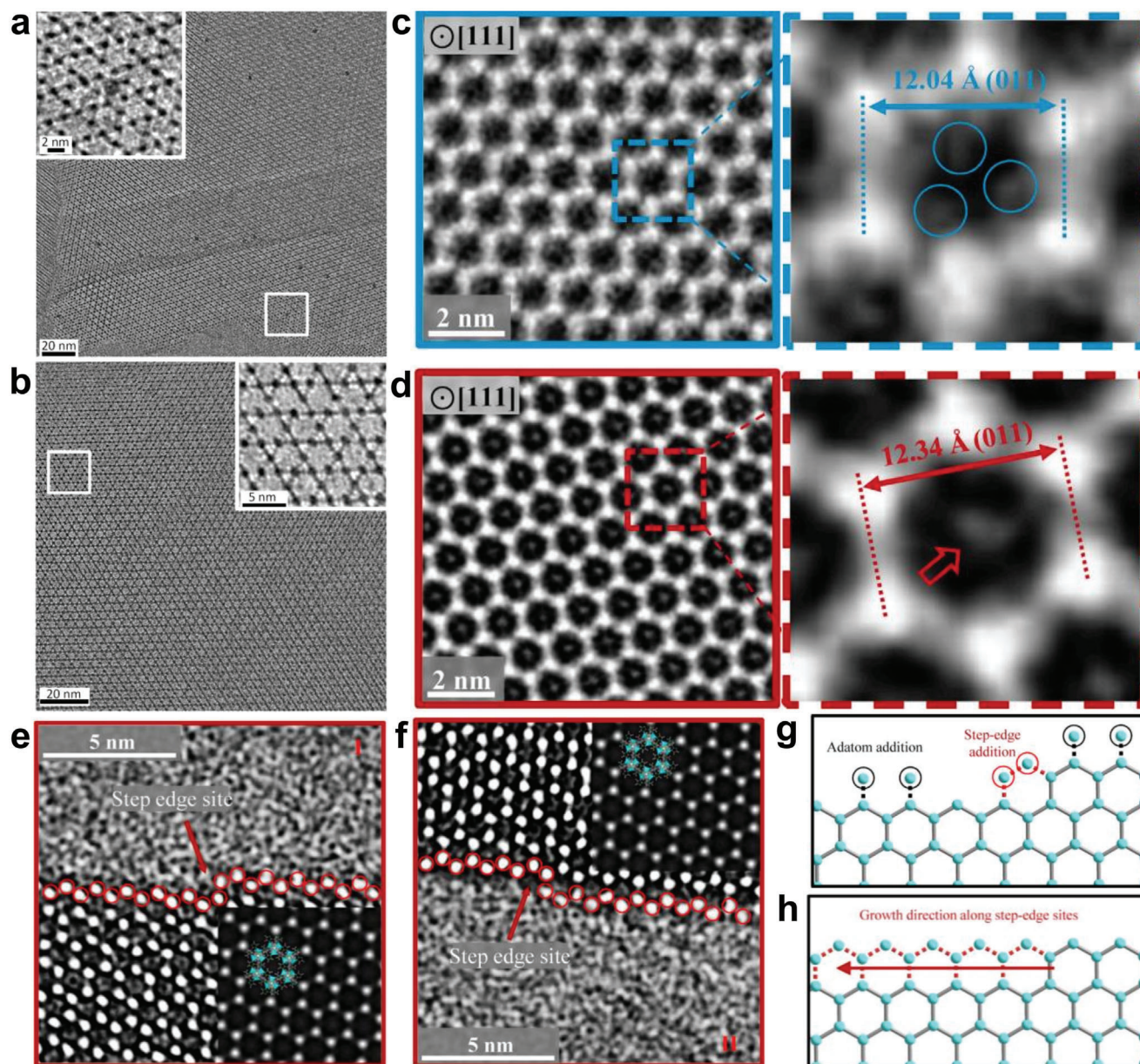
In the case of MOF derivatives, where calcination is a primary preparation method, the dynamic carbonization process can be studied using TEM heating holders.[259–261] One such study investigated the carbonization process of Ni-MOF using in-situ hot-stage TEM.[260] The findings revealed increased crystallization of Ni particles at temperatures above 300 °C. At temperatures exceeding 700 °C, Ni particles aggregated into larger particles, and the derivative obtained at 600 °C proved to be a recyclable and highly efficient electrocatalyst for 4-nitrophenol reduction.[262] To analyze the impact of pyrolysis temperature on the structural, functional, and electrocatalytic properties of ZIF-67 derivatives, in-situ TEM imaging has been employed (**Figure 15**).[263] Below 300 °C, ZIF-67 remains stable, while a disordered structure emerges at ≈500 °C. Raising the temperature results in the growth of Co particles and the graphitization of carbon. Furthermore, TEM has been employed in the study of ZIF-8 (Zeolitic Imidazolate Framework-8) composed of zinc ions coordinated with imidazolate linkers showing its formation and growth through synthesisation[264] as well as MOF-74 as a family of MOF derivatives, including MOF-74(M), where M represents a metal ion such as Zn, Mg, or Ni and MOF-808 composed of zirconium oxide clusters and tetracarboxylate linkers[265] to reveal details about the particle shape, size distribution, and the presence of defects or structural distortions.

Despite the successful use of TEM in MOF studies, the major limitation is a high degree of MOF instability when high-energy electrons are used in TEM. There are several TEM methods used for MOF studies depending on the target application.[266] For morphological characterization, bright field transmission electron microscopy (BFTEM) and high angle annular dark field scanning transmission electron microscopy (HAADF-STEM) are the most suitable techniques. As HAADF-STEM imaging possesses less chemical sensitivity, it is recommended to use it for imaging metallic particles in MOFs. To obtain structural information on MOFs, selected area electron diffraction (SAED) and high-resolution TEM (HRTEM) are good candidates. Using these techniques, it is possible to identify the crystalline phases and orientation as well as structural defects. SAED involves directing a focused electron beam onto a selected area of the sample and analyzing the resulting diffraction pattern created by electron interaction with the crystal lattice. In SAED, the crystal lattice serves as a 3D diffraction grating, causing electrons to scatter in specific directions, forming a pattern of bright spots or rings. The spacing between these spots offers insights into lattice spacing in different crystal planes, enabling the determination of crystal structure, lattice parameters, and crystal orientation. The intensity of diffraction spots provides information about the atomic arrangement within the crystal lattice. Wu et al.[267] have used SAED to explain the formation of Ni-MOF-74 and Ni-MOF-74 shells via epitaxial growth (**Figure 16**). As depicted in Figure 16, three SAED patterns exhibit remarkable similarity, indicating a high degree of alignment between the crystal orientations of the core MOF and the shell MOF. Considering its susceptibility to acid, Mg-MOF-74 serves as the most acid-labile analog among all counterparts. Consequently, the core of Mg-MOF-74 can be selectively eliminated through chemical etching with HCl, thereby resulting in a hollow Ni-MOF-74 structure.

By coupling with Energy Dispersive Spectroscopy (EDS) or Energy Dispersive X-ray Analysis (EDX or EDAX), the determination of elemental composition on a nanometre scale could be possible. This is especially useful in STEM mode, as the small

**ADVANCED
SCIENCE NEWS**

www.advancedsciencenews.com

**NANO · MICRO
small**

www.small-journal.com

Figure 14. HRTEM images of a) $Mn_{12}Ac@NU$-1000 and b) pristine NU-100. CTF-corrected denoised images of c) a ZIF-8 particle and d) a CO_2-filled ZIF-8 particle. e,f) Cryo-EM images of two edges of a ZIF-8 particle (inset: simulated TEM images with overlaid atomic structures). g) Schematic of possible surface additions of Zn clusters during ZIF-8 growth. h) Schematic of ZIF-8 growth initiated at the step-edge site. Reproduced with permission.[256] Copyright 2022, Taylor & Francis.

size of electron beams permits obtaining significant resolution in chemical images.

3.1.3. Scanning Electron Microscopy (SEM)

SEM is a high-resolution analytical tool that uses an electron beam to image surfaces at the nano/microscale. In SEM, secondary electrons reveal morphology and topography, while backscattered electrons offer atomic information. X-rays, with specific wavelengths tied to elements, enable element iden-

tification and elemental distribution maps (EDS mapping). SEM's ability to reveal nanoparticle structures is valuable for measuring various MOF and MOF derivative properties like topology, morphology, crystal size, and elemental composition. For example, **Figure 17a**[268] displays SEM images of MOF-derived nanoporous carbon (NPC) materials synthesized by introducing guest species.[269] The porous carbon exhibits various nanoparticle shapes, such as polyhedral, fiber, and web-like structures. SEM can also study the impact of substituting MOFs or guests on nano-diatom morphology after carbonization. Reactive metals are substituted with homologous metals

**ADVANCED
SCIENCE NEWS**

www.advancedsciencenews.com

**NANO · MICRO
small**

www.small-journal.com
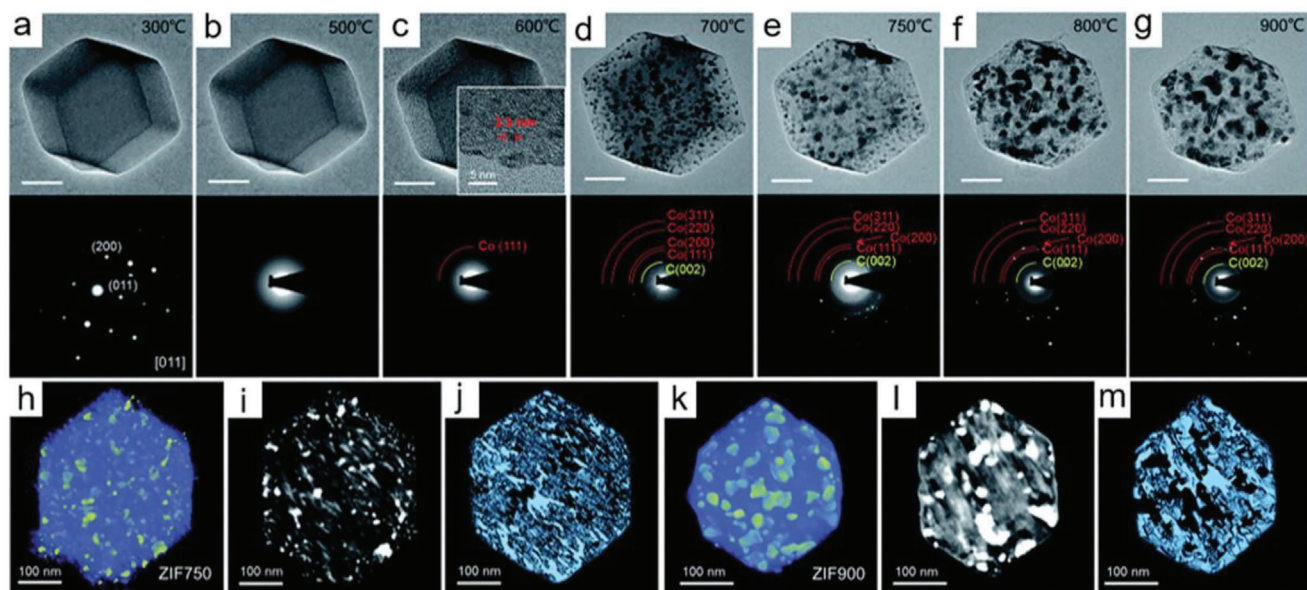
Figure 15. a–g) Images obtained by in-situ TEM as well as associating SAED patterns of ZIF-67 obtained at different temperatures. 3D tomographic reconstruction of h–j) ZIF750 and k–m) ZIF900, respectively. Reproduced with permission.[256] Copyright 2022, Taylor & Francis.

or oxide-forming species, preventing metal-catalyzed carbon formation. Figure 17b,c shows significant morphological changes in the MOF host, forming guest/host-dependent carbonaceous materials.[269] SEM imaging of insulating MOFs poses challenges due to the charging effect. To achieve high-resolution images,

Figure 16. Select area electron diffraction (SAED) patterns of Mg-MOF-74@Ni-MOF-74. Reproduced with permission.[267] Copyright 2019, American Chemical Society.
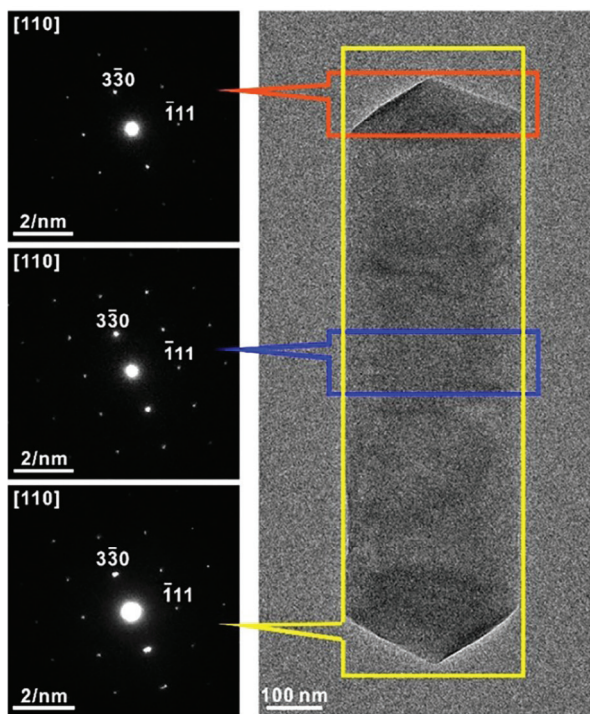
coating MOFs with conductive materials like gold, titanium, or osmium is essential to reduce electron gun-induced charges. Optimal accelerating voltage selection is crucial to reveal surface details without causing heat-induced damage. Field Emission Scanning Electron Microscopy (FESEM) provides a highly focused beam with a spot size ranging from 0.4 to 5 nm, improving resolution at lower voltages, and minimizing charging and crystal damage risk. Combining Energy Dispersive Spectroscopy (EDS) with SEM enables qualitative and quantitative analysis of MOF elements, influenced by sample surface conditions. Caution in coating material selection is necessary to avoid peak overlap with MOF metals, preventing erroneous analysis.

3.1.4. Atomic Force Microscopy (AFM)

AFM has emerged as a powerful imaging and characterization technique due to its sub-angstrom resolution and in situ measurement capabilities.[270–278] It not only measures surface roughness and morphology but also provides insights into crystal growth in MOFs and MOF derivatives.

In AFM measurements, the deflection of a microcantilever is used to probe interactions between the specimen's surface and a nanoscale tip at the cantilever's end. The earliest AFM mode, contact mode, involved raster scanning the AFM probe over the sample surface while maintaining a constant force through deflection detection by adjusting the probe's height. Contact mode faced challenges like unwanted friction and potential sample or tip damage,[279] leading to the development of dynamic AFM to provide more characterization information and minimize friction.[280]

Dynamic AFM involves the microcantilever oscillating at/near its resonance frequency while scanning the sample surface and has two major modes: amplitude modulation atomic force
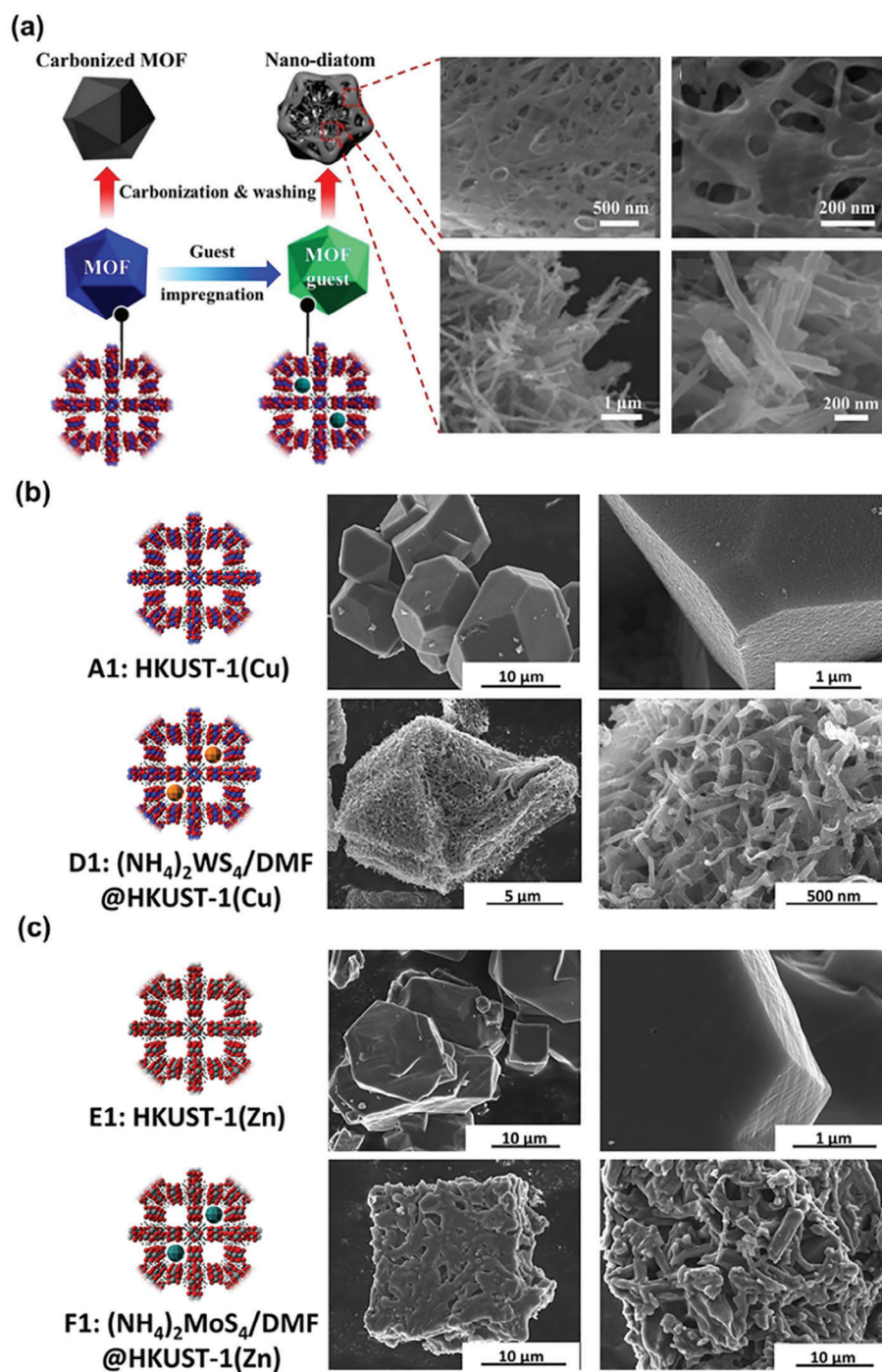
Figure 17. a) Preparation procedure for the fabrication of nano-diatoms derived from guest impregnation of a polyhedral MOF. Reproduced with permission.[268] Copyright 2019, Wiley. b,c) Schematic illustrations of precursors (left column) and SE-SEM images of products (two columns on the right-hand side) after the thermochemical treatment of b) A1 (top) and D1 (bottom); and c) E1 (top) and F1 (bottom). Reproduced with permission.[269] Copyright 2018, American Chemical Society.

microscopy (AM-AFM or tapping mode) and frequency modulation atomic force microscopy (FM-AFM).[280]

Beyond these common dynamic AFM modes, several advanced techniques have been developed to increase resolution and extract more information from MOFs, including multifrequency AFM,[281] conductive AFM,[282] electrochemical AFM,[283] force mapping AFM[282] and AFM-based infrared spectroscopy (AFM-IR).[284] In multifrequency AFM, the cantilever is excited and detected in different frequencies including the harmonics and/or eigenfrequencies.[285] Conductive AFM uses conductive

ADVANCED
SCIENCE NEWS
www.advancedsciencenews.com

NANO · MICRO
small
www.small-journal.com

tip scans across the specimen's surface in contact mode while applying a bias voltage and measuring the resulting current flow to create a current map alongside a topographic image.

Electrochemical AFM integrates conventional AFM with electrochemical measurements to perform in-situ measurements in an electrochemical cell, allowing the study of electrode surface morphology changes during electrochemical reactions. Force mapping AFM involves the AFM probe making constant-rate contact and separation with the sample surface while scanning, generating topographical images and force-versus-distance curves.[286] These data create a force map alongside the topography.

In AFM-IR, the AFM tip detects local thermal expansion in a sample due to infrared radiation absorption, combining topography with chemical analysis and compositional mapping from infrared spectroscopy, offering spatial resolution in both areas.

Generally, AFM's applications in MOF studies can be categorized into two classes:[287]

1) Providing high spatial and temporal resolution maps of MOF materials (both 2D and 3D) and real-time crystallization mechanisms.
2) Nanoscale mechanical characterization of MOFs.

For the first time, Shoaee et al.[288] used AFM to map the HKUST-1 surface, revealing defects, crystal aspects, and growth (Figure 17). Real-time images showed triangular {111} facet growth with ternary symmetry. Within 77 minutes, a small nucleation point formed, rapidly expanding into a larger step.[271] After 97 min, a sudden drop in step speed corresponds to a sudden change in supersaturation. AFM also unveiled MOF-5's spiral crystal growth and structure (Figure 18). MOF-5's atomistic crystal growth depended on Zn/H_2bdc ratio, causing shifts in growth rates and terrace morphology.[289] Recently, the AFM was used to study the surface reconstruction processes of a MOF material (Ce-RPF-8) immersed in water and glycerol. The Ce-RPF-8 characterized with angstrom resolution shows the diffusion of molecular species along terraces and step edges.[290]

AFM serves not only to examine MOF morphology and crystal growth but also to assess their nanomechanical properties. Two AFM approaches are commonly used: nanoindentation with AM-AFM and multifrequency AFM, notably bimodal AM-FM configuration.[281,291,292] The latter offers the advantage of capturing both sample topography and stiffness simultaneously in a shorter time. Sun et al.[291] employed bimodal AM-FM AFM to determine Young's modulus for HKUST-1 thin films, yielding values ranging from 3 to 6 GPa. However, they used Matrimid5218 as a reference material with a Young's modulus of 4 GPa, which is not suitable for MOFs. Thus, their Young's modulus measurement approach for MOFs needs refinement for accuracy. Enhancing this technique could enable the assessment of MOF mechanical properties across various metal ions and chemical functionalities. Bimodal AFM measurements on different Zr and Hf isostructural UiO-66-type MOFs revealed that UiO-66(Hf)-type MOFs exhibit a higher Young's modulus (46−104 GPa) than UiO-66(Zr)-type MOFs (34−100 GPa) (Figure 19).[291] Additionally, zinc/copper-based MOFs display a lower Young's modulus (3−10 GPa) compared to Zr and Hf isostructural UiO-66-type MOFs. This study demonstrates the tunability of MOF mechan-
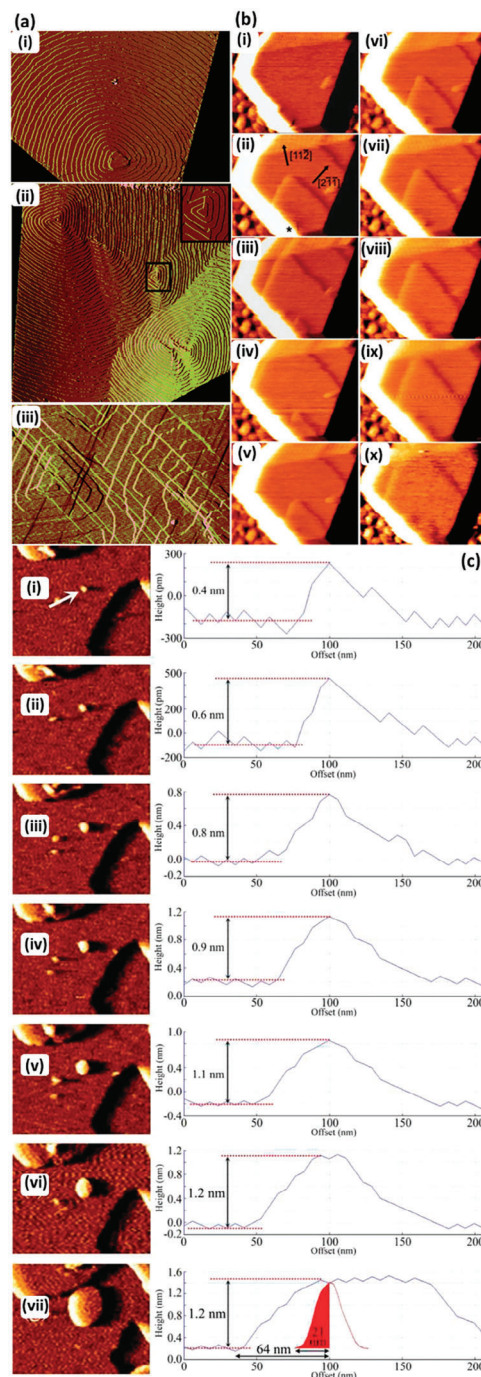
Figure 18. a) {111} facets of HKUST-1 images acquired by AFM, illustrates i) a double-growth spiral, ii) merging single- and multiple growth spirals iii) growth spirals overlaid with fractures primarily in the <110> directions. Reproduced with permission.[288] Copyright 2008, The Royal Society of Chemistry. b) Real-time AFM images of the {111} facet growth of an HKUST-1 crystal at i) 56, ii) 77, iii) 79, iv) 82, v) 85, vi) 88, vii) 91, viii) 94, ix) 97, x) 108 min after injection of the growth solution. Reproduced with permission.[271] Copyright 2009, The Royal Society of Chemistry. c) Real-time AFM images and cross-sectional views of a developing growth step on the (110) face of a ZIF-8 crystal at 0 (i), 2.9 (ii), 4.9 (iii), 7.8 (iv), 12.8 (v), 15.6 (vi), and 40 (vii) min after first probation of the 2D surface nuclei. Reproduced with permission.[272] Copyright 2011, American Chemical Society.
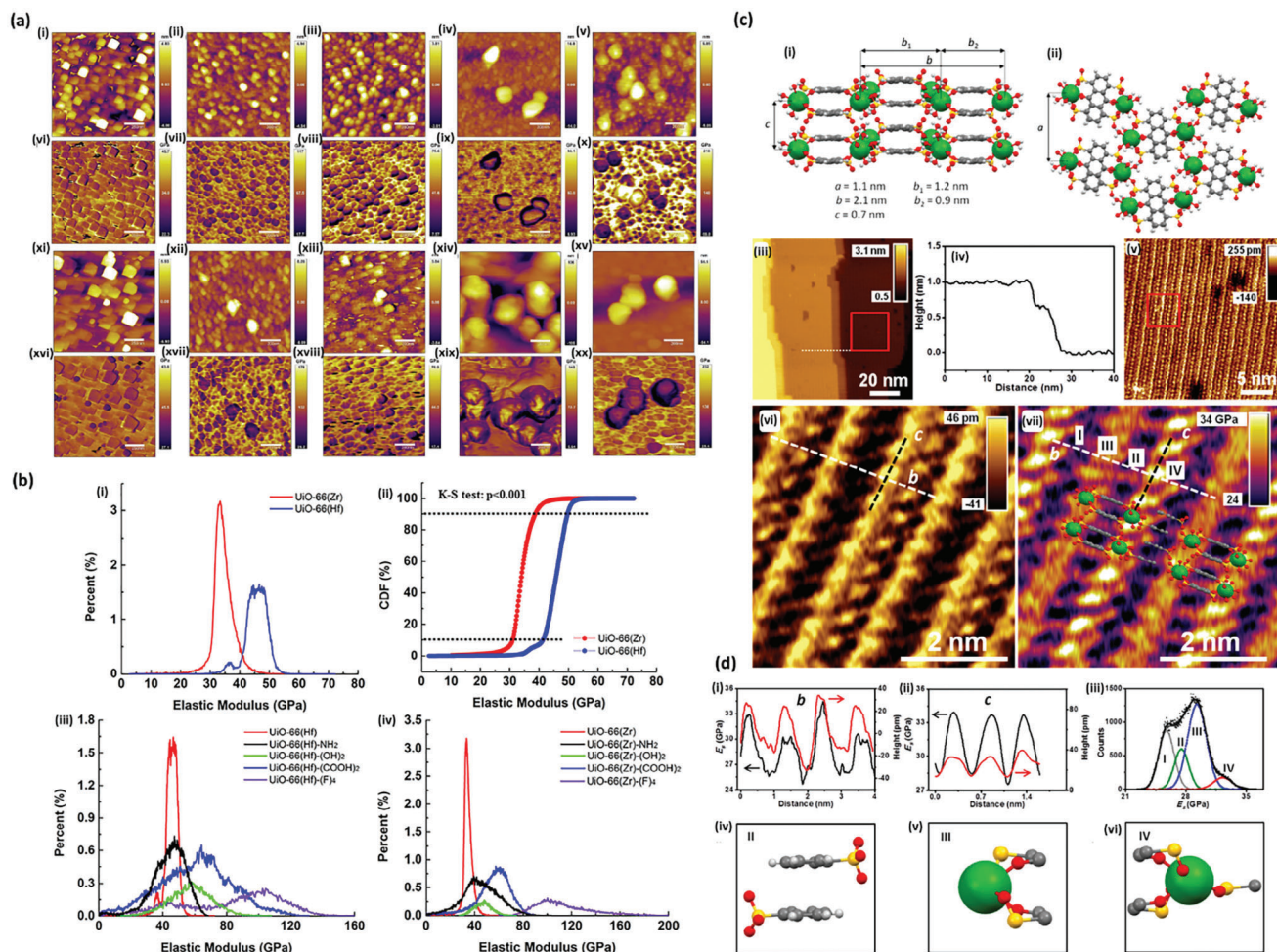
Figure 19. a) Topography mapping of i) UiO-66(Zr); ii) UiO-66(Zr)-(OH)2; iii) UiO-66(Zr)-NH2; iv) UiO-66(Zr)-(COOH)2; v) UiO-66(Zr)- (F)4. Elastic modulus mapping of vi) UiO-66(Zr); vii) UiO-66(Zr)-(OH)2; viii) UiO-66(Zr)-NH2; ix) UiO-66(Zr)-(COOH)2; x) UiO-66(Zr)-(F)4.[291] Topography mapping of xi) UiO-66(Hf); xii) UiO-66(Hf)-(OH)2; xiii) UiO-66(Hf)-NH2; xiv) UiO-66(Hf)-(COOH)2; xv) UiO-66(Hf)-(F)4. Elastic modulus mapping of xvi) UiO-66(Hf); xvii) UiO-66(Hf)-(OH)2; xviii) UiO-66(Hf)-NH2; xix) UiO-66(Hf)-(COOH)2; xx) UiO-66(Hf)-(F)4.[291] b) Distribution curves of AM-FM stiffness maps of i) UiO-66(Hf/Zr). ii) CDF curves of the distribution curves presented in (i). iii) Distribution curves of UiO-66(Hf)-type MOFs. iv) Distribution curves of UiO-66(Zr)-type MOFs. Reproduced with permission.[291] Copyright 2017, American Chemical Society. c) Young's modulus image of a metal−organic framework. i) Top view structure of the MOF. Atom colors: Ce, green; S, yellow; O, red; C, gray; H, white. ii) Side view structure of the MOF. iii) Bimodal AFM image (topography) of a section of the MOF surface. iv) Height cross-section along the line marked in (c). v) Sub-nanometre resolved map of the area of the MOF marked in (iii). vi) Angstrom-resolved bimodal (topographic) image of the region of the MOF marked in (v). vii) Stiffness map of the region shown in (vi).[281] d) The MOF structure on the basal plane has been overlaid. Cross-sections and statistical Young's modulus curves. i) Topography and Young's modulus cross-sections along the dashed lines parallel to the b lattice vector. ii) Topography and Young's modulus cross-sections along the dashed lines parallel to the c lattice vector. iii) Statistic elastic modulus values obtained over the region shown in Figure (c)-(vii). iv) Atomic structure associated with a Young's modulus of 27.5 GPa. v) Proposed atomic structure for the locations that give a Young's modulus of 29.3 Gpa. vi) Atomic structure associated with the positions that give a Young's modulus of 32.3 Gpa. In panels (v) and (vi), we have omitted all H atoms for clarity. Atom colors: Ce, green; S, yellow; O, red; C, gray; H, white. Reproduced with permission.[281] Copyright 2017, American Chemical Society.

ical properties through varying metal nodes or modifying ligand chemical functionalities. For instance, incorporating sterically bulky functional groups increases the atomic density and subsequently boosts the mechanical properties of UiO-66-type MOFs (Figure 19). Furthermore, bimodal AFM was used to determine the Young's modulus of MOFs containing cerium atoms surrounded by oxygen and sulfur atoms[281] (Figure 19). Results indicate that Ce atoms are stiffer than carbon linkers, with the softest regions found between carbon rings. Variations in stiffness near Ce atoms suggest that the type and number of surrounding atoms influence Ce atom elasticity. **Table 9** provides a

summary of different AFM modalities applied in MOF and MOF derivative studies.

3.1.5. Profilometry

Profilometry is a technique used to extract and analyze surface roughness and topographical data from materials. This method can be performed using either a physical probe (stylus) or light (optical profilometry) to probe and quantify the sample surface topography. In MOF applications, profilometers

**ADVANCED
SCIENCE NEWS**

www.advancedsciencenews.com

NANO · MICRO

small

www.small-journal.com

Table 9. Examples of AFM modalities applications in MOF/MOF-derived materials.

| AFM Mode	Medium	Application/Reported Data	Other Techniques	Refs.
Tapping mode (AM-AFM)	Different MOFs in air and ambient conditions	3D Imaging and thickness measurements	XRD, TEM, SEM, GIXRD, XPS, DR-UV-Vis, FTIR, etc	[287]
Conductive Mode	CoNi-MOF in air	In-situ imaging	TEM, XRD, XPS, SEM, EDS	[282]
FM-AFM	DCA3Co2 MOF in ambient condition	Imaging, formation of a 2D band structure in the MOF decoupled from the substrate	STM, DFT	[293]
Electrochemical AFM	Cu MOF HKUST-1 in electrochemistry tapping fluid cell	Study height image and electrochemical growth	Electrochemical Raman spectroscopy	[283]
AFM-IR	HKUST-1 in Cu-BTC solution	Imaging, study the nucleation and growth process, study the impact of temperature on thin film formation	IRRAS, XRD, SEM-EDX	[284]
Bimodal AM-FM	UiO-66-type MOFs, HKUST-1 & MOF consists of groups of cerium, oxygen, and sulfur atoms are joined by organic linkers in air	Imaging and mechanical maps	NA	[281,291]
AFM Nanoindentation	ZIF-8 in air	Quantitative measurements of fine-scale MOF crystals.	SEM, XRD	[360]

are typically used for microscale measurements with nanometre resolution.[235]

For instance, optical profilometry can determine the average surface roughness of the Cu-BTC framework (HKUST-1), which is 2.23 ± 0.24 μm, showing higher roughness compared to native Cu foil (**Figure 20** and **Table 10**).[294] It's important to note that while profilometry provides valuable surface information, it does not directly reveal atomic-scale structural details like X-ray diffraction or AFM.

3.1.6. Fluorescent Microscopy

Fluorescence microscopy is a technique used in light microscopes that involves exciting fluorophores and detecting their emitted fluorescence. In the context of MOFs, it's useful for visualizing guest molecule loading, assessing their distribution within MOFs, and examining post-synthetic modifications on MOF crystal surfaces. This is achieved using luminescent or colored dyes with various sizes and functional groups. However, it's important to note that fluorescence microscopy has a limitation known as the diffraction limit, which restricts its resolution.[295] To overcome this limitation, advanced techniques have been developed to enhance microscope functionality, resolution, and sensitivity.[296] One such technique is Stimulated Emission Depletion (STED) microscopy, which employs two laser beams: an excitation beam to activate fluorophores and a depletive doughnut-shaped laser to suppress fluorescence around the excitation point. STED microscopy achieves resolutions between 20 and 80 nm but requires specialized equipment and suitable fluorophores for the depletion process, and it can be susceptible to photobleaching and phototoxicity due to the high-intensity depletion laser.[297] Structured Illumination Microscopy (SIM) is another method for achieving high-resolution images by utilizing structured light patterns during specimen illumination.[298] SIM generates an interference pattern known as Moiré fringes[299]
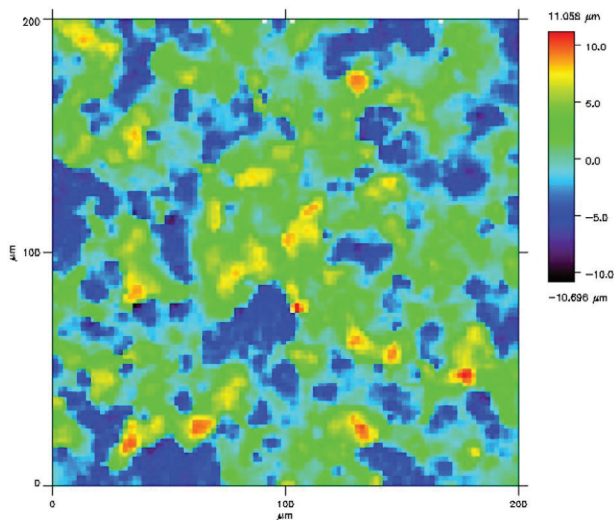
Figure 20. Optical profilometry image of an electrodeposited MOF film. Reproduced with permission.[294] Copyright 2018, Springer Nature.

Table 10. Optical profilometry of an electrodeposited MOF film. Surface roughness parameters Ra (arithmetical average roughness), Rq (root mean squared roughness), Rp (maximum peak height), and RV (maximum valley depth) for native Cu foil and electrodeposited Cu-BTC films.

Sample	Scan length [mm]	R_a [μm]	R_q [μm]	R_p [μm]	R_v [μm]
Cu foil	1.0	0.24	0.47	10.68	4.81
Cu-BTC film	1.0	1.92	2.43	10.64	8.50
Cu-BTC film	1.0	2.30	2.86	12.08	10.02
Cu-BTC film	0.2	2.48	3.05	10.57	8.59
Cu-BTC film average		2.23 ± 0.24	2.78 ± 0.26	11.1 ± 0.7	9.04 ± 0.7

**ADVANCED
SCIENCE NEWS**

www.advancedsciencenews.com

NANO · MICRO

small

www.small-journal.com

when imaging features smaller than the diffraction limit. This technique can provide images with a resolution of 100–150 nm but necessitates specialized hardware and data processing algorithms. It may have limitations in imaging thick samples or highly complex MOF structures compared to confocal microscopy due to reduced optical sectioning.

As an example of fluorescent microscopy techniques in MOF applications, Ma et al.[300] used fluorescence microscopy and confocal laser scanning microscopy to visualize fluorescent dye locations within MOF crystals and demonstrated selective post-synthetic covalent modification of MOF crystal surfaces. Schrimpf et al.[301] employed fluorescence imaging and lifetime analysis to investigate the spatial arrangement of functionalities and defect levels within a multivariable MOF crystal, focusing on UiO-67. Ameloot et al.[302] utilized confocal fluorescence microscopy to map the three-dimensional structures of defects in single crystals of HKUST-1 and MOF-5 based on carboxylate linkers (**Figure 21**). Additionally, Rosario et al.[303] used fluorescence microscopy to show that filamentous fungi emit green or red light after accumulating particulate lanthanide metal–organic frameworks on their cell walls. Schunter et al.[304] explored the ubiquitylation process of the acetyltransferase MOF in Drosophila melanogaster using fluorescence microscopy. By tracking the localization and behavior of ubiquitylated MOF within cells, they gained insights into the spatial and temporal aspects of MOF ubiquitylation, providing a deeper understanding of its regulation and functional consequences. Generally, fluorescence and super-resolution microscopy techniques enable the examination of MOF distribution within living cells and provide insights into their localization patterns, movement, trafficking, and interactions within cells. By tagging MOF derivatives with fluorescent markers, it can be possible to visualize their behavior and co-localization with specific cellular components, enhancing our understanding of MOF functionality in biological contexts.

3.1.7. Positron Annihilation Spectroscopy (PAS)

PAS is a non-destructive method used to study vacancy-type defects. Positrons are antiparticles of electrons with the same mass but opposite charge. When a specimen is exposed to positrons, it becomes thermalized and subsequently annihilates with electrons, emitting gamma rays in the process. The collected gamma rays provide information about the positron lifetime, allowing for the identification of defect types and their relative concentrations. By plotting positron lifetime against emitted gamma-ray signals, a PAS spectrum is generated. This technique can be employed to compare the ortho-positronium lifetime of MOFs with their pore size and determine the specific location of metal nanoparticles relative to the MOF structure.[235] Additionally, by incorporating positron-emitting isotopes into guest molecules, PAS can be used to trace the diffusion and adsorption behavior of these molecules within MOF-derivative structures. Another valuable application of PAS in the study of MOF derivatives is its ability to monitor structural transformations under external stimuli, such as temperature variations, pressure changes, or exposure to different environments. These transformations are tracked by observing changes in positron lifetime or annihilation characteristics. As an example Chen et al.[305] utilized PAS to characterize
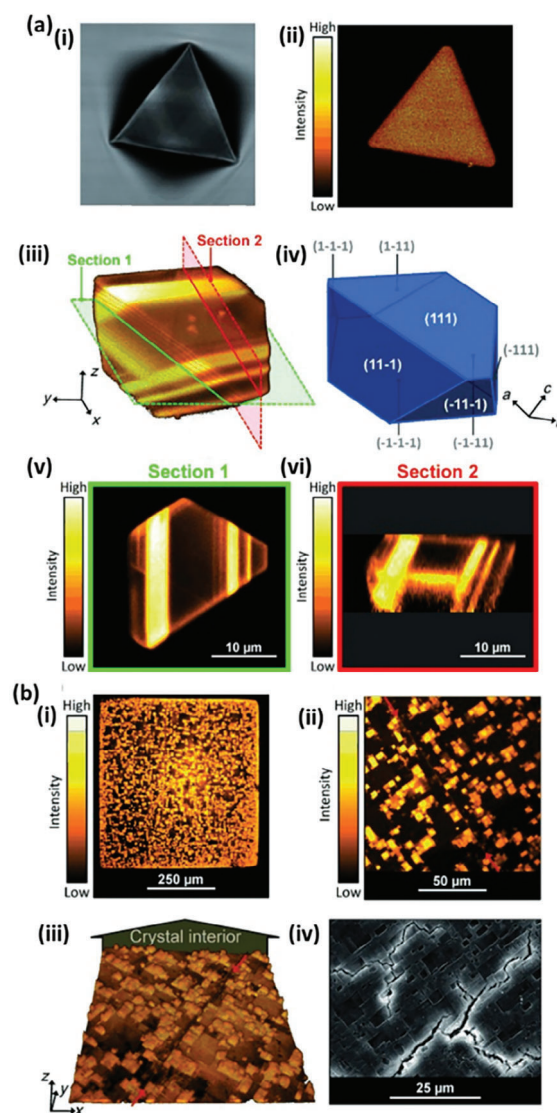
Figure 21. a) Images of HKUST-1 single crystals captured by confocal fluorescence illustrate the presence of defects upon extending crystallization time. i) Transmission micrograph of a HKUST-1 crystal acquired after a short crystallization time. ii) Fluorescence micrograph of the surface of the same crystal illustrating the absence of defects. iii) Fluorescence data captured from HKUST-1 crystal after extended crystallization time. Semitransparent 3D reconstruction of the fluorescence data captured as a series of xy-scans along the z-axis. Locations of xy- and xz-sections shown in panels (v) and (vi), respectively, are indicated. iv) Schematic of the single crystal illustrated in panel (iii) with indication of the limiting crystal planes and crystallographic axes. v) As-recorded xy-section. The crystal boundaries in this 2D section are all parallel to the ⟨110⟩ directions. vi) xz-section represented the data shown in panel (c) and visualizing the angles between the crystal's exterior surface and defect planes propagating in the crystal's interior. b) Confocal fluorescence mapping of defects in a MOF-5 single crystal. i) Overview fluorescence micrograph of the outer surface of a large cubic MOF-5 crystal. ii) Fluorescence micrograph details of the crystal facet illustrated in panel (i). The red arrows indicate a line defect. iii) 3D reconstruction of the fluorescence data presented in panel (ii), show the penetration of defects into the crystal interior. To compare, the same line defect as in panel (ii) is indicated with red arrows. iv) Electron micrograph of a similar MOF-5 crystal showing the large irregular cracks formed upon drying. Reproduced with permission.[302] Copyright 2013, Wiley.
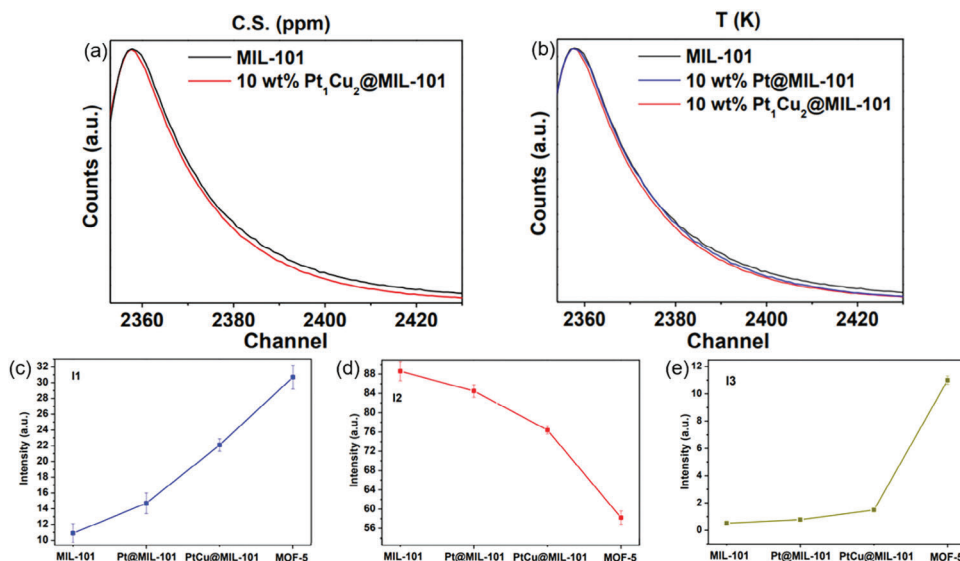
Figure 22. a) Positron lifetime spectra for MIL-101 and 10 wt% Pt1Cu2@MIL-101. b) Positron lifetime spectra for MIL-101, 10 wt% Pt@MIL-101 and 10 wt% Pt1Cu2@MIL-101. c–e) The intensities of I1, I2 and I3 with error for MIL-101, Pt@MIL-101, PtCu@MIL-101 and MOF-5. The error-bars are standard errors of the mean. Reproduced with permission.[305] Copyright 2017, Springer Nature.

the location of Pt and PtCu NPs relative to the host MOF particles (PtCu@MIL-101, Pt@MIL-101, and MIL-101; **Figure 22**). The results demonstrate similarly measured lifetimes ($\tau 1$, $\tau 2$, and $\tau 3$) for three samples, while there is a change in intensities after loading Pt or PtCu NPs inside the MOF pores, especially for PtCu@MIL-101. However, there are some challenges in using PAS to study MOF-derivatives. One such challenge lies in the limited availability of positron sources and the complexity of experimental setups required for PAS analysis. Additionally, the interpretation of PAS data in the context of MOF derivatives can be challenging due to the diverse nature of these materials and the complex interactions between positrons and their surroundings.

3.1.8. Electron Paramagnetic Resonance

Electron Paramagnetic Resonance (EPR), also known as Electron Spin Resonance Spectroscopy (ESR), is a method used to analyze materials containing unpaired electrons. EPR shares its fundamental principle with Nuclear Magnetic Resonance (NMR), but in EPR, it's the electrons, not atomic nuclei, that are excited. In this technique, a magnetic field is applied to the electrons, which possess magnetic dipoles aligned either parallel or antiparallel to the direction of the magnetic field. The EPR spectrum is recorded by plotting the optical absorption vs magnetic field strength by changing the magnetic field. EPR spectroscopy is particularly useful to investigate the coordination environment and behavior of metal ions within MOF-derivatives,[306] detection and characterization of ligand radicals,[307] defects within MOF-derivatives,[308] as well as analyzing the magnetic interactions between paramagnetic centers within MOF-derivatives.[309] In a study by Mendt et al.[306] the adsorption of nitric oxide (NO) on both the flexible and rigid forms of DUT-8(Ni) was investigated using continuous wave electron paramagnetic resonance (EPR) spectroscopy at X-band frequency. They observed a hysteresis loop in the intensity of adsorption and desorption for the flexible form of DUT-8(Ni), but not for the rigid form. This disparity suggests that the difference in flexibility between the two materials plays a role in their adsorption behavior. Additionally, they measured EPR signals with an electron spin S = 1/2, which are likely attributed to Ni^{2+}-NO adsorption complexes at defective paddle wheel units within the porous phase of DUT-8(Ni). In these complexes, the unpaired electron is located at the Ni^{2+} ion.

Furthermore, EPR was successfully employed to inspect the incorporation and coordination state of the Cu^{2+} ions in the $^3_\infty[Cd_{0.98}Cu_{0.02}(prz\text{-}trz\text{-}ia)]$ porous MOF[310] and $_\infty^3[Cu_2{}^ICu_2{}^{II}\{H_2O\}_2\{(Me\text{-}trz\text{-}m\text{ba})_2\text{thio}\}_2]Cl_2$[311] (**Figure 23**). The EPR measurements have been performed on powder samples and single crystals and exhibited the full electron Zeeman g and copper hyperfine A^{Cu} interaction tensors including the orientation of their principal axes frames[310] as well as the exchange of the spin triplets between neighboring Cu2 PW units.[311]

Although EPR was successfully utilized in studying MOF and its derivatives, still there are some challenges remain. One significant challenge lies in the sensitivity of EPR to paramagnetic species, which may be present in low concentrations or masked by background signals in MOF derivatives. Additionally, the need for specialized equipment and expertise in EPR spectroscopy can limit its accessibility to researchers. Furthermore, the interpretation of EPR spectra in the context of MOF derivatives can be complex due to the intricate interplay between molecular structure, guest-host interactions, and environmental factors.

3.2. Characterization of Physical and Electrochemical Properties

Understanding the physical and electrochemical properties of MOFs and their derivatives is crucial for their broad applications

**ADVANCED
SCIENCE NEWS**

www.advancedsciencenews.com

**NANO · MICRO
small**

www.small-journal.com
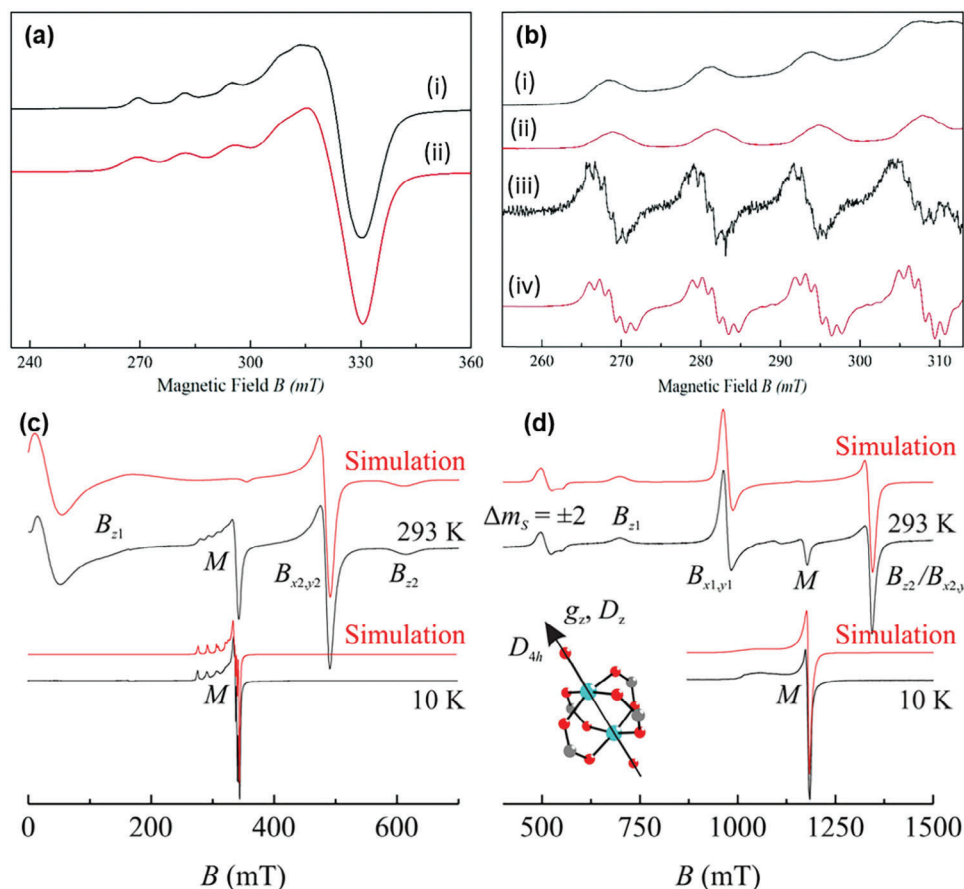
Figure 23. a) X-Band EPR spectra of an asCu$_{0.02}$Cd powder captured at 20 K: i) measured and ii) simulated spectrum. b) X-Band EPR spectra of an asCu$_{0.02}$Cd powder captured at 20 K illustrating the g$_{\parallel}$ spectral area with resolved ^{14}N shf splitting: (i and iii) measured and corresponding (ii and iv) simulated first and second derivative spectra. Reproduced with permission.[310] Copyright 2017, The Royal Society of Chemistry. c,d) Normalized experimental (black) and simulated (red) (C) X-band and (D) Q-band spectra of powder sample 2 at 10 K and room temperature. The M-symbol marks the line of mononuclear Cu^{2+} ions. The PW unit with collinear gz and Dz principal axes of Cu^{2+} pair g- and D-tensors are also indicated in (d). Reproduced with permission.[311] Copyright 2015, American Chemical Society.

in energy conversion, energy storage, chemical sensing, gas adsorption and desorption, gas storage, drug delivery, catalysis, and optoelectronics. To determine and characterize these properties, including optical and adsorption behavior, thermal and colloidal stability, apparent surface area, and porosity, various characterization techniques and analytical instruments are employed. In the following section, we will review and emphasize the commonly used methods and their applications for characterizing the physical and electrochemical properties of MOFs.

3.2.1. Surface Area and Porosity Characterization of MOFs and its Derivatives

Adsorption/desorption isotherms reveal essential information about material textural properties.[312] The widely adopted technique for assessing surface areas, pore volumes, average pore size, and pore size distributions in MOFs is nitrogen (N$_2$) gas adsorption at 77 K.[313] This method involves studying the N$_2$ adsorption isotherm, which tracks N$_2$ adsorption as a function of pressure at the boiling temperature. To obtain meaningful

data, proper activation of the MOF is essential.[313] Initially, samples undergo outgassing in a vacuum at a specific temperature to remove trapped adsorbate molecules in the pores. The outgassing temperature choice is vital; high temperatures can harm MOFs, while low temperatures result in incomplete outgassing. Typically, degassing temperatures range from 120 to 150 °C, depending on the MOF.[314–316] Next, a sample cell with a known weight is cooled to 77 K and exposed to a specific N$_2$ amount. After temperature and pressure stabilize, the isotherm records adsorption until the adsorbent surface is fully covered. Then, nitrogen is gradually removed from the cell to initiate desorption.[317]

The International Union of Pure and Applied Chemistry (IUPAC) classifies adsorption isotherms into six groups based on their shape, aiding porous material categorization (see **Figure 24**).

Based on the classification, monolayer microporous solids with pores smaller than 2 nm produce Type I isotherms, characterized by a sharp initial gas adsorption increase followed by a saturation plateau. For example, nitrogen adsorption on MOF-5 displays a Type I isotherm, indicating monolayer formation.[245]

**ADVANCED
SCIENCE NEWS**

www.advancedsciencenews.com

NANO · MICRO
small

www.small-journal.com
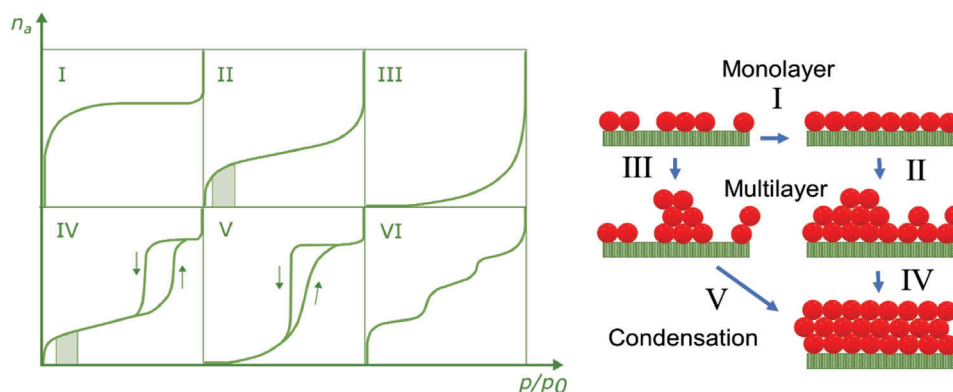
Figure 24. Schematic presentation of IUPAC classification of adsorption isotherms (typical BET range is illustrated in Types II and IV by the shaded areas) n_a is quantity of absorbed gas, p/p_0 is the relative pressure.

Type II isotherms result from nonporous or macroporous samples with pores larger than 50 nm, allowing multilayer adsorption. In MOFs like MIL-101(Cr), nitrogen adsorption creates a Type II isotherm due to its mesoporous structure.[318]

Type III isotherms, although rare, occur when adsorbate-adsorbate interactions outweigh adsorbate-adsorbent interactions. An example is nitrogen adsorption on Al-MIL-53, a nonporous MOF derivative.[319]

Mesoporous materials with 2–50 nm pores exhibit Type IV isotherms. They feature monolayer-multilayer adsorption at lower pressures and capillary condensation in mesopores at higher pressures. UiO-66 shows a Type IV isotherm due to micropores and mesopores.[319]

Type V isotherms emerge in mesoporous materials with weak adsorbate interactions. Materials with uniform surfaces exhibit Type VI isotherms. MOF-derivatives like MOF-177 with high surface area and pore volume display Type V isotherms, indicating multilayer adsorption.[320]

To calculate apparent surface area, the most common approach reported so far is Brunauer–Emmett–Teller (BET) theory[321] as multilayer gas adsorption adapts to pore sizes of most MOFs. However, as the BET model is more appropriate for flat surfaces for complex 3D MOFs, it may require modification.[322] So, the excess sorption work (ESW) method or integration with BET is proposed for accurate surface area determination, especially in cases where the structures show relatively less complex isotherms having distinct steps associated with mono/multilayer loading.[323]

For example, it is shown in the case that the pore filling and monolayer formation become indistinguishable and cannot be differentiated on the basis of isotherm data, the BET method significantly overestimates the surface area.[324] This is because the BET method includes non-monolayer adsorbate molecules as monolayer loading which can be called pore-filling contamination. Same to the BET approach, the N_2 adsorption isotherm can be used to capture the information on the pore volume and pore size distribution of MOFs by employing mathematical modeling. The most common computing methods are density functional theory[325] mostly utilized for analyzing meso/micropores, Barrett– Joyner–Halenda method[326] applicable only for mesopores and Horwath–Kawazoe (HK)[327] used for micropores. However, the accuracy of results is dependent on the sensitiv-

ity of equipment and the reliability of experimental data. Banerjee et al.[72] have performed the BET surface area measurements for the zinc-based MOF (MOF-5) derived carbon (MOF-DC) and exhibited the N_2 adsorption/desorption isotherms alongside pore size distribution (**Figure 25a**). The results identify the high concentration of micropores as well as the existence of mesoporosity. Self-activation of Zn and its evaporation during the carbonization process causes such pore formation. The N_2 adsorption/desorption experiments on nano-SnO_2 derived from tin metal–organic frameworks identify the uniformity of spherical SnO_2 nanoparticles with an average 40 nm diameter (Figure 25b).[155] The nitrogen sorption isotherm results of MHPCS and MHPCS/Se clearly exhibit a substantial reduction of surface area after infusion of Se in MHPCS. It can be explained by the occupation of almost all pores of the carbon sphere by Se.[201]

In addition to Tables 1 and 2 that show the surface area of some MOF-derivatives, Table 13 summarizes the specific details obtained through surface area and porosity characterization techniques applied to different MOF and MOF-derivatives. It is depicted that in the case of MOF-derived materials, the surface area is reduced. This phenomenon can be explained by considering various factors such as thermal decomposition, agglomeration of particles, collapse of the pore structure, and sintering during synthesis. The removal of organic linkers and the formation of larger metal oxide particles result in fewer exposed surfaces available for interaction, leading to a reduction in surface area compared to the porous structure of the original MOF. Furthermore, the MOF-derived metal oxide shows less surface area in comparison with MOF-derived porous carbon materials (**Table 11**).

3.2.2. Volumetric and Calorimetric Measurements

Calorimeters are used to measure heat transfer and evaluate MOFs' adsorption properties. MOF adsorption studies provide insights into porosity, essential for applications like gas storage.[334] Calorimetry relies on a temperature sensor and heater element. In standard conditions, the temperature difference between heated and unheated states is measured. In varying medium conditions, the temperature difference changes with the flow rate. Wu et al.[335] conducted CO_2 adsorption calorimetry at 25 °C on CD-MOF-2. They discovered two distinct
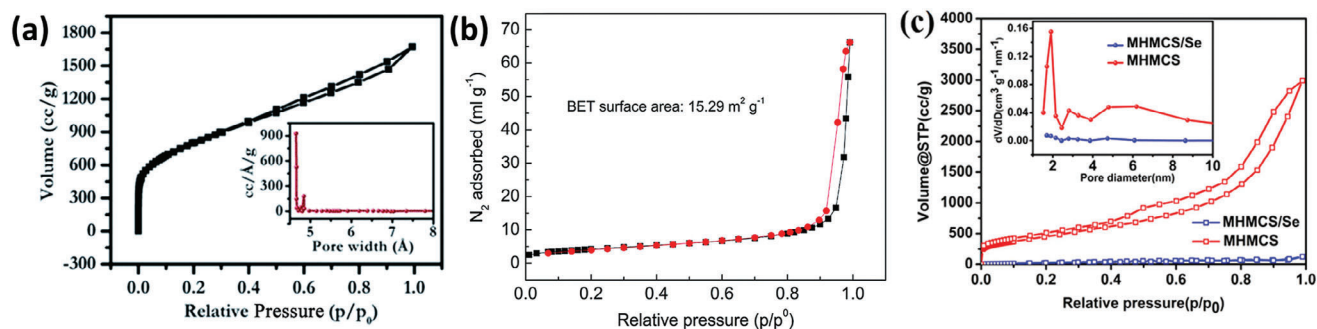
Figure 25. a) N_2 adsorption/desorption isotherms of MOF-DC, inset: pore size distribution. Reproduced with permission.[72] Copyright 2014, The Royal Society of Chemistry. b) N_2 adsorption–desorption measurement of the nano-SnO_2. Reproduced with permission.[155] Copyright 2015, The Royal Society of Chemistry. c) Nitrogen sorption isotherm and pore size distribution of MHPCS and MHPCS/Se composite. Reproduced with permission.[201] Copyright 2016, American Chemical Society.

binding sites for CO_2 adsorption, confirmed by calorimetric data (**Figure 26**). Their method involved three steps: 1) Placing 30 mg of CD-MOF-2 in a silica glass tube connected to a gas analyzer. 2) Vacuum degassing for 12 h at room temperature to remove adsorbed species. 3) Placing the tube in the calorimeter after 12 h at 25 °C for CO_2 adsorption. Figure 26a,b displays adsorption isotherms and calorimetric traces for the first and second CO_2 adsorption rounds. The initial steep gas curve in the low-pressure region (Type I isotherm) indicates a strong chemical interaction between CD-MOF-2 and CO_2 at room temperature. Subsequent adsorption doses reduce the calorimetric peak, signifying less exothermic differential enthalpy with increasing CO_2 coverage. Figure 26c illustrates the differential enthalpy of CO_2 adsorption versus surface coverage (CO_2 per nm^2) for the first (black), second (red), and third (blue) adsorption rounds.

For the case of MOF derivatives, volumetric measurements can be used to determine the gas capacity, adsorption kinetics, and the nature of the adsorption process in MOF derivatives. For example, through volumetric measurements, the hydrogen uptake capacity in MOF-5 as 3.8 wt% at 77 K and 10 MPa was determined.[336,337] Furthermore, using volumetric measurements it has been shown that the MOF-74 series exhibits high hydrogen uptake capacities, with MOF-74-Mg (Fe2(dobdc)) reaching up to 2.2 wt% at 77 K and 1.2 bar.[338] Zhao et al.[338] provided a comprehensive table describing the H_2 adsorption properties of MOFs. Despite the successful implementation of volumetric and calorimetric measurements in evaluating MOF-derivatives adsorption, still there are challenges that primarily revolve around the accurate determination of the true volume of porous MOF/derivative structures due to factors like adsorption, desorption, and the presence of solvent molecules. To mitigate these challenges, techniques such as gas or liquid displacement methods to measure the volume of MOF-derived samples can be employed. These methods involve introducing a known volume of gas or liquid into the MOF/derivative structure and measuring the displacement, allowing for a more accurate determination of the sample's true volume. Additionally, strategies like degassing and solvent exchange are employed to remove solvent molecules or residual solvents from the MOF/derivative structure before conducting volumetric and calorimetric measurements, minimizing their influence on the results.

In addition of determination of gas capacity, volumetric measurements can provide insights into the selectivity of MOF-derivatives towards specific gases. By comparing the adsorption of different gases, such as CO_2, N_2, and CH_4, the selectivity of the MOF material can be determined. Examples are the selectivity of MOF-5 toward CO_2 over N_2, where volumetric measurements have shown a higher CO_2 adsorption capacity[339] as well as the selectivity of MOF-74 toward CO_2 over N_2.[339]

3.2.3. Thermogravimetric Analysis

Thermal stability and solvent-accessible pore volume of MOFs are determined using thermogravimetric analysis (TGA).[340] TGA involves heating a sample at a controlled rate under a

Table 11. Examples of surface area and pore volume of different MOF and MOF-derived materials.

MOF	Surface area [S_{BET} m^2 g^{-1}] and pore volume [cm^3 g^{-1}]						Refs.
	MOF		MOF-derived carbon		MOF-derived metal oxide		
	[m^2 g^{-1}]	[cm^3 g^{-1}]	[m^2 g^{-1}]	[cm^3 g^{-1}]	[m^2 g^{-1}]	[cm^3 g^{-1}]	
MOF-5	3465	1.4	1880	2.22	11	0.02	[328,61,157]
MIL-199	1553	0.687	1370	0.57	39	–	[329,98,115]
ZIF-8	1470	0.69	1067	0.69	579	2.15	[330,96,158]
ZIF-67	1319	0.61	943	0.84	148	–	[330,331,97]
MIL-88-Fe	1242	0.7	484	0.923	75	–	[332,333,111]

ADVANCED
SCIENCE NEWS

www.advancedsciencenews.com

NANO · MICRO
small

www.small-journal.com
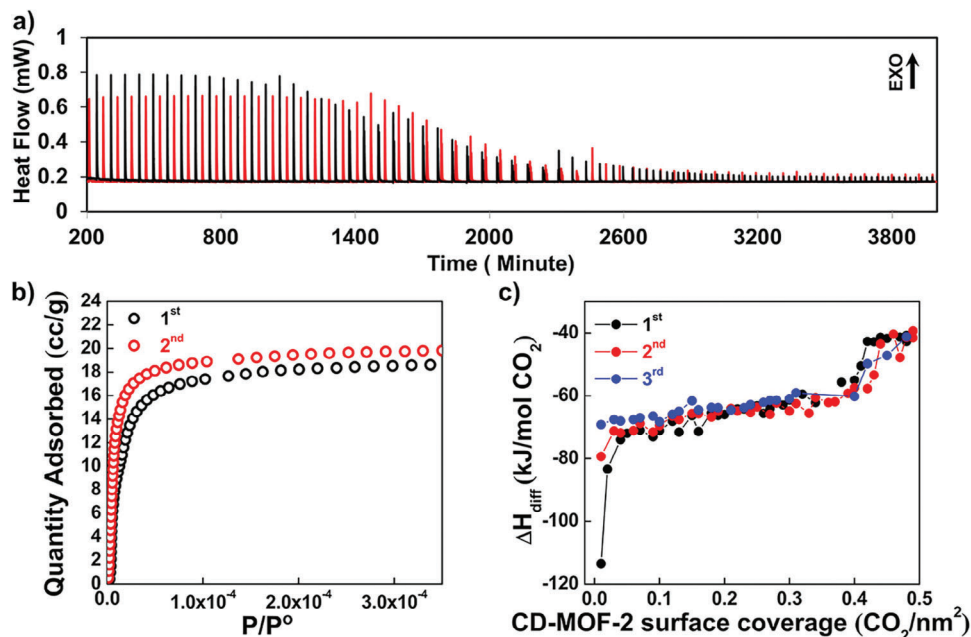
Figure 26. a) CO_2 adsorption isotherms and b) associated calorimetric traces (at 25 °C) for the first (black) and second (red) CO_2 adsorption on the same CD-MOF-2 sample (after degassing at 25 °C for 12 h). c) Differential enthalpies of CO_2 adsorption (at 25 °C) for the first (black), second (red), and third (blue) rounds of adsorption on the same CD-MOF-2 sample. Reproduced with permission.[335] Copyright 2013, American Chemical Society.

specific atmosphere, recording mass loss. Several distinct steps occur during TGA: initial desolvation below 150 °C, followed by a stable plateau when the MOF is solvent-free, and eventually, a second mass loss indicating framework degradation. (See **Figure 27** for HKUST-1[341] and NU-1000 under N_2 and air[313]).

The decomposition pathway of MOF during TGA varies with the carrier gas (e.g., air, O_2, or N_2) used (Figure 27c). To confirm thermal stability and understand mass changes better, complementary techniques like in-situ PXRD[342] and mass spectrometry[343] are recommended alongside TGA. TGA analysis reveals that factors like metal hardness, coordinated solvent molecules, functional group nature and position, interpenetration, and isoreticular expansion all influence MOF thermal stability.[341] However, distinguishing between plateau regions and decomposition features is challenging due to the convolution of desolvation and decomposition. Furthermore, TGA of solvated samples can estimate pore volume.[313] This estimation relies on correlating mass loss with trapped solvent in the pores. To achieve this, MOFs are soaked in a high-boiling-point solvent and quickly filtered to remove untrapped solvent molecules in the pores, attributing the post-filtering mass loss to the void space within the MOF.[313] It's essential to note that while TGA can be used for both MOFs and MOF derivatives, the presence of functional groups or modifications in derivatives can lead to distinct thermal behaviors compared to pristine MOFs. TGA is also valuable in assessing the thermal stability of MOF-derived materials, such as carbonaceous materials resulting from pyrolysis or other thermal treatments of MOFs. As thermal instability, decomposition, and solvent residues can influence TGA analysis and lead to inaccurate measurements of weight loss and thermal behavior, utilizing vacuum or inert gas purging during analysis can

minimize thermal degradation and remove volatile components. Additionally, conducting TGA under controlled heating rates and using suitable reference materials can enhance the reliability of results.

3.2.4. UV–Vis Diffuse Reflectance Spectroscopy (UV–vis DRS)

UV–vis Diffuse Reflectance Spectroscopy (UV–vis DRS) is a simple method for analyzing powders and surfaces without extensive sample preparation.[344] It works by directing light onto a specimen at a specific angle, causing the sample to reflect radiation in all directions. The reflected radiation from the sample includes both regular and diffuse reflectance.[344] Regular reflectance occurs when incident radiation is reflected at the same angle on a smooth, planar surface. In contrast, diffuse reflection occurs when scattering or multiple reflections disperse radiation in all directions across a hemisphere of incident radiation. Since diffuse reflection depends on the specimen's surface properties, it provides more information.[345] UV–vis DRS is widely used to characterize the optical properties of MOFs. MOFs contain metal oxo-clusters and organic linkers, resulting in electronic transitions between the valence band and conductive band of metal oxo-clusters or between the highest occupied molecular orbital (HOMO) and lowest unoccupied molecular orbital (LUMO) of organic linkers when exposed to light with the appropriate energy.[346] This leads to the formation of an absorption spectrum with multiple bands, depending on the constituents promoting electron transitions. Additionally, UV-vis DRS is valuable for studying electronic properties, ligand interactions, and photochemical reactions in MOF derivatives. By analyzing absorption peaks and their wavelengths, it is

ADVANCED
SCIENCE NEWS
www.advancedsciencenews.com

NANO · MICRO
small
www.small-journal.com
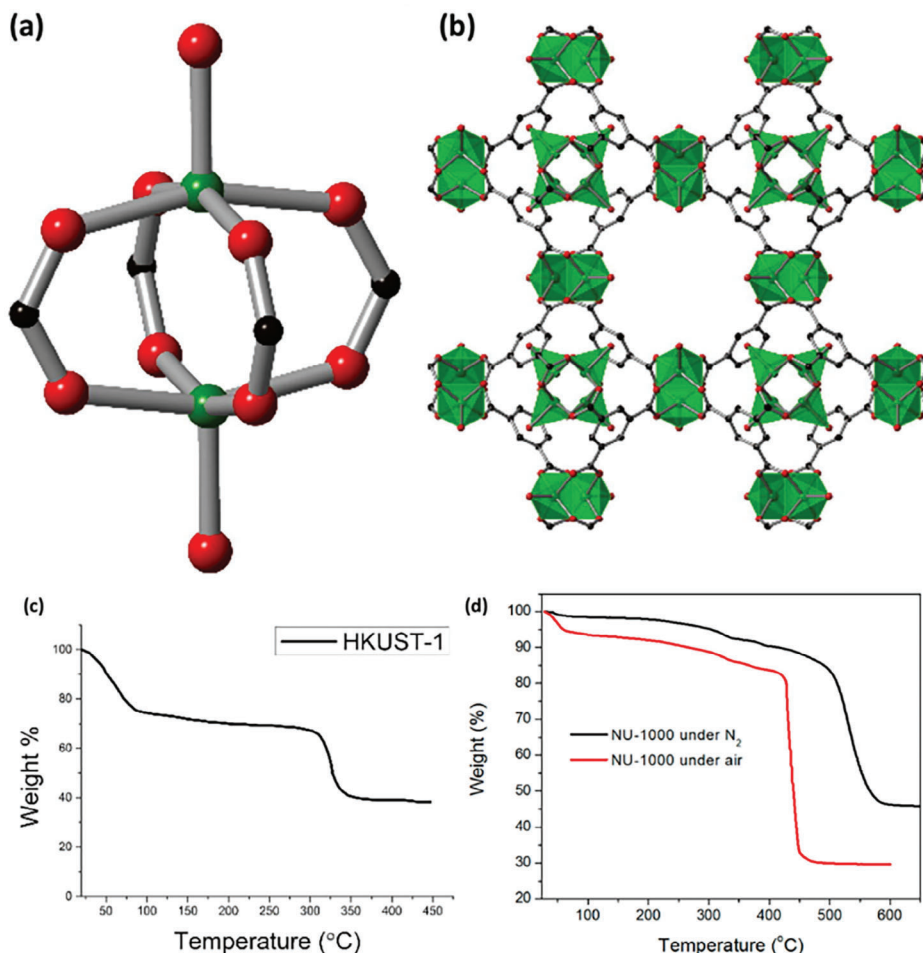
Figure 27. a) Copper paddle-wheel SBU in HKUST. b) A unit cell of the material. c) Thermogravimetric Analysis (TGA) of HKUST-1. Reproduced with permission.[341] Copyright 2020, Elsevier. d) Low-temperature de-solvation is observed (<125 °C), followed by a plateau region, followed by a secondary mass loss step beginning at 300 °C, which is assigned as the temperature of decomposition (T_d). Cu – green, O – red, C – grey, H – omitted. Thermogravimetric analysis curve showing weight % versus temperature taken under N2 and air. MOF used is NU-1000. Reproduced with permission.[313] Copyright 2017, American Chemical Society.

possible to determine the nature of electronic transitions, such as charge transfers or ligand-to-metal and metal-to-ligand transitions in MOF derivatives. This information enhances our understanding of the optical properties and potential functions of MOF derivatives. Furthermore, UV–vis DRS can reveal structural changes or interactions between MOF derivatives and guest molecules or ligands. Modifications in the absorption spectrum, such as shifts or intensity changes, indicate alterations in the electronic environment due to guest molecule inclusion or ligand coordination.

Jia et al.[347] have used the UV–vis DRS measurements on g-C_3N_4, TiO_2, TCN4, TCN8, and TCN15 to assess the photocatalytic activity of the synthesized MOF derivatives (**Figure 28**). The UV–vis spectra exhibited wider visible-light absorption for TCN4, TCN8, and TCN15 than TiO_2 due to the presence of g-C_3N_4. It means the hybridized TiO_2 derived from the MIL-125 (Ti) with g-C_3N_4 has a higher visible-light-harvesting ability than pure TiO_2 that is affordable to increase the photocatalytic degradation activity.

3.2.5. Photoluminescence Spectroscopy (PLS)
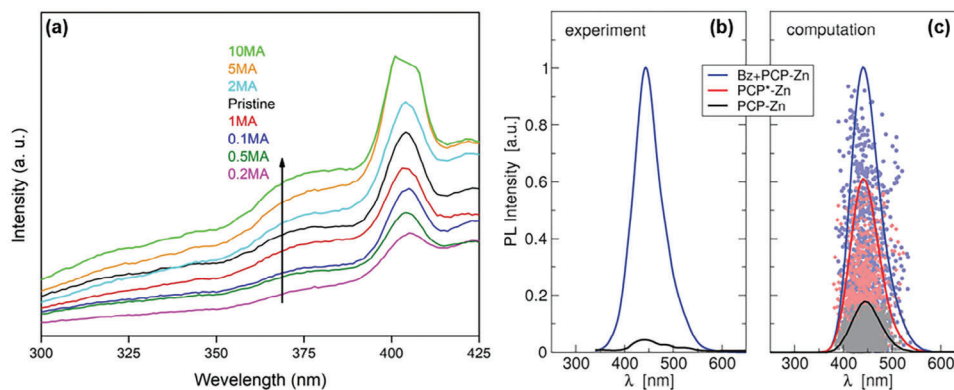
Photoluminescence Spectroscopy (PLS) uses laser irradiation to generate and collect light from a sample, revealing imperfections
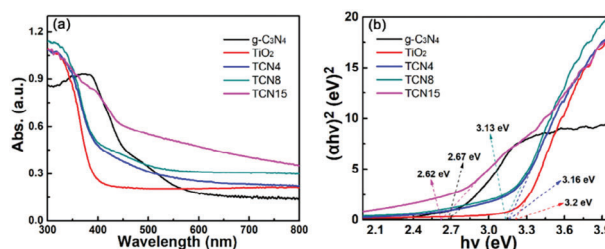
Figure 28. UV–vis diffuse reflectance spectra (DRS) (a) and Plot of $(\alpha h\nu)^2$ vs. $h\nu$ for the band gap energy (b) of TiO_2, g-C_3N_4, TCN4, TCN8, and TCN15. Reproduced with permission.[347] Copyright 2020, Springer Nature.

ADVANCED
SCIENCE NEWS
www.advancedsciencenews.com

NANO · MICRO
small
www.small-journal.com

Figure 29. a) Comparison of photoluminescence spectra of all prepared MIL-125 derived Mg^{2+} doped mesoporous TiO_2 photocatalysts. Reproduced with permission.[350] Copyright 2021, Wiley. b) The photoluminescence spectrum for PCP-Zn (black) and Bz+PCP-Zn (blue). The transition from "off" to "on" in photoluminescence is significantly clear.[351] c) The simulation results of the artificial system PCP*-Zn (red). Reproduced with permission.[351] Copyright 2019, American Chemical Society.

and impurities of the specimen.[348] It explores structural defects, oxygen vacancies, and photogenerated charge recombination in MOFs and derivatives, quantifying recombination centers based on spectrum intensity.[322] Photoluminescence in MOFs originates from metallic nodes, organic linkers, or their interactions.[349] PLS is used for MOFs and derivatives, but the focus differs intrinsic luminescent behavior and excited states in MOFs, while for derivatives, it centers on modifying luminescence for specific applications.

Figure 29a displays PLS results for charge recombination in Mg^{2+} doped mesoporous TiO_2 derived from MOF MIL-125.[350] Pristine mesoporous TiO_2 shows moderate PLS response, decreasing with lower Mg^{2+} doping. Above 0.5Mg, intensity increases due to surface defects and concentrated Mg^{2+} centers promoting charge recombination.

Jensen et al.[351] used PL spectroscopy to show the enhancement of the photoluminescence effect of Zn-based metal–organic framework (MOF) material $Zn_2(bdc)_2(dpNDI)$ (PCP-Zn) due to the adsorption of guest molecules resulting from an underlying guest-induced structural change. Furthermore, because of interactions of guest molecules with the framework, there would be a variation of emission color that changes the MOF electronic structure. Figure 29b,c clearly shows the effect of introducing the benzene guest molecule.

### 3.2.6. Transient Absorption Spectroscopy (TAS)

TIS is a versatile technique used to study transient states of photochemically/physically relevant molecules, allowing for the observation and characterization of their structural and electronic properties. In TAS, a brief laser pulse excites the sample, raising electrons to higher energy states. A time-delayed probe pulse is used to measure absorption changes over time. By varying the time delay, a time-resolved absorption spectrum is obtained, revealing insights into excited state dynamics. For MOFs, the focus is on understanding intrinsic excited state behavior, while for MOF derivatives, the analysis often explores the effects of modifications, guest molecules, or functional groups on excited state dynamics and photochemical reactivity.

To underly the efficacy of photoexcited charge separation of mesoporous zirconium–porphyrin MOF, PCN-222 (also called MOF-545 or MMPF-6), based on tetrakis (4-carboxyphenyl)-porphyrin (H2TCPP), Xu et al.[352] has performed the ultra-fast transient absorption (TA) spectroscopy (**Figure 30**). The results demonstrate the photocatalytic reduction of CO_2 under visible-light irradiation over photoactive porphyrin-based semiconducting MOF of PCN-222, with much higher activity than the H2TCPP ligand alone.[352] Furthermore, Santaclara et al.[353] used TAS to compare the photoexcitation of pristine NH_2-MIL-125(Ti) in DMF and its derivative **2**@NH_2-MIL-125(Ti) in dimethylformamide (DMF). As Figure 30c exhibits, despite the shape of the spectrum, the TAS spectrum of **2**@NH_2-MIL-125(Ti) in dimethylformamide (DMF) is very similar to the original from solely the MOF (Figure 30d). However, the decay of the induced absorbance corresponded to the photogenerated holes (at $\lambda = 570$ nm) on the MOF and on **2**@NH_2-MIL-125(Ti) is significantly different. Obviously, the decay of **2**@NH_2-MIL-125(Ti) is faster than the pristine MOF. It represents that a fraction of the holes on the MOF is most likely transferred to compound **2**.

3.2.7. Transient Photocurrent Spectroscopy Analysis

Transient photocurrent spectroscopy (TPS) assesses charge pair separation and stability. Photogenerated electrons move to the contact surface, while holes are absorbed by the electrolyte. Modulated light perturbs the sample, and time or frequency domain photocurrent data yields material insights. TPS reveals photoconductivity and charge transport in MOFs by illuminating them with a laser, creating charge carriers. An external field collects photocurrent over time, enabling the study of carrier dynamics, recombination, and extraction. The analysis yields data on carrier lifetime, mobility, and recombination kinetics. TPS examines carrier dynamics, transport, and recombination in MOFs and MOF derivatives. MOF analysis by TPS focuses on intrinsic transport and recombination, while analysis of MOF derivative with TPS explores modifications, guest molecules, or interfacial effects.

TPS has been utilized to exhibit the charge separation and charge transfer process of the MIL-53(Fe)/hydrated and
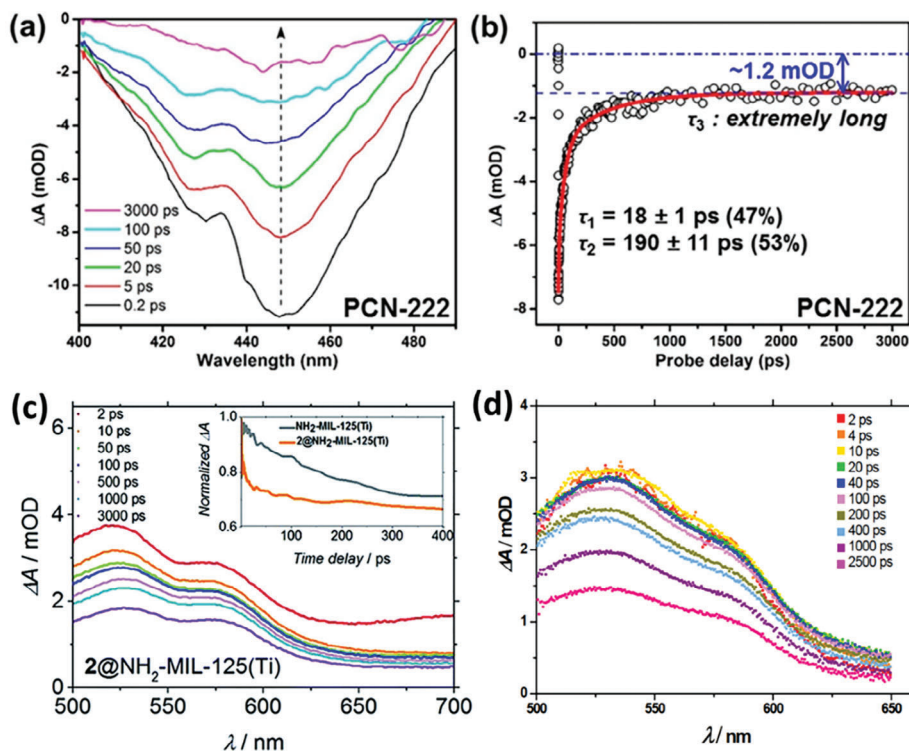
Figure 30. a) Transient TA spectra of PCN-222 collected at different probe delays (pump at 500 nm). b) Representative TA kinetics of PCN-222 captured at the probing wavelength of 430 nm. In (a) and (b), the TA signal is provided as absorbance variation (ΔA) with unit of mOD (OD is optical density). Reproduced with permission.[352] Copyright 2015, American Chemical Society. c) Differential transient spectra of 2@NH2-MIL-125(Ti) in DMF upon excitation at 400 nm, inset: comparison of the time traces of NH2-MIL-125(Ti) and 2 occluded in NH2-MIL-125(Ti) at 540 nm in DMF. d) Differential transient absorption spectra for a suspension of NH2-MIL-125(Ti) in DMF upon excitation at 400 nm. Reproduced with permission.[353] Copyright 2017, The Royal Society of Chemistry.

MIL-53(Fe)/dehydrated.[354] In the measurement process, the samples should be dispersed and sonicated. The photo response of MIL-53(Fe)/hydrated sample depicts higher photocurrent than MIL-53(Fe)/dehydrated sample indicating more efficient charge separation of photoexcited electron–hole pairs (**Figure 31**a).[354] Su et al.[355] studied and compared the photocurrent behavior of MOF-derived hollow CuO/ZnO nanocages (h-CZN), hollow ZnO nanocages (h-ZN), and CuO (Figure 31b). TPR results demonstrate the higher photocurrent density and separation efficiency

of photogenerated carriers of h-CZN than that of CuO and h-ZN.[356] Hence, the h-CZN provides the highest photocatalytic performance.[355]

3.2.8. Electrochemical Impedance Spectroscopy

Electrochemical impedance spectroscopy (EIS) probes material charge transfer and electrode reactions effectively. Porosity plays a crucial role in EIS outcomes, potentially aiding pore size
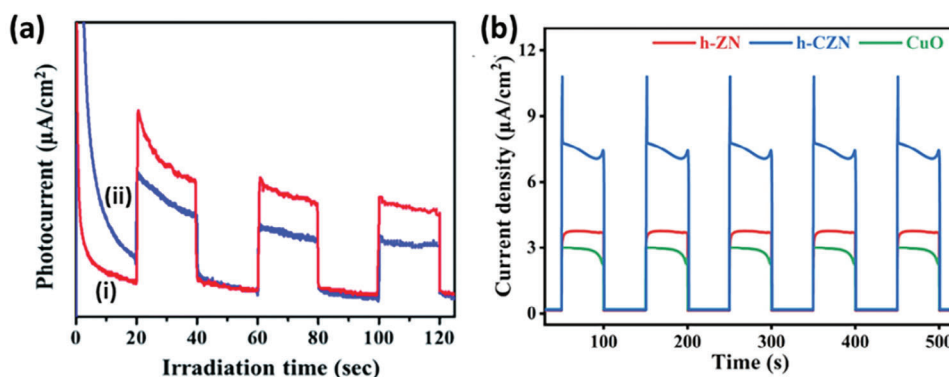
Figure 31. a) TPS results of i) MIL-53(Fe)/hydrated and ii) dehydrated samples, Reproduced with permission.[354] Copyright 2019, The Royal Society of Chemistry., b) TPR, (spectra of h-ZN, h-CZN, and CuO. Reproduced with permission.[355] Copyright 2022, Elsevier.

ADVANCED
SCIENCE NEWS
www.advancedsciencenews.com

NANO · MICRO
small
www.small-journal.com
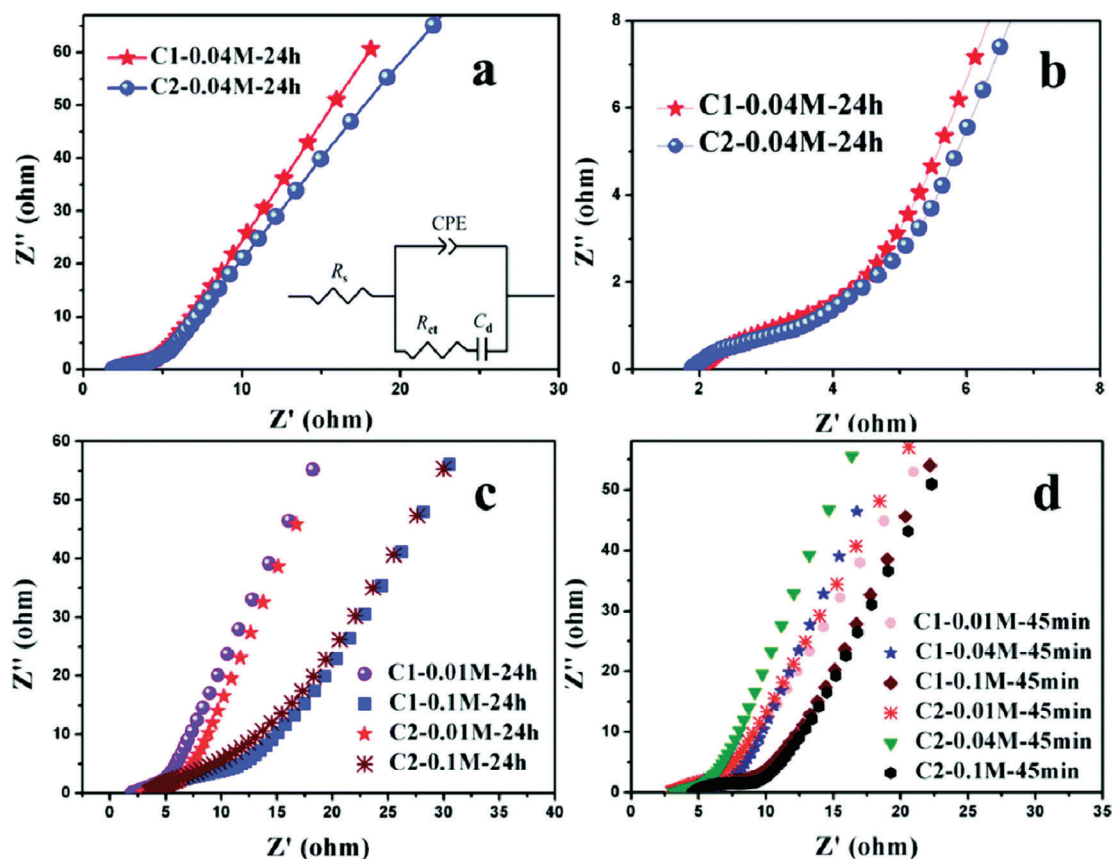
Figure 32. Electrochemical impedance spectra. a) Nyquist plots of the as-prepared C1-0.04 M-24 h and C2-0.04 M-24 h hybrid electrodes at room temperature; inset shows an equivalent circuit. b) A magnification image of EIS data. c,d) Nyquist plots of other hybrid electrodes. Reproduced with permission.[359] Copyright 2019, The Royal Society of Chemistry.

assessment.[357] EIS employs a three-electrode setup with a potentiostat, applying a periodic signal and collecting the response. Impedance spectra are plotted in electrochemical cells, focusing on the linear response. Data are presented in Nyquist or Bode plots, using components like R, C, and L. Software can analyze EIS data with circuits, and it helps determine exciton lifetimes.[358]

Indeed, EIS is employed to study the electrical conductivity, charge transfer mechanisms, and surface/interface properties of both MOFs and MOF derivatives. However, the application of EIS in the context of MOF derivatives can differ due to specific properties and introduced modifications. These distinctions encompass alteration-induced effects, redox behavior, electrocatalysis, stability, and ion diffusion characteristics.

To evaluate the electrical resistance as well as charge transfer resistance of MOF-derived MnO_x/N-doped carbon/MnO_2 with moderate carbon/nitrogen ratios (6.76 and 1.84 for C1- and C2-based composites, respectively) EIS measurements have been performed at an open circuit voltage in the frequency range of 100 kHz to 10 MHz (**Figure 32**). The conductivity data of the solid samples were obtained with four-point probes. Generally, similar patterns are observed in the Nyquist plots of C1 and C2 electrodes which exhibit dominancy of kinetic control in the high-frequency region and diffusion control in the low-frequency

region.[359] From EIS results, it is revealed that long-period soaking and lower concentrations are major conditions in the synthesis of composite electrodes.[359]

3.2.9. Dynamic Light Scattering (DLS)

DLS determines the hydrodynamic size of MOFs in solution. It also offers size distribution insights for particles within MOF and MOF-derivative samples. This method reveals the range of particle sizes in the solution, crucial for assessing material homogeneity or heterogeneity. For MOF derivatives, with surface modifications and functional groups, DLS aids in understanding their impact on particle size distribution and colloidal behavior. It provides insights into the effectiveness of surface modifications in controlling particle size and stabilizing colloidal systems. DLS operates by monitoring intensity fluctuations resulting from scattered laser light interference caused by moving particles. An autocorrelation function of the intensity over time is plotted, and a fitting model is applied to extract the particle's diffusion coefficient. It is crucial to note that the accuracy of the hydrodynamic diameter depends on the chosen fitting model.[360] The DLS analysis of the $MnFe_2O_4$/C particles and $MnFe_2O_4$/C@Ce_6 is given in **Figure 33**. As can be seen, the results show a narrow peak

**ADVANCED
SCIENCE NEWS**
www.advancedsciencenews.com

**NANO · MICRO
small**
www.small-journal.com
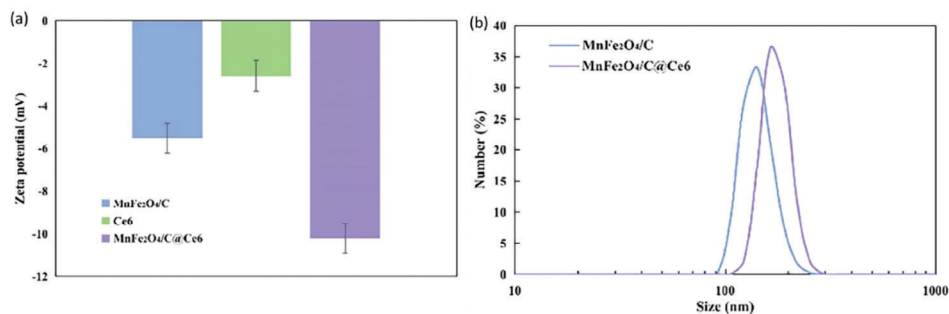
Figure 33. a) DLS analysis of the $MnFe_2O_4/C$ particles and $MnFe_2O_4/C@Ce_6$. b) zeta potential of $MnFe_2O_4/C$, free Ce_6, and $MnFe_2O_4/C@Ce_6$. Reproduced with permission.[361] Copyright 2021, Elsevier.

that suggests both particles are homogeneously dispersed.[361] The measured diameter for $MnFe_2O_4/C$ is 130 nm, while for $MnFe_2O_4/C@Ce_6$ is 150 nm. The results exhibited an increase in the hydrodynamic diameter of MOF-derived particles due to the loading of Ce_6.

3.2.10. Electrophoretic Light Scattering (ELS)

Electrophoretic Light Scattering (ELS) is used to analyze particle drift for Zeta potential. For MOFs and MOF derivatives, knowing the zeta potential is important for understanding their colloidal behavior, dispersion stability, and interaction with other species in solution. It provides insights into the surface chemistry, surface modification effects, and stability of the particles. The principle of ELS is based on dynamic light scattering.[] The dispersed particle mobility determines the frequency or phase shift of an incident laser beam. While in DLS Brownian motion causes particle motion, in ELS, the oscillating electric field is responsible for motion. In addition to the DLS analysis, the ELS analysis of the $MnFe_2O_4/C$ particles and $MnFe_2O_4/C@Ce_6$ is given in Figure 33. The zeta potentials of $MnFe_2O_4/C$, free Ce_6, and $MnFe_2O_4/C@Ce_6$ are -5.5 ± 0.7, -2.5 ± 0.7, and -10.2 ± 0.5 mV, respectively. It is clear that the zeta potential of the $MnFe_2O_4/C$-derived Ce_6 is enhanced.

3.2.11. Fluorescence Correlation Spectroscopy (FCS)

Fluorescence correlation spectroscopy (FCS) is a type of fluorescence-based technique utilized for the determination of the diffusion coefficient, local concentration, and hydrodynamic diameter of labeled nanoparticles.[362,363] The principle mechanism of FCS is based on analyzing the time correlation in fluorescence fluctuation emitted when fluorescently labeled nanoparticle in a liquid sample are diffusing in and out of an observation volume.[364] The diffusion coefficient and concentration of fluorescent particles are the outcomes of FCS data analysis. The measured diffusion coefficient alongside Stokes–Einstein relation is used to calculate the hydrodynamic diameter of a nanoparticle.
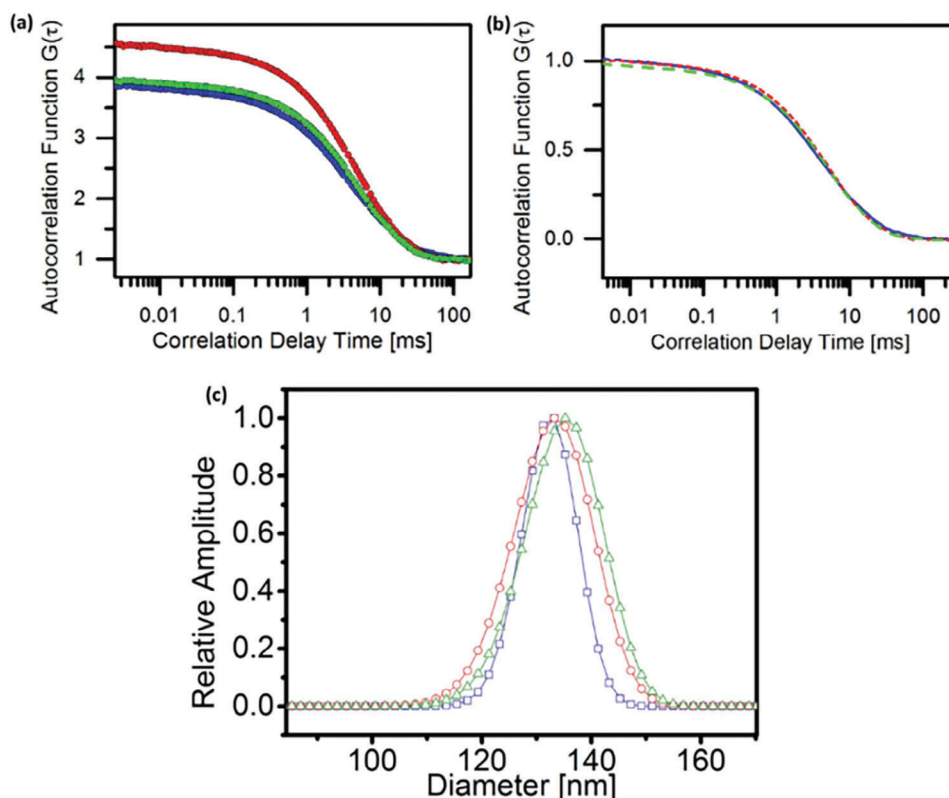
In the case of MOFs and MOF derivatives, FCS can provide information about the mobility of guest molecules or functionalized moieties within the MOF framework. This is valuable for understanding the dynamics of guest molecule release, diffusion behavior, or interactions with the MOF matrix. Furthermore,

FCS can provide insights into the behavior of guest molecules within the MOF and its derivative frameworks, such as diffusion rates, residence times, or binding interactions. By using fluorescently labeled guest molecules, FCS allows the characterization of their release kinetics, diffusion behavior, or interactions with the MOF structure. To measure the hydrodynamic diameter of Zr-fum MOF NPs, FCS is used (**Figure 34**).[236] The results in an apparent diffusion time of 3.68 ms, give a hydrodynamic diameter of Zr-fumNPs, 135 nm.

3.2.12. Aqueous Stability Testing

Aqueous stability tests have been performed to evaluate the chemical stability of MOFs in water because of their application in water purification using photocatalytic reactions.[322] As MOFs and their derivatives are composed of metal nodes connected by organic ligands, they form a porous crystalline structure. Aqueous stability testing helps evaluate the chemical stability of MOFs in water or aqueous solutions. It is widely recognized that the degradation of MOFs typically involves two key factors: the breakage of metal-ligand bonds and the formation of more stable products compared to pristine MOFs.[339] Therefore, the chemical stability of MOFs is highly dependent on intrinsic structural characteristics (internal factors) such as the charge density of metal ions, connectivity of metal ions/clusters, ligand basicity, ligand configuration, and ligand hydrophobicity, among others. So, using aqueous stability testing the performance and suitability of metal–organic frameworks and MOF derivatives for applications in aqueous environments could be evaluated. It involves assessing the stability, durability, and structural integrity of these materials when exposed to water or aqueous solutions. The relevance and approach for conducting aqueous stability testing may vary for MOFs and MOF derivatives.

Most MOF structures contain acidic or basic functional groups, so to test their aqueous stability it is crucial to use enough water (i.e., 20 mg of MOF suspended in 10 mL of water) for each test.[313] Moreover, the pH of the water should be measured before MOF is added as well as after its filtration and removal. To test the MOF stability in water, the MOF needs to be suspended in an accurately measured pH solution for a certain amount of time (at least 12 h) at room temperature.[313] After exposure to an aqueous solution, the MOF should be recovered through filtration, washing, and then drying.[365] It is noted when making

ADVANCED
SCIENCE NEWS

www.advancedsciencenews.com

NANO · MICRO

small

www.small-journal.com

Figure 34. FCS Autocorrelation functions of labeled Zr-fum particles sample 1(blue), 2(red), and 3(green). a) Original correlation curves illustrate small different correlation heights demonstrating small different concentrations of the three nanoparticle samples. The same data after normalization b) illustrates a slight variation in the diffusion times of the Zr-fum samples expressing small batch-to-batch changes in the hydrodynamic diameter. c) FCS size distribution of three measured nanoparticle batches 1(blue), 2(red), and 3 (green) collected from GDM Fit. The similarities in the resulting diameters show the great reproducibility of the synthesis of the particles. Reproduced with permission.[236] Copyright 2016, The Royal Society of Chemistry.

pH solution, the chemical identities of counterions and buffers should be considered as these can interfere with experiments and lead to errors in the analysis of results. Finally, the yield stability is calculated by measuring the percentage mass of recovered MOF with respect to the initial mass which describes the percentage of MOF which is not dissolved in the solution.[313] Noted to have the stability of the MOF after exposure to the aqueous solution, the sample should be recovered via careful filtration and reactivated following the appropriate activation procedure.[313] As this comparison needs accurate control of porosity and structure, it is critical to verify the MOF identity using PXRD and N_2 isotherm measurements before and after aqueous stability testing.

As an example, for the case of MOF-545 and MMPF-6,[366,367] the stability experiments revealed exceptional performance, even when exposed to concentrated aqueous HCl solution for 24 hours. This exceptional stability can be attributed to the presence of robust Zr-O bonds within the 8-connected Zr-clusters and the effective chelation between Fe(III) and porphyrin, as observed in similar PCN-series MOFs previously reported.[338]

Interestingly, the utilization of monocarboxylic acids as solvents in the synthesis of stable Zr(IV)-based MOFs has been observed.[338] In the case of the large-pore MOF, MIP-200, based on Zr^{4+} and 3,3',5,5'-tetracarboxydiphenylmethane (H4mdip), dimethylformamide (DMF) commonly used in MOF synthesis was replaced by a mixture of monocarboxylic acid (formic acid)

and acetic anhydride. Remarkably, MIP-200 exhibited outstanding stability even under highly challenging conditions, including concentrated strong acids (HCl and HNO_3), highly concentrated H_3PO_4 and H_2SO_4, as well as exposure to NH_4OH vapor.[368]

3.2.13. NMR Spectroscopy

Nuclear magnetic resonance spectroscopy (NMR) is a potent method for characterizing materials and determining molecular structures at the atomic level.[369] It relies on the properties of electrically charged nuclei with multiple spins. These nuclei, when subjected to a magnetic field, resonate at specific frequencies, typically in the radio frequency range, detectable using radio techniques. Various NMR techniques, including the deuteron NMR (H NMR),[370] solid-state NMR (ss-NMR),[371] ^{13}C cross-polarization magic angle spinning NMR (^{13}C CP/MAS NMR),[372] proton high-resolution magic angle spinning NMR (HR-MAS NMR)[373] and recently proposed classic NMR by a combination of liquid- and solid-state in-situ crystallization NMR[374] have been employed. In the case of MOFs, NMR techniques are used to assess purity, link ratios, modulator remnants, and solvent absence post-activation. MOFs that can't dissolve in typical NMR solvents require digestion. This involves adding D_2SO_4, NaOD, or diluted HF in D_2O to MOF, sonicating the mixture, and finally
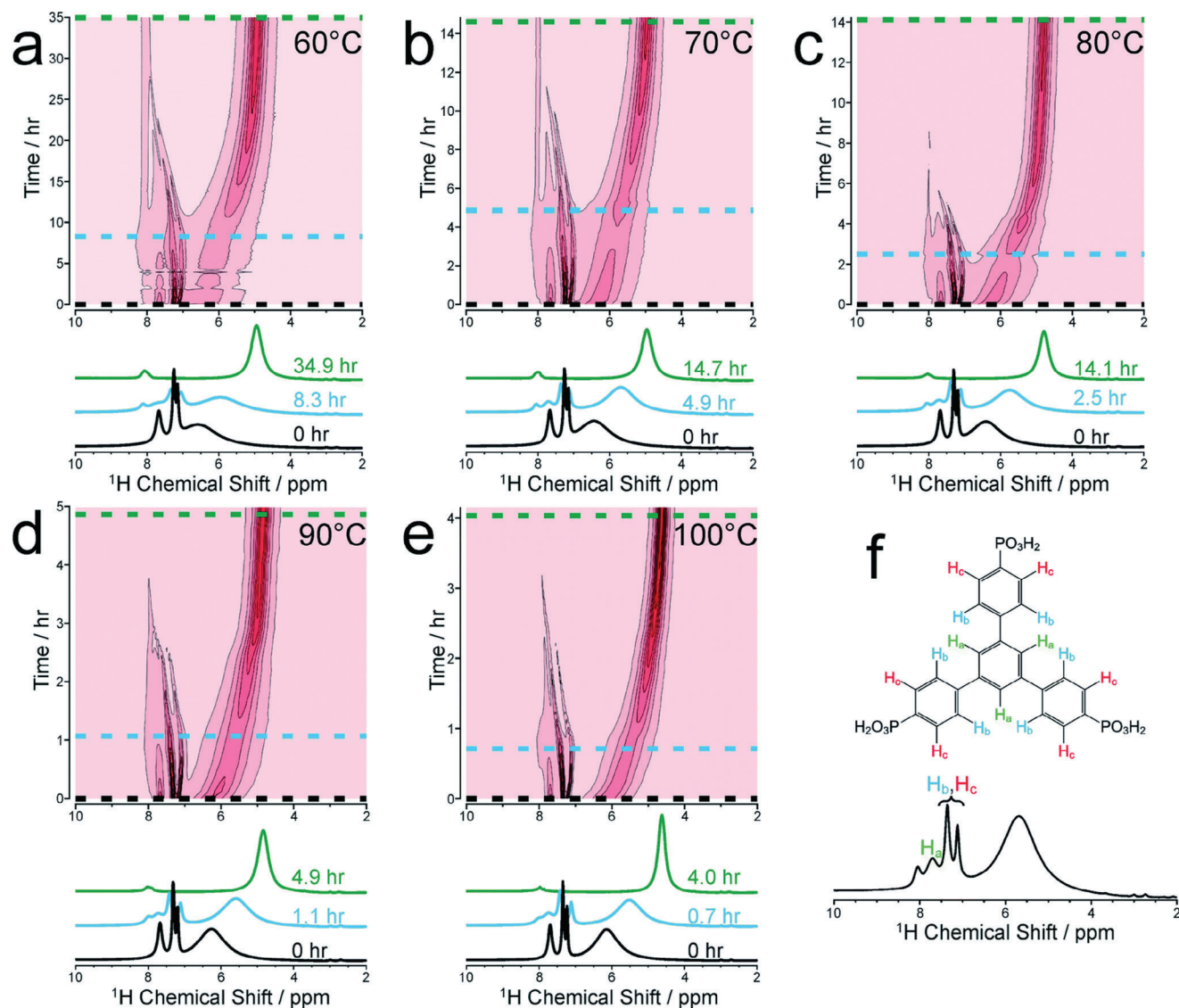
Figure 35. Intensity contour graphs of the ^1H NMR spectra captured as a function of time in the in situ NMR measurements of MFM-500(Ni) synthesis, and individual spectra selected at specific times (indicated by horizontal dashed lines in the contour plots), at different temperatures: a) 60 °C, b) 70 °C, c) 80 °C, d) 90 °C and l 100 °C. Assignments of the three peaks due to aromatic ^1H environments (denoted H_a, H_b, and H_c) in the BTPPA linker are illustrated in (f). The spectra are illustrated without normalization. Reproduced with permission.[376] Copyright 2021, The Royal Society of Chemistry.

diluting it with DMSO-d6.[313] Recently, ss-NMR has become increasingly useful for MOF characterization, offering insights into framework motion, guest diffusion, and host–guest interactions. For example, Xe NMR studies CO_2 diffusion within MOF-74-Mg pores[375] and identifies interactions in activated UMCM-1.[376] ss-NMR detects NMR-active nuclei in MOF frameworks, making it possible to detect metal ions in secondary building units (SBUs) containing such nuclei. However, due to the low natural abundance and small magnetic moments of these nuclei, specialized pulse sequences like CPMG are necessary to enhance signal strength. For quadrupolar nuclei, broad-band pulses or WURST sequences expand the excitation frequency range. Detecting paramagnetic ions like Cr, Mn, Co, Fe, Cu, or Ni remains a challenge. Recently, combined ss-NMR and liquid-state NMR (CLASSIC NMR) have been used to observe organic material

crystallization from solution. CLASSIC NMR enables simultaneous monitoring of time-dependent changes in liquid and solid phases, polymorphic identification, and molecular aggregation spectrometer[376] (**Figure 35**). In situ NMR provides insights into initial liquid-phase reactions and solid formation mechanisms. A comprehensive review by Rehman et al. discusses NMR applications in MOF structure and dynamics characterization.[377]

3.3. Characterization of Chemical Properties

To determine the elemental states and composition of MOFs and their derivatives, spectroscopy techniques including Raman, FTIR, EDS, DRIFTS, and ICP-OES as the most common approaches have been used. In this section, we briefly review the

ADVANCED
SCIENCE NEWS

www.advancedsciencenews.com

NANO · MICRO
small

www.small-journal.com

Table 12. Summary of spectroscopy techniques used to study MOF and its derivatives.

Technique	Raman Spectroscopy	FTIR	EDS	DRIFTS	ICP-OES
Application	– Structural characterization. – Phase identification. – Study guest-host interactions. – Explore molecular vibrations, crystal symmetry, and coordination environments.	– Identify functional groups. – Verify MOF synthesis. – Characterize surface modifications. – Study adsorption processes in MOFs	– Elemental analysis. – Identifying metal ions, ligands, and impurities. – Determining elemental distribution within the structure.	– Provides information on surface species and adsorbates. – Allows in situ analysis. – Useful for studying catalytic reactions.	– Quantitative elemental analysis. – Determining metal ion concentrations. – Assessing the metal leaching behaviour.
Advantages	– Non-destructive. – Detailed information on molecular vibrations. – In situ and real-time analysis.	– Non-destructive. – Explore chemical bonding and functional groups. – Relatively easy sample preparation.	– Qualitative and semi-quantitative elemental information. – Relatively quick analysis. – Compatible with scanning electron microscopy (SEM).	– Surface sensitivity. – In-situ analysis. – Identification of adsorbates. – Quantitative analysis. – Characterization of guest-host interactions.	– High sensitivity. Wide dynamic range. – Multi-element analysis capability. – Suitable for analysing trace elements.
Disadvantages	– Fluorescence interference. – Limited depth penetration. – Sample handling and preparation.	– Limited spatial resolution. – Affected by water vapor interference. -Requires proper baseline correction.	– Limited sensitivity for low atomic number elements. – Potential for X-ray overlap. – May require specialized sample preparation.	– Limited spatial resolution. – Can be influenced by sample morphology and particle size. – Requires careful control of sample temperature	– Destructive technique. – Requires sample digestion. – Complex instrumentation. – Skilled operation. – Time-consuming sample preparation
Limitations	– Limited sensitivity for low-concentration species. – Require data interpretation expertise for complex spectra.	– Sensitive to surface species. – May not provide detailed structural information.	– Spatial resolution. -Cannot distinguish between different oxidation states of elements.	– Surface-sensitive technique. – May not fully represent the bulk properties of MOFs.	– Spatial resolution. -Cannot provide information on the distribution of elements within MOFs.

underlying mechanism of these methods and their application for MOF materials. **Table 12** summarizes the application, pros, and cons of these techniques applied for MOF and its derivatives.

3.3.1. Vibrational Spectroscopy (Infrared (IR)/Fourier-Transform Infrared (FTIR)/Raman spectroscopy)

Molecules exhibit a defined number of vibrational modes depending on their degrees of freedom. Linear molecules possess 3N-5 normal modes of vibration, while nonlinear molecules have 3N-6 modes, where N represents the molecule's atom count.[317] These modes fall into two categories: stretching and bending (**Figure 36**).

Stretching vibrations involve changes in bond lengths, while bending vibrations alter bond angles. Each vibrational mode absorbs energy at a distinct frequency, forming the basis for vibrational spectroscopy. This field comprises two primary techniques: infrared and Raman spectroscopy, each sensitive to specific vibrations and widely used for extracting structural and reactivity information from surface species in MOFs.[334,378]

In MOF research, infrared spectroscopy is more commonly used. The infrared spectrum spans three sub-regions: near-infrared (14 000–4000 cm^{-1}), mid-infrared (4000-400 cm^{-1}), and low-energy-far-infrared (400–10 cm^{-1}). Obtaining high-quality far-IR spectra is challenging, but high-brilliance synchrotron sources can enhance signal intensity. High-resolution synchrotron vibrational spectroscopy is particularly valuable for understanding phenomena like shear-induced phase transitions, structural flexibility, and pore-breathing mechanisms in MOFs.[379,380]

Three prominent IR techniques are FTIR, DRIFTS, and attenuated total reflection (ATR).[381] FTIR and DRIFTS are commonly used for observing solid-state materials and studying host-guest interactions. ATR, based on total reflection in a high refractive index crystal in direct contact with the material, is less preferred for MOFs. FTIR offers precise quantification and sensitivity to various chemical groups, employing a Fourier transform to translate raw data into the spectrum wavelength.[382] Unlike IR, which uses monochromatic light, FTIR irradiates the specimen with a light beam containing multiple frequencies in the vibrational IR region, resulting in higher signal-to-noise ratios.

Raman spectroscopy complements FTIR by detecting apolar bond vibrations. It analyses vibrational, rotational, and low-frequency modes based on inelastic scattering between a

ADVANCED
SCIENCE NEWS
www.advancedsciencenews.com

NANO · MICRO
small
www.small-journal.com

Stretching vibrations

Symmetric stretch

Asymmetric stretch

Bending vibrations

Rocking
In-plane bending

Scissoring
In-plane bending

Wagging
out-of-plane bending

Twisting
out-of-plane bending
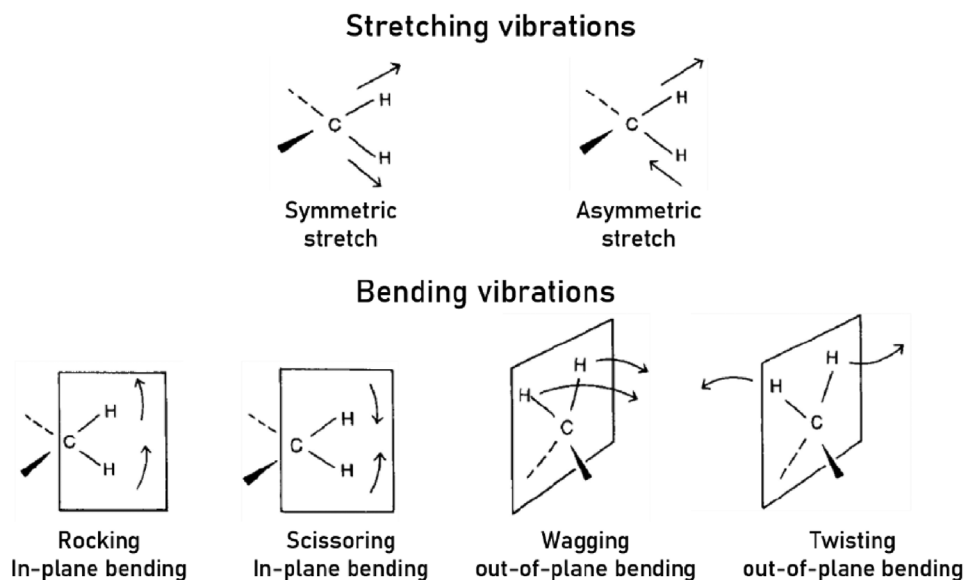
Figure 36. Representation of different type of stretching and bending vibrations. Reproduced with permission.[317] Copyright 2020, U. PORTO.

monochromatic laser beam and molecules in the specimen. Raman scattering arises when the frequency of scattered light differs from the incident light.[383]

Both IR and Raman techniques are extremely useful to address a series of properties typical for MOF materials including the absence/presence of solvents inside the pores, assessing the insertion of functional groups after the post-synthetic process, elucidating the nature and identity of linkers and evaluating the presence of defects in framework and coordination vacancies formed at the metal sites after desolvation. Vibrational frequency perturbation, change of band intensity, skeletal, and surface vibrational perturbation are the indexes that can be used to observe the interaction of probe molecules with the adsorption sites in MOFs which are crucial to understanding the role of MOF active sites.[334]

For example, FTIR and Raman spectroscopy are used to characterize the functional groups present in the MWCNTs, the MOFs/MWCNTs, and the Co@NSC/MWCNTs.[384] As shown in

Figure 37, there is a good similarity between the FTIR spectra of MWCNTs and MOFs/MWCNTs. For the Co@NSC/MWCNTs, in FTIR spectra the observed band in the 1616–1342 cm^{-1} region is associated with the vibrations of C=C and C=N bonds, which validates the successful doping of nitrogen.[385] The peak at 1415–1440 cm^{-1} is related to the C–S bond that confirms the organic skeleton of MOFs is composed and converted to N,S-Co doped graphite carbon layers on the surface of MWCNTs.[384] In addition, the observed weak absorption band at 856 cm^{-1} attributed to the Co–N bond[386] proves the presence of interaction between Co and N species.

Another example of using FTIR and Raman spectroscopy to study the Fe-MOF, Co-MOF, and Co-MOF@Fe-MOF is given in Figure 38.[387] For all materials, there is a peak at 1572 cm^{-1} which is attributed to asymmetric stretching vibrations of carboxylate groups.[388] The symmetric vibrations of carboxylic groups cause bands at 1354 cm^{-1} which is evidence of the presence of benzenedi-carboxylate anion (BDC^{2-}).[389,390] The peak
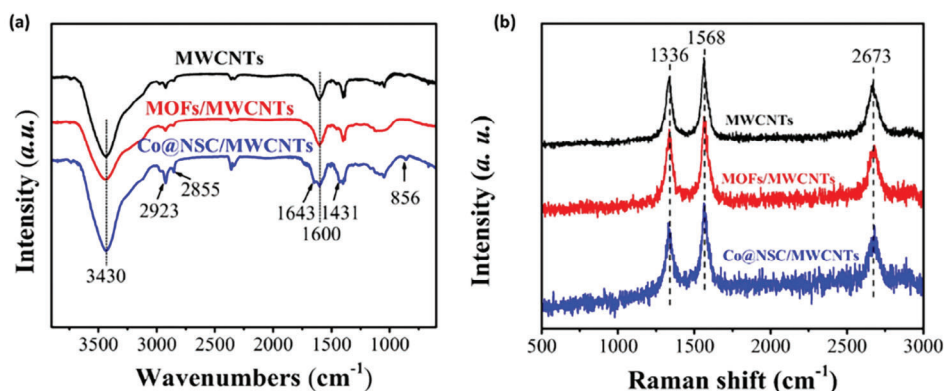
Figure 37. FTIR spectra and Raman spectra of the MWCNTs, the MOFs/MWCNTs, and the Co@NSC/MWCNTs. Reproduced with permission.[384] Copyright 2019, Springer Nature.

**ADVANCED
SCIENCE NEWS**

www.advancedsciencenews.com

NANO · MICRO

small

www.small-journal.com
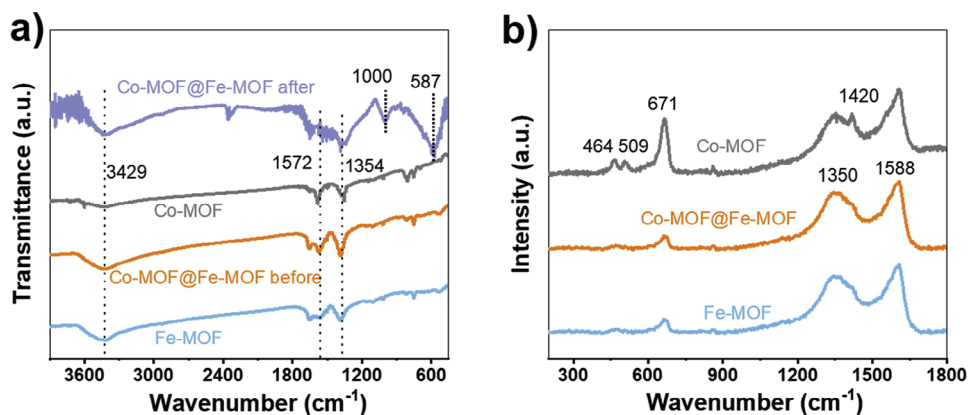
Figure 38. a) IR and b) Raman spectra for Fe-MOF, Co-MOF, and Co-MOF@Fe-MOF. IR spectrum of the catalyst after OER operation was also shown for comparison. Reproduced with permission.[387] Copyright 2020, Elsevier.

at 3429 cm^{-1} corresponds to the stretching vibration of OH.[388] The peaks in the range of 740–810 cm^{-1} are associated with IR bands for the benzene ring.[387] The Raman spectroscopy shows the presence of separate D (1350 cm^{-1}) and G (1588 cm^{-1}) bands as a consequence of involved graphene oxide.[391] For all MOFs, the ratios of I_D/I_G which are calculated from the peak intensity are between 1.04 and 1.06 that means there is a similar state of graphene oxide in the studied MOFs. The presence of M–O species causes the bands at 509, 671, and 1420 cm^{-1}.[388]

3.3.2. Diffuse Reflectance Infrared Fourier Transform Spectroscopy (DRIFTS)

DRIFTS, or Diffuse Reflectance Infrared Fourier Transform Spectroscopy, is a spectroscopy method commonly employed in MOF studies. It offers the advantage of analyzing powdered samples with minimal or sometimes no sample preparation. DRIFTS is based on a reflectance phenomenon and involves measuring the diffuse reflected infrared rays from a specimen, providing information about its shape and reflectivity. In DRIFTS, the reflection of infrared radiation occurs in all directions. An ellipsoid mirror is used to collect the infrared rays, which are then processed and analysed. This technique is valuable in MOF research for detecting the presence or absence of IR active functional groups.[392,393] Additionally, DRIFTS enables the study of MOF behaviour under different temperatures or in the presence of specific gases like CO and CO$_2$.[394]

For example, to understand how CO$_2$ adsorbed on the basic sites of MOF-808a, the DRIFTS test has been performed (**Figure 39**).[344] Although there is a probability of interference between IR spectra of the carboxylate group of the BTC ligand in MOF-808a with IR observation of CO$_2$ adsorption on MOF-808, in comparison with blank MOF-808a, several new bands can be observed. Increasing the temperature leads to the disappearance of these bands which means MOF-808a has absorbed CO$_2$ and generated new species.[344]

It is worth to mention DRIFTS can be performed on either powdered samples of an MOF, or the samples can be diluted in a matrix such as potassium bromide (KBr).[313]

To study the possible reaction pathway for the methanol steam reforming (MSR) reaction of MOF-derived composite as a precursor for CuO–CeO$_2$ catalyst, in situ DRIFT has been performed[395] (**Figure 40**). The obtained data show the spillover of oxygen species can be facilitated by the high dispersion of active metal. Consequently, the formate is oxidized to carbonate and generates CO$_2$. This enhances the selectivity of CO$_2$ by preventing the direct decomposition of formate to CO. Furthermore, it is explored that CuO-CeO$_2$ has lower selectivity and higher activity than CuO-CeO$_2$-I in the entire range of temperatures.[395]

3.3.3. Inductively Coupled Plasma Optical Emission Spectroscopy (ICP-OES)

Inductively Coupled Plasma Optical Emission Spectroscopy (ICP-OES) is an analytical method utilized for the determination of the number of specific elements in a sample. Due to the
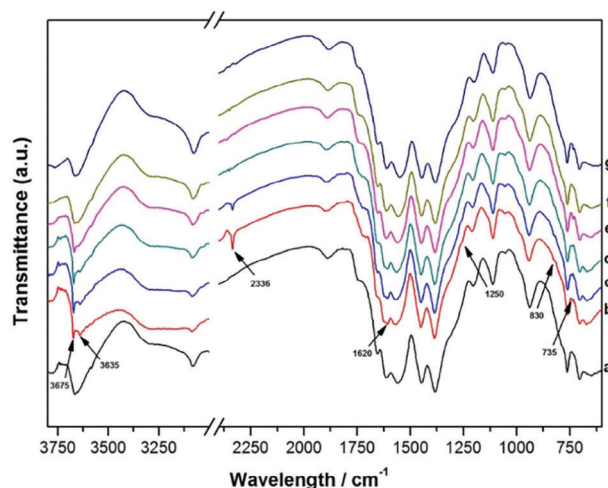
Figure 39. DRIFTS spectra of MOF-808a (a) and the samples after CO$_2$ introduced to MOF-808a and then heated at various temperatures: 30 °C (b); 70 °C (c); 110 °C (d); 170 °C (e); 220 °C (f); 300 °C (g). Each spectrum was taken 10 min after the desired temperature was reached. Reproduced with permission.[344] Copyright 2018, American Chemical Society.

**ADVANCED
SCIENCE NEWS**

www.advancedsciencenews.com

NANO · MICRO

small

www.small-journal.com
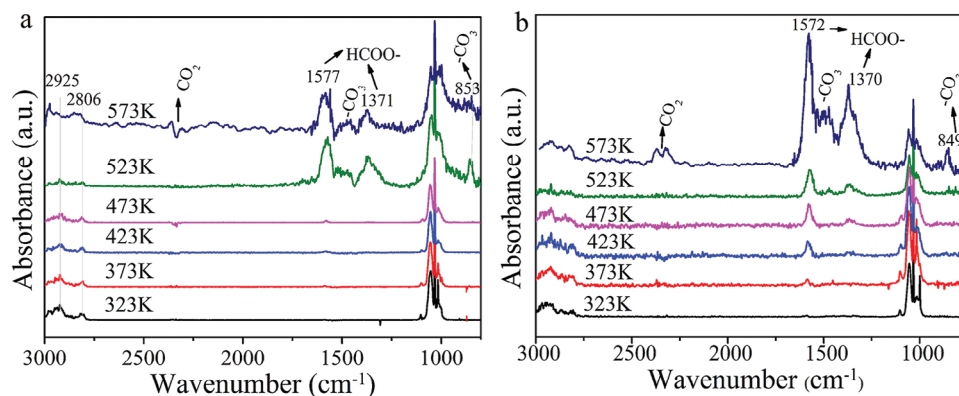
Figure 40. DRIFT spectra for MSR on reduced a) CuO-CeO$_2$ and b) CuO-CeO$_2$-I. Reproduced with permission.[395] Copyright 2021, Elsevier.

advantage of ICP-OES in the detection of elements at very low concentrations, ICP-OES is commonly used to determine the elemental composition of MOFs and their derivatives. It provides a quantitative analysis of metal ions present in the MOF structure, allowing researchers to assess the metal-to-ligand ratios and verify the synthesis process. Moreover, ICP-OES is capable of detecting and quantifying trace impurities in MOFs. It helps in assessing the purity of MOF and its derivative samples and identifying any unwanted contaminants that might affect the material's performance or properties. Prior ICP-OES analysis, the sample must be completely dissolved. For complete dissolution of MOFs, H$_2$SO$_4$ or HNO$_3$ should be added to MOFs followed by hydrogen peroxide in a microwave tube. Then, the sample is heated by microwave irradiation and finally cleaned before dilution with water.[313] Xue et al.[396] employed ICP-OES to determine the element contents of FeNC, CoNP@NC and CoNP@FeNC-0.05 catalysts (**Table 13**).

3.4. Characterization of Electronics Properties

The Recent development of MOFs with controlled electronic and optical properties enables the characterization of MOF electronic properties as a new fundamental science that paves the way for applications in electronics and photonics. To determine the Bandgap potential, band-edge, and bandgap offset as well as the Fermi level of MOF-based materials, XPS and UPS are the most commonly used techniques. Here, we survey the principle and the application of these techniques for MOF study.

3.4.1. X-Ray Photoelectron Spectroscopy (XPS)

X-ray photoelectron spectroscopy (XPS) is a quantitative method utilized to measure the elemental composition of the surface of a material as well as determine the binding states of the elements. By analyzing the binding energies of the photoelectrons emitted from the sample, the coordination chemistry, ligand-metal interactions, and the electronic structure of the MOF materials can be identified. Furthermore, it provides information about the nature and abundance of surface-bound ligands, linker species, and potential surface modifications.

For example, to determine the elemental chemical state in Co-MOF-derived catalysts under different temperatures, XPS has been performed (**Figure 41**). The overall XPS spectrum consists of characteristic peaks for C 1s, O 1s, and Co 2p (Figure 41a). By increasing the calcination temperature, the intensity of the C 1s peak is enhanced while the peak intensities of O 1s and Co 2p are reduced. **Table 14** lists the atomic concentrations and binding energies of C, Co, and O atoms, respectively.[397]

As another example, the XPS measurement is utilized to compare and analyze the chemical composition, involved electronic interactions, and oxidation states of Fe-MOF, Co-MOF, Co-MOF@Fe-MOF, and the hybrid MOF catalyst.[387] The full XPS spectra of the Fe-MOF, Co-MOF, and Co-MOF@Fe-MOF are shown in **Figures 42** and **43** that demonstrate the presence of Fe, Co, O, and C elements in the MOFs.

The results of the XPS spectrum of Fe 2p in Fe-MOF and Co-MOF@Fe-MOF demonstrate the bands at binding energies of 712.0 eV and 725.3 eV are attributed to Fe 2p$_{3/2}$ and Fe 2p$_{1/2}$[398] which illustrates the Fe in mentioned MOFs are Fe(III) oxidation state. The formation of hybrid MOF enhances the shake-up band due to the more paramagnetic state of Fe ions. The Co 2p XPS spectra indicate cobalt species is mainly in its +2 oxidation state.[399] Furthermore, the generation of Fe-MOF on the surface of Co-MOF leads to strong electronic interactions between two MOFs. The results exhibit that in the considered MOFs, the carbon composition not only comes from the ligands but also from the graphene oxide additive.[387]

3.4.2. Ultraviolet Photo Electron Spectroscopy (UPS)

UPS is an alternative to XPS, which utilizes monochromatic UV light radiation to produce photoelectrons. In UPS the excitation source is helium discharge sources normally He-I, 21.2 eV and He-II, 40.8 eV.[400] As low-energy photons are used in UPS;

Table 13. The element contents of prepared catalysts from ICP-OES tests.

	FeNC	CoNP@NC	CoNP@FeNC-0.05
Fe (wt%)	1.05	–	1.04
Co (wt%)	–	1.82	4.02

ADVANCED
SCIENCE NEWS

www.advancedsciencenews.com

NANO · MICRO
small
www.small-journal.com
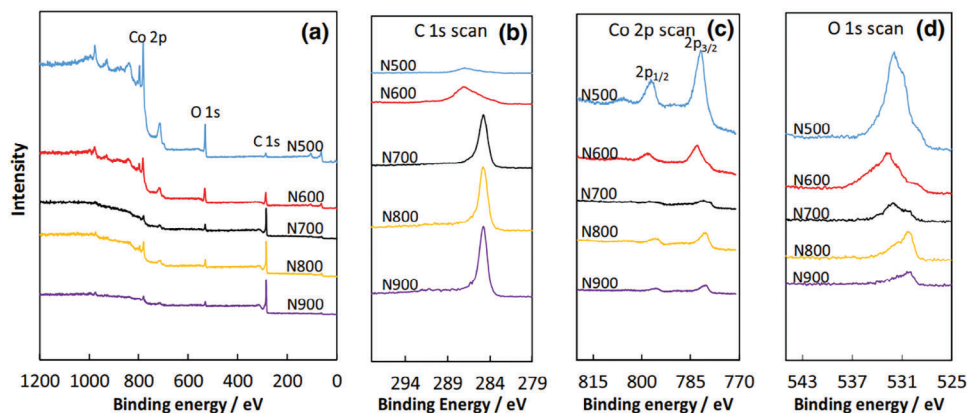
Figure 41. XPS spectra of Co-MOF-derived catalysts a survey spectrum, b C 1s scan, c Co 2p scan, and d O 1s scan. Reproduced with permission.[397] Copyright 2018, Springer Nature.

Table 14. Binding energy and percentage of atomic concentration by XPS, and relative ratio of D and G bands by Raman of Co-MOF-derived catalysts.[397]

Sample	Binding energy [eV]			Atomic content [%]			I_D/I_G
	C 1S	Co 2P$_{3/2}$	O 1S	C	Co	O	
Co-MOF.N500	286.85	781.79	531.77	16.01	34.10	49.89	2.50
Co-MOF.N600	286.92	782.83	532.70	63.95	10.27	25.78	2.42
Co-MOF.N700	284.77	780.57	532.01	89.22	2.60	8.18	1.63
Co-MOF.N800	284.77	780.39	530.28	86.58	4.47	8.96	1.33
Co-MOF.N900	284.79	780.42	530.28	93.71	1.84	4.45	1.08
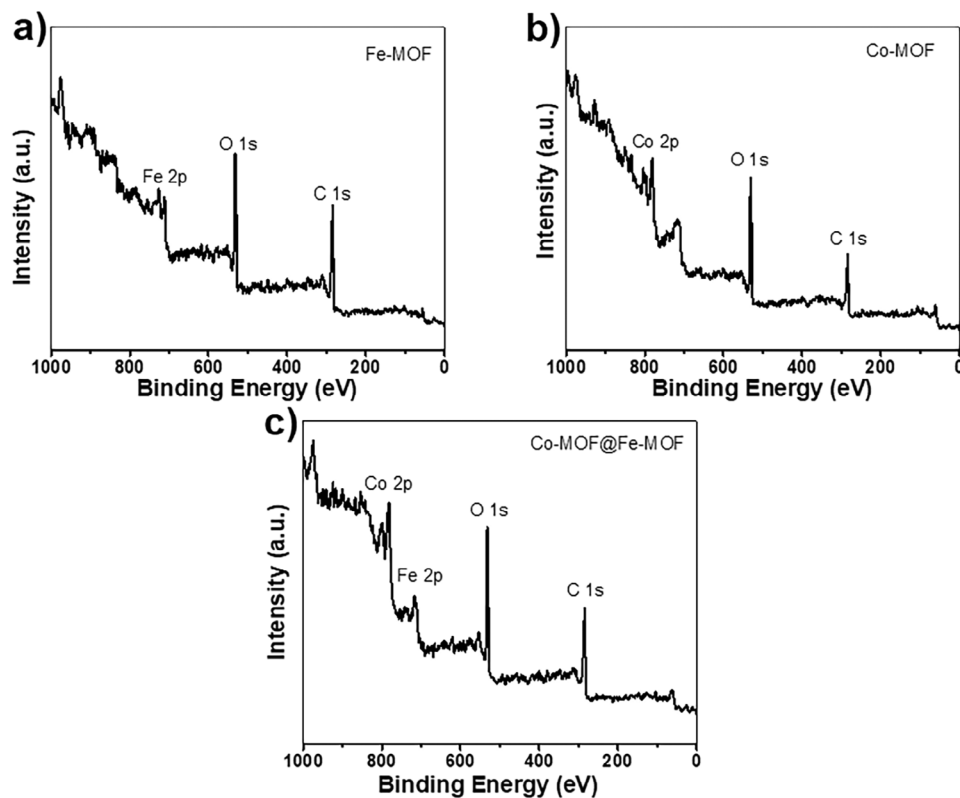
Figure 42. XPS full survey spectra of a) Fe-MOF, b) Co-MOF, c) Co-MOF@Fe-MOF products. Reproduced with permission.[387] Copyright 2020, Elsevier.

**ADVANCED
SCIENCE NEWS**

www.advancedsciencenews.com

NANO · MICRO

small

www.small-journal.com
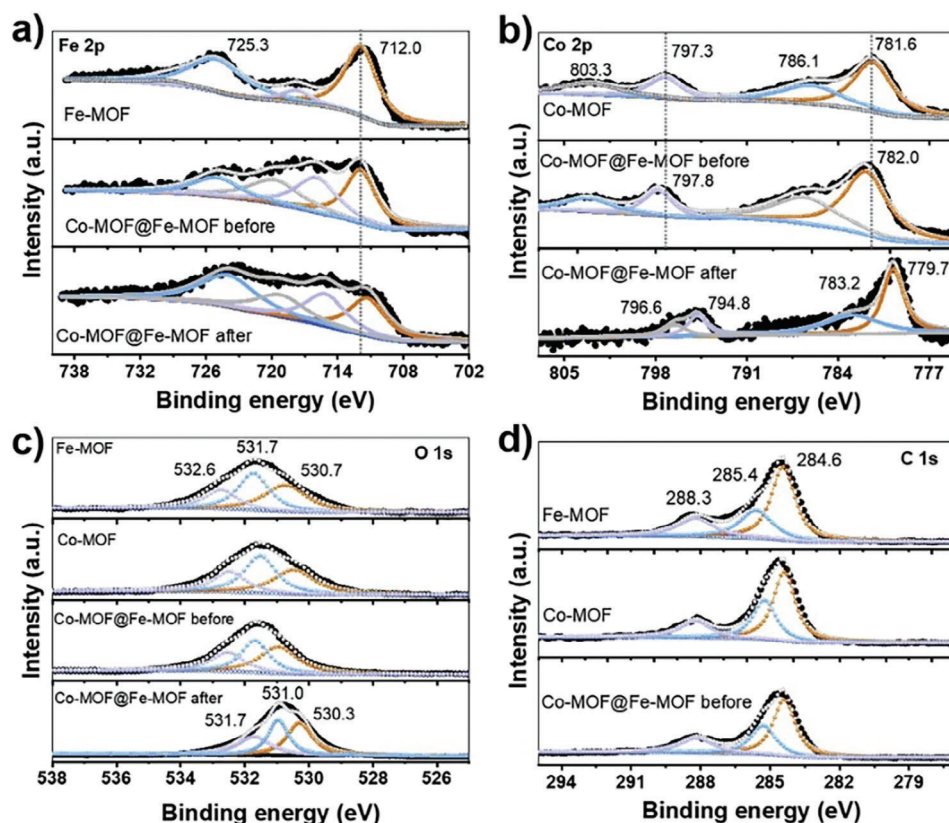
Figure 43. XPS spectra of Fe-MOF, Co-MOF, Co-MOF@Fe-MOF, and the hybrid MOF catalyst after OER operation. a) Fe2p, b) Co2p, c) O1s, and d) C1s. Reproduced with permission.[387] Copyright 2020, Elsevier.

it is suitable to analyze the valence band structures of MOF semiconductors. In UPS, the changes in the kinetic energy of the electron depend on its molecular orbital. The photon energy equals the sum of the absolute value of electron kinetic energy and its orbital potential energy.[235] To complement the UPS measurements, low-intensity XPS (LIXPS) can be used. In LIXPS, an X-ray gun uses very low photon density sufficient to carry out secondary edge measurement. Through this approach, it would be possible to detect the charging artifacts that usually occur in UPS measurements because UV sources have relatively high photon density which can be crucial in organic materials due to low conductivity that prevents effective replenishment of photo-extracted electrons.[401] Due to the fewer charging effects in LIXPS compared to UPS, in the measurement of work function by LIXPS, the charging artifacts that affect UPS are revealed.[402] Elzein et al.[401] study the growth of MOF thin films composed of TCPP (= Tetrakis(4-carboxyphenyl)porphyrin) linkers and dicopper paddlewheel secondary building blocks (SBU) self-assembled on top of SAM-terminated (MP) Au substrates by ultraviolet and X-ray photoemission spectroscopy (**Figure 44**). They carried out measurements for three cases: i) the Au-functionalized surface sample was incubated in $Cu(NO_3)_2$ and then immersed in TCPP. ii) the Au-functionalized sample was incubated in the mixed fresh TCPP and $Cu(NO_3)_2$ solutions. iii) Au-functionalized surface was immersed only in TCCP solution.

The UPS results exhibited the orbital line-up of the MOF molecules bound to the surface of the Au-functionalized surface

as a considerable barrier for both hole and electron injections from the Au-functionalized surface to the MOF thin film. This property at the interface is crucial to the design and development of conductive MOF materials which can be a breakthrough in molecular electronic devices.

4. Summary and Challenges

Considering the enormous demand for high-performance advanced materials with functional properties, the development of MOF derivatives is of great importance. Past and recent research has demonstrated the capability of synthesizing and characterizing MOF-derived materials with tuneable structures, morphologies, compositions, functionalities, and superior physiochemical properties by using MOF as a precursor and sacrificial template. MOF derivatives are attractive materials for various advanced technological applications e.g., energy, biomedical, sensor, etc. MOF derivatives are generally composed of multiple components assembled in different hierarchical levels and each component possesses special functionality and their synergistic effect helps to realize enhanced performance. In this review, we have summarized the details of synthesis techniques and mechanisms for developing MOF derivatives. Previous studies demonstrate that MOF can serve as a precursor for producing various MOF derivatives where MOF works as a sacrificial template and a controlled synthesis technique can preserve the structure, surface area, and porosity of the parent MOF to its derivative. This is

**ADVANCED
SCIENCE NEWS**

www.advancedsciencenews.com

**NANO · MICRO
small**

www.small-journal.com
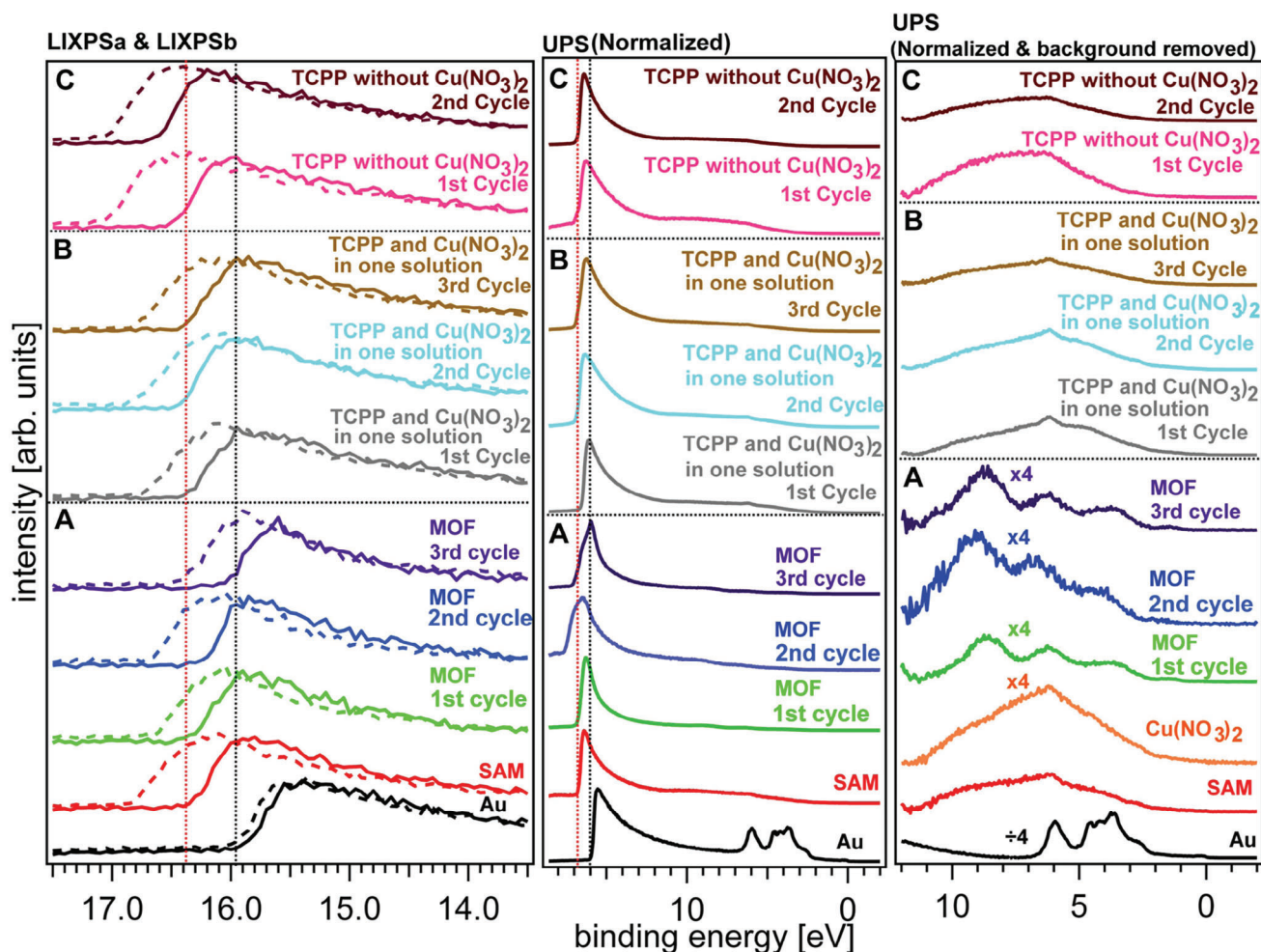
Figure 44. LIXPS and UP spectra before and after step-by-step incubation of sputter cleaned Au functionalized substrate in (A) in the metal ion $Cu(NO_3)_2$ then in the organic ligands TCPP for three cycles sequentially, B) in both the metal ion and the organic ligand solution for three cycles sequentially, and C) only in a TCPP solution for two cycles. Their normalized secondary edges were measured with LIXPS before (LIXPSa) and after (LIXPSb) UPS and are illustrated in the left panel. The complete normalized UP spectra are shown in the middle. The right panel illustrates the evolution of the valence band/HOMO emission features via the deposition process. Reproduced with permission.[401] Copyright 2016, American Chemical Society.

difficult to achieve through other conventional synthesis techniques. The tuneability in composition, structure, morphology, and physiochemical properties in the MOF derivatives can be achieved easily using the MOF precursor-based synthesis technique. This review also summarizes that through cogently designing the synthesis process or combining multiple synthesis techniques, variety of MOF derivatives with predetermined structures, properties, and functionalities can be developed for a variety of advanced technological applications.

Despite significant progress on the scalable and facile MOF-templated synthesis of porous functional MOF derivatives, there are still some challenges that remain. When the MOF precursors are treated at low temperatures, the derived material shows poor crystallinity and high resistivity which leads to poor performance. Alternatively, when treated at a higher temperature, there is a possibility of structural collapse in the derived materials resulting in poor structural, mechanical, and electrical properties. We are listing below some of the prominent challenges and potential forthcoming research directions in the synthesis of MOF-derived

materials which needs systematic study to overcome. i) Most reported studies indicate that synthetic parameters are crucial to controlling the composition, structure, morphologies, and properties of MOF-derived materials. So, a systematic investigation is important to understand the relationship between the structure and properties of MOF derivatives. The development of a robust and scalable synthesis process capable of controlling the features of the MOF derivatives is also crucial. ii) The decomposition and transformation mechanism of MOF to its derivatives are not yet clearly understood. ii) Significant control in preventing the degradation of the MOF structure during the conversion process through a calcination-based or solution-based synthesis process is yet to be achieved. iii) Managing the degree of particle aggregation during the transformation process of MOF to its derivatives is still a challenge and this kind of aggregation results from the formation of poor-quality MOF derivatives. iv) The possibility of low structural stability, difficulty in preserving the MOF precursor structure in the derivatives, and precise control over the surface area and pore size of MOF derivatives are major

**ADVANCED
SCIENCE NEWS**

www.advancedsciencenews.com

**NANO · MICRO
small**

www.small-journal.com

challenges yet to be achieved. v) Accurate control of the chemical composition and morphology of the MOF derivatives to control their physical and chemical properties is still a challenge to overcome. vii) Bringing this synthesis technique of MOF derivatives from laboratory to industrial scale production is also a major challenge to solve. For rapid development in the synthesis of MOF-derived materials and transfer of their performance to industrial-scale applications, a systematic study in terms of structure, composition, pore distribution, surface area, and pore volume during the transformation process is required. Additionally, a comprehensive understanding of the relationship between the structure of MOF-derived material and its physiochemical properties is required which needs the use and development of advanced characterization techniques and instruments. The basis of the characterization of MOFs can be classified into four main categories consisting of diffraction, microscopy, spectroscopy, and scattering. In addition, to characterize the physical, chemical, and electrochemical properties of MOFs and their derivatives including thermal stability, adsorption properties, porous structures, and aqueous stability, additional techniques such as thermogravimetric analysis (TGA), volumeter, and calorimeter have been used. To identify the components that compose of the MOF structures, detect the defects and impurities, and characterize the optical, electronic, chemical, and electrochemical properties of MOFs spectroscopy techniques have been widely used. Depending on the synthesis and preparation methods and characterizing desired properties, different spectroscopy methods including Raman, IR, FTIR, UV-Dis, XPS, and XAS are employed in MOFs study. To characterize MOFs' surface charge, determine the size distribution of the MOFs, obtaining information about their stability and surface interaction with other molecules scattering techniques have been employed. Through appropriate selection and integration of suitable scattering methods, these techniques can provide extensive information on MOF size, from angstrom to micrometer levels, as well as probe the internal structure of MOFs in highly concentrated samples. The increasing complexity of MOF structures needs advances in either crystallographic instrumentation or structural and functional analysis approaches. While enormous research has been dedicated to obtaining single crystals with appropriate diffraction quality, due to the challenges in the growth process of the MOF crystals such as gas temperature and induced reactions, using powder diffraction data through PXRD crystallography has been proposed as an alternative approach. Due to the compression of reciprocal 3D space into 1D space, which causes the overlap in diffracted peaks, analysis of PXRD data requires advances in structure computer modeling such as the charge flipping method that can pave the way to elucidate the crystal structures of complex MOFs derivatives. Microscopy techniques are promising candidates not only to image the surface of MOF structures but also to explore the structural and functional properties of MOFs. For example, in the structural analysis aspect, electron microscopy can be used as a complementary method to XRD/PXRD to unravel the complex crystal structure of MOF derivatives. Despite extensive applications of electron microscopy modalities in the imaging and characterizing of MOFs, there is a lack of fundamental understanding of the beam damage mechanism in MOFs and the interplay between numerous structural parameters and beam sensitivities. So, there is a need to have a systematic analysis of MOF beam sensitivities over MOF metal nodes, linkers, topologies, and guest molecules. Moreover, imaging and characterizing the solution and gas phase performance of MOFs needs using advanced EM methods which can open a new path for synthetic chemists. Considering the mentioned limitation in EM microscopy as well as their limited lateral resolution, due to its high spatial and lateral resolution as well as operation in ambient conditions, AFM is considered as the complementary instrument to image and characterize MOF structures. Recently several advanced AFM techniques are developed and are under development which can address the raising points for simultaneous imaging and characterizing the MOF structures and properties.

Finally, we can summarize by thanking the ongoing advance in characterization techniques and instruments, combining the experimental data obtained from measurements with computationally derived data can facilitate the structural-properties analysis of MOFs and their derivative and could provide promising results to enhance the synthesizing approaches.

Conflict of Interest

The authors declare no conflict of interest.

[1] H. Furukawa, K. E. Cordova, M. O'Keefe, O. M. Yaghi, *Science* **2013**, *341*, 1230444.
[2] O. M. Yaghi, M. O'Keeffe, N. W. Ockwig, H. K. Chae, M. Eddaoudi, J. Kim, *Nature* **2003**, *423*, 705.
[3] S. Kitagawa, R. Kitaura, S. Noro, *Angew. Chem., Int. Ed.* **2004**, *43*, 2334.
[4] C. R. Kim, T. Uemura, S. Kitagawa, *Chem. Soc. Rev.* **2016**, *45*, 3828.
[5] Z. Wang, S. M. Cohen, *Chem. Soc. Rev.* **2009**, *38*, 1315.
[6] H. Furukawa, N. Ko, Y. B. Go, N. Aratani, S. B. Choi, E. Choi, A. O. Yazaydin, R. Q. Snurr, M. O'Keeffe, J. Kim, O. M. Yaghi, *Science* **2010**, *329*, 424.
[7] B. F. Hoskins, R. Robson, *J. Am. Chem. Soc.* **1990**, *112*, 1546.
[8] G. B. Gardner, D. Venkataraman, J. S. Moore, S. Lee, *Nature* **1995**, *374*, 792.
[9] O. M. Yaghi, H. L. Li, *J. Am. Chem. Soc.* **1995**, *117*, 10401.
[10] S. Munakata, T. Kurodasowa, M. Maekawa, A. Hirota, S. Kitagawa, *Inorg. Chem.* **1995**, *34*, 2705.

ADVANCED
SCIENCE NEWS

www.advancedsciencenews.com

NANO · MICRO
small
www.small-journal.com

[11] D. Riou, O. Roubeau, G. Férey, *Microporous Mesoporous Mater.* **1998**, *23*, 23.

[12] Y. Li, R. T. Yang, *Langmuir* **2007**, *23*, 12937.

[13] P. Horcajada, T. Chalati, C. Serre, B. Gillet, C. Sebrie, T. Baati, J. F. Eubank, D. Heurtaux, P. Clayette, C. Kreuz, J. S. Chang, Y. K. Hwang, V. Marsaud, P. N. Bories, L. Cynober, S. Gil, G. Ferey, P. Couvreur, R. Gref, *Nat. Mater.* **2010**, *9*, 172.

[14] P. Falcaro, R. Ricco, C. M. Doherty, K. Liang, A. J. Hill, M. J. Styles, *Chem. Soc. Rev.* **2014**, *43*, 5513.

[15] H.-L. Jiang, B. Liu, T. Akita, M. Haruta, H. Sakurai, Q. Xu, *J. Am. Chem. Soc.* **2009**, *131*, 11302.

[16] S. Dang, Q.-L. Zhu, Q. Xu, *Nat. Rev. Mater.* **2018**, *3*, 17045.

[17] P. Silva, S. M. F. Vilela, J. P. C. Tome, F. A. Almeida Paz, *Chem. Soc. Rev.* **2015**, *44*, 6774.

[18] G. Huang, L. Yang, X. Ma, J. Jiang, S.-H. Yu, H.-L. Jiang, *Chem. – A Eur. J.* **2016**, *22*, 3470.

[19] X. Li, B. Zhang, Y. Fang, W. Sun, Z. Qi, Y. Pei, S. Qi, P. Yuan, X. Luan, T. W. Goh, W. Huang, *Chemistry* **2017**, *23*, 4266.

[20] T. Toyao, M. Fujiwaki, K. Miyahara, T.-H. Kim, Y. Horiuchi, M. Matsuoka, *ChemSusChem* **2015**, *8*, 3905.

[21] X. Kang, H. Liu, M. Hou, X. Sun, H. Han, T. Jiang, Z. Zhang, B. Han, *Angew. Chem., Int. Ed.* **2016**, *55*, 1080.

[22] Y. Xu, X.-J. Lv, Y. Chen, W.-F. Fu, *Catal. Commun.* **2017**, *101*, 31.

[23] F. Zhang, C. Chen, W.-M. Xiao, L. Xu, N. Zhang, *Catal. Commun.* **2012**, *26*, 25.

[24] S. Li, N. Wang, Y. Yue, G. Wang, Z. Zu, Y. Zhang, *Chem. Sci.* **2015**, *6*, 2495.

[25] H. Liu, S. Zhang, Y. Liu, Z. Yang, X. Feng, X. Lu, F. Huo, *Small* **2015**, *11*, 3130.

[26] S. Zhang, H. Liu, C. Sun, P. Liu, L. Li, Z. Yang, X. Feng, F. Huo, X. Lu, *J. Mater. Chem. A* **2015**, *3*, 5294.

[27] R. Zhang, L. Hu, S. Bao, R. Li, L. Gao, R. Li, Q. Chen, *J. Mater. Chem. A* **2016**, *4*, 8412.

[28] X. Wang, S. Zhao, Y. Zhang, Z. Wang, J. Feng, S. Song, H. Zhang, *Chem. Sci.* **2016**, *7*, 1109.

[29] C. Zhu, T. Dong, W. Gao, K. Ma, Y. Tian, X. Li, *Int. J. Hydrog. Energy* **2017**, *42*, 17457.

[30] G. Yu, J. Sun, F. Muhammad, P. Wang, G. Zhu, *RSC Adv.* **2014**, *4*, 38804.

[31] H. Tan, C. Ma, L. Gao, Q. Li, Y. Song, F. Xu, T. Wang, L. Wang, *Chem. – A Eur. J.* **2014**, *20*, 16377.

[32] Y.-Z. Chen, G. Cai, Y. Wang, Q. Xu, S.-H. Yua, H.-L. Jiang, *Green Chem.* **2016**, *18*, 1212.

[33] X. Wang, W. Chen, L. Zhang, T. Yao, W. Liu, Y. Lin, H. Ju, J. Dong, L. Zheng, W. Yan, X. Zheng, Z. Li, X. Wang, J. Yang, D. He, Y. Wang, Z. Deng, Y. Wu, Y. Li, *J. Am. Chem. Soc.* **2017**, *139*, 9419.

[34] S. Ding, C. Zhang, Y. Liu, H. Jiang, W. Xing, R. Chen, *J Ind Eng Chem* **2017**, *46*, 258.

[35] J. Long, Y. Zhou, Y. Li, *Chem. Commun.* **2015**, *51*, 2331.

[36] X. Liu, S. Cheng, J. Long, W. Zhang, X. Liu, D. Wei, *Mater. Chem. Front.* **2017**, *1*, 2005.

[37] R. V. Jagdeesh, M. Kathiravan, A. S. Alshammari, N. Helfried, P. Marga-Martina, R. Jörg, B. Matthias, R. V Jagadeesh, K. Murugesan, A. S. Alshammari, H. Neumann, M.-M. Pohl, J. Radnik, M. Beller, *Science* **2017**, *358*, 326.

[38] X. Li, C. Zeng, J. Jiang, L. Ai, *J. Mater. Chem. A* **2016**, *4*, 7476.

[39] J. Long, K. Shen, Y. Li, *ACS Catal.* **2017**, *7*, 275.

[40] B. Tang, W.-C. Song, E.-C. Yang, X.-J. Zhao, *RSC Adv.* **2017**, *7*, 1531.

[41] J. Long, K. Shen, L. Chen, Y. Li, *J. Mater. Chem. A* **2016**, *4*, 10254.

[42] W. Zhong, H. Liu, C. Bai, S. Liao, Y. Li, *ACS Catal.* **2015**, *5*, 1850.

[43] K. Shen, L. Chen, J. Long, W. Zhong, Y. Li, *ACS Catal.* **2015**, *5*, 5264.

[44] Y. Li, Y.-X. Zhou, X. Ma, H.-L. Jiang, *Chem. Commun.* **2016**, *52*, 4199.

[45] X. Ma, Y.-X. Zhou, H. Liu, Y. Li, H.-L. Jiang, *Chem. Commun.* **2016**, *52*, 7719.

[46] M. Ding, S. Chen, X.-Q. Liu, L.-B. Sun, J. Lu, H.-L. Jiang, *ChemSusChem* **2017**, *10*, 1898.

[47] X. Wang, W. Zhong, Y. Li, *Catal. Sci. Technol.* **2015**, *5*, 1014.

[48] V. P. Santos, T. A. Wezendonk, J. J. D. Jaén, A. I. Dugulan, M. A. Nasalevich, H.-U. Islam, A. Chojecki, S. Sartipi, X. Sun, A. A. Hakeem, A. C. J. Koeken, M. Ruitenbeek, T. Davidian, G. R. Meima, G. Sankar, F. Kapteijn, M. Makkee, J. Gascon, *Nat. Commun.* **2015**, *6*, 1.

[49] T. A. Wezendonk, V. P. Santos, M. A. Nasalevich, Q. S. E. Warringa, A. I. Dugulan, A. Chojecki, A. C. J. Koeken, M. Ruitenbeek, G. Meima, H.-U. Islam, G. Sankar, M. Makkee, F. Kapteijn, J. Gascon, *ACS Catal.* **2016**, *6*, 3236.

[50] B. An, K. Cheng, C. Wang, Y. Wang, W. Lin, *ACS Catal.* **2016**, *6*, 3610.

[51] B. Qiu, C. Yang, W. Guo, Y. Xu, Z. Liang, D. Ma, R. Zou, *J. Mater. Chem. A* **2017**, *5*, 8081.

[52] M. Oschatz, S. Krause, N. A. Krans, C. Hernández Mejía, S. Kaskel, K. P. de Jong, *Chem. Commun.* **2017**, *53*, 10204.

[53] Y.-X. Zhou, Y.-Z. Chen, L. Cao, J. Lu, H.-L. Jiang, *Chem. Commun.* **2015**, *51*, 8292.

[54] J. Zhang, B. An, Y. Hong, Y. Meng, X. Hu, C. Wang, J. Lin, W. Lin, Y. Wang, *Mater. Chem. Front.* **2017**, *1*, 2405.

[55] C. Bai, X. Yao, Y. Li, *ACS Catal.* **2015**, *5*, 884.

[56] X. Yao, C. Bai, J. Chen, Y. Li, *RSC Adv.* **2016**, *6*, 26921.

[57] R. Fang, R. Luque, Y. Li, *Green Chem.* **2016**, *18*, 3152.

[58] X. Wang, Y. Li, *J. Mater. Chem. A* **2016**, *4*, 5247.

[59] S. Ji, Y. Chen, Q. Fu, Y. Chen, J. Dong, W. Chen, Z. Li, Y. Wang, L. Gu, W. He, C. Chen, Q. Peng, Y. Huang, X. Duan, D. Wang, C. Draxl, Y. Li, *J. Am. Chem. Soc.* **2017**, *139*, 9795.

[60] C. Bai, A. Li, X. Yao, H. Liu, Y. Li, *Green Chem.* **2016**, *18*, 1061.

[61] L. Zuo, S. Chen, J. Wu, L. Wang, H. Hou, Y. Song, *RSC Adv.* **2014**, *4*, 61604.

[62] G. Xu, B. Ding, L. Shen, P. Nie, J. Han, X. Zhang, *J. Mater. Chem. A* **2013**, *1*, 4490.

[63] J. Li, Y. Chen, Y. Tang, S. Li, H. Dong, K. Li, M. Han, Y. Q. Lan, J. Bao, Z. Dai, *J. Mater. Chem. A* **2014**, *2*, 6316.

[64] J. Sen Li, S. L. Li, Y. J. Tang, K. Li, L. Zhou, N. Kong, Y. Q. Lan, J. C. Bao, Z. H. Dai, *Sci. Rep.* **2014**, *4*, 1.

[65] B. Liu, H. Shioyama, T. Akita, Q. Xu, *J. Am. Chem. Soc.* **2008**, *130*, 5390.

[66] B. Liu, H. Shioyama, H. Jiang, X. Zhang, Q. Xu, *Carbon N Y* **2010**, *48*, 456.

[67] H. Li, M. Eddaoudi, M. O'Keeffe, O. M. Yaghi, *Nature* **1999**, *402*, 276.

[68] N. Bakhtiari, S. Azizian, *ACS Omega* **2018**, *3*, 16954.

[69] J. Li, Q.-L. Zhu, Q. Xu, *Chem. Commun.* **2015**, *51*, 10827.

[70] S. Zhao, H. Yin, L. Du, L. He, K. Zhao, L. Chang, G. Yin, H. Zhao, S. Liu, Z. Tang, *ACS Nano* **2014**, *8*, 12660.

[71] Y. V. Kaneti, J. Tang, R. R. Salunkhe, X. Jiang, A. Yu, K. C. W. Wu, Y. Yamauchi, *Adv. Mater.* **2017**, *29*, 1604898.

[72] A. Banerjee, K. K. Upadhyay, D. Puthusseri, V. Aravindan, S. Madhavi, S. Ogale, *Nanoscale* **2014**, *6*, 4387.

[73] D. Yuan, J. Chen, S. Tan, N. Xia, Y. Liu, *Electrochem. Commun.* **2009**, *11*, 1191.

[74] H.-L. Jiang, B. Liu, Y.-Q. Lan, K. Kuratani, T. Akita, H. Shioyama, F. Zong, Q. Xu, *J. Am. Chem. Soc.* **2011**, *133*, 11854.

[75] M. Hu, J. Reboul, S. Furukawa, N. L. Torad, Q. Ji, P. Srinivasu, K. Ariga, S. Kitagawa, Y. Yamauchi, *J. Am. Chem. Soc.* **2012**, *134*, 2864.

[76] X. Pei, Y. Chen, S. Li, S. Zhang, X. Feng, J. Zhou, B. Wang, *Chinese J. Chem.* **2016**, *34*, 157.

[77] J.-S. Li, S.-L. Li, Y.-J. Tang, K. Li, L. Zhou, N. Kong, Y.-Q. Lan, J.-C. Bao, Z.-H. Dai, *Sci. Rep.* **2015**, *4*, 5130.

[78] Y. A. Fu, Y. Huang, Z. Xiang, G. Liu, D. Cao, *Eur. J. Inorg. Chem.* **2016**, *2016*, 2100.

[79] F. Zheng, Y. Yang, Q. Chen, *Nat. Commun.* **2014**, *5*, 5261.

[80] P. Su, H. Xiao, J. Zhao, Y. Yao, Z. Shao, C. Li, Q. Yang, *Chem. Sci.* **2013**, *4*, 2941.

[81] A. Aijaz, N. Fujiwara, Q. Xu, *J. Am. Chem. Soc.* **2014**, *136*, 6790.

[82] J. Liu, D. Zhu, C. Guo, A. Vasileff, S.-Z. Qiao, *Adv. Energy Mater.* **2017**, *7*, 1700518.

[83] Q. Ren, H. Wang, X.-F. Lu, Y.-X. Tong, G.-R. Li, *Adv. Sci.* **2018**, *5*, 1700515.

[84] I. A. Khan, Y. Qian, A. Badshah, M. A. Nadeem, D. Zhao, *ACS Appl. Mater. Interfaces* **2016**, *8*, 17268.

[85] H. M. Barkholtz, D.-J. Liu, *Mater. Horiz.* **2017**, *4*, 20.

[86] P. Zhang, F. Sun, Z. Xiang, Z. Shen, J. Yun, D. Cao, *Energy Environ. Sci.* **2014**, *7*, 442.

[87] B. Y. Xia, Y. Yan, N. Li, H. B. Wu, X. W. (David) Lou, X. Wang, *Nat. Energy* **2016**, *1*, 15006.

[88] W. Zhang, Z.-Y. Wu, H.-L. Jiang, S.-H. Yu, *J. Am. Chem. Soc.* **2014**, *136*, 14385.

[89] A. Zitolo, V. Goellner, V. Armel, M.-T. Sougrati, T. Mineva, L. Stievano, E. Fonda, F. Jaouen, *Nat. Mater.* **2015**, *14*, 937.

[90] P. Yin, T. Yao, Y. Wu, L. Zheng, Y. Lin, W. Liu, H. Ju, J. Zhu, X. Hong, Z. Deng, G. Zhou, S. Wei, Y. Li, *Angew. Chem., Int. Ed.* **2016**, *55*, 10800.

[91] Y. Hou, Z. Wen, S. Cui, S. Ci, S. Mao, J. Chen, *Adv. Funct. Mater.* **2015**, *25*, 872.

[92] S. Lim, K. Suh, Y. Kim, M. Yoon, H. Park, D. N. Dybtsev, K. Kim, *Chem. Commun.* **2012**, *48*, 7447.

[93] J. Hu, H. Wang, Q. Gao, H. Guo, *Carbon N Y* **2010**, *48*, 3599.

[94] S. J. Yang, T. Kim, J. H. Im, Y. S. Kim, K. Lee, H. Jung, C. R. Park, *Chem. Mater.* **2012**, *24*, 464.

[95] I. Ahmed, B. N. Bhadra, H. J. Lee, S. H. Jhung, *Catal. Today* **2018**, *301*, 90.

[96] A. Almasoudi, R. Mokaya, *J. Mater. Chem.* **2012**, *22*, 146.

[97] R. R. Salunkhe, J. Tang, Y. Kamachi, T. Nakato, J. H. Kim, Y. Yamauchi, *ACS Nano* **2015**, *9*, 6288.

[98] S. Salehi, S. Mandegarzad, M. Anbia, *J. Alloys Compd.* **2020**, *812*, 152051.

[99] B. N. Bhadra, S. H. Jhung, *J. Hazard. Mater.* **2017**, *340*, 179.

[100] Q.-L. Zhu, W. Xia, L.-R. Zheng, R. Zou, Z. Liu, Q. Xu, *ACS Energy Lett.* **2017**, *2*, 504.

[101] Y.-T. Xu, X. Xiao, Z.-M. Ye, S. Zhao, R. Shen, C.-T. He, J.-P. Zhang, Y. Li, X.-M. Chen, *J. Am. Chem. Soc.* **2017**, *139*, 5285.

[102] Q. Lai, L. Zheng, Y. Liang, J. He, J. Zhao, J. Chen, *ACS Catal.* **2017**, *7*, 1655.

[103] F. Cheng, W.-C. Li, J.-N. Zhu, W.-P. Zhang, A.-H. Lu, *Nano Energy* **2016**, *19*, 486.

[104] Q.-L. Zhu, W. Xia, T. Akita, R. Zou, Q. Xu, *Adv. Mater.* **2016**, *28*, 6391.

[105] Y. Ye, F. Cai, H. Li, H. Wu, G. Wang, Y. Li, S. Miao, S. Xie, R. Si, J. Wang, X. Bao, *Nano Energy* **2017**, *38*, 281.

[106] H. B. Wu, B. Y. Xia, L. Yu, X.-Y. Yu, X. W. (David) Lou, *Nat. Commun.* **2015**, *6*, 6512.

[107] Y. Chen, S. Ji, Y. Wang, J. Dong, W. Chen, Z. Li, R. Shen, L. Zheng, Z. Zhuang, D. Wang, Y. Li, *Angew. Chem., Int. Ed.* **2017**, *56*, 6937.

[108] C. D. Malonzo, S. M. Shaker, L. Ren, S. D. Prinslow, A. E. Platero-Prats, L. C. Gallington, J. Borycz, A. B. Thompson, T. C. Wang, O. K. Farha, J. T. Hupp, C. C. Lu, K. W. Chapman, J. C. Myers, R. L. Penn, L. Gagliardi, M. Tsapatsis, A. Stein, *J. Am. Chem. Soc.* **2016**, *138*, 2739.

[109] R. R. Salunkhe, Y. V. Kaneti, Y. Yamauchi, *ACS Nano* **2017**, *11*, 5293.

[110] L. Zhang, H. B. Wu, S. Madhavi, H. H. Hng, X. W. Lou, *J. Am. Chem. Soc.* **2012**, *134*, 17388.

[111] X. Xu, R. Cao, S. Jeong, J. Cho, *Nano Lett.* **2012**, *12*, 4988.

[112] S. Maiti, A. Pramanik, S. Mahanty, *CrystEngComm* **2016**, *18*, 450.

[113] W. Cho, Y. H. Lee, H. J. Lee, M. Oh, *Adv. Mater.* **2011**, *23*, 1720.

[114] W. Guo, W. Sun, L. P. Lv, S. Kong, Y. Wang, *ACS Nano* **2017**, *11*, 4198.

[115] T. T. Li, J. Qian, Y. Q. Zheng, *RSC Adv.* **2016**, *6*, 77358.

[116] Y. Wang, B. Wang, F. Xiao, Z. Huang, Y. Wang, C. Richardson, Z. Chen, L. Jiao, H. Yuan, *J. Power Sources* **2015**, *298*, 203.

[117] D. Tian, X.-L. Zhou, Y.-H. Zhang, Z. Zhou, X.-H. Bu, *Inorg. Chem.* **2015**, *54*, 8159.

[118] Y. Han, M. Zhao, L. Dong, J. Feng, Y. Wang, D. Li, X. Li, *J. Mater. Chem. A* **2015**, *3*, 22542.

[119] V. Soundharrajan, B. Sambandam, J. Song, S. Kim, J. Jo, S. Kim, S. Lee, V. Mathew, J. Kim, *ACS Appl. Mater. Interfaces* **2016**, *8*, 8546.

[120] G. Zeng, Y. Chen, L. Chen, P. Xiong, M. Wei, *Electrochim. Acta* **2016**, *222*, 773.

[121] T. K. Kim, K. J. Lee, J. Y. Cheon, J. H. Lee, S. H. Joo, H. R. Moon, *J. Am. Chem. Soc.* **2013**, *135*, 8940.

[122] B. Zhang, S. Hao, D. Xiao, J. Wu, Y. Huang, *Mater. Des.* **2016**, *98*, 319.

[123] F. Zheng, S. Xu, Z. Yin, Y. Zhang, L. Lu, *RSC Adv.* **2016**, *6*, 93532.

[124] S. Kong, R. Dai, H. Li, W. Sun, Y. Wang, *ACS Sustainable Chem. Eng.* **2015**, *3*, 1830.

[125] H. Pang, B. Guan, W. Sun, Y. Wang, *Electrochim. Acta* **2016**, *213*, 351.

[126] Y. Han, S. Zhang, N. Shen, D. Li, X. Li, *Mater. Lett.* **2017**, *188*, 1.

[127] Z. Xiu, M. H. Alfaruqi, J. Gim, J. Song, S. Kim, T. V Thi, P. T. Duong, J. P. Baboo, V. Mathew, J. Kim, *Chem. Commun.* **2015**, *51*, 12274.

[128] Z. Xiu, M. H. Alfaruqi, J. Gim, J. Song, S. Kim, P. T. Duong, J. P. Baboo, V. Mathew, J. Kim, *J. Alloy. Compd.* **2016**, *674*, 174.

[129] C. Li, Z. Li, Q. Li, Z. Zhang, S. Dong, L. Yin, *Electrochim. Acta* **2016**, *215*, 689.

[130] X. Zhang, M. Wang, G. Zhu, D. Li, D. Yan, T. Lu, L. Pan, *Ceram. Int.* **2017**, *43*, 2398.

[131] Y. Kimitsuka, E. Hosono, S. Ueno, H. Zhou, S. Fujihara, *Inorg. Chem.* **2013**, *52*, 14028.

[132] T. Wang, L. Shi, J. Tang, V. Malgras, S. Asahina, G. Liu, H. Zhang, X. Meng, K. Chang, J. He, O. Terasaki, Y. Yamauchi, J. Ye, *Nanoscale* **2016**, *8*, 6712.

[133] Y. Feng, H. Lu, X. Gu, J. Qiu, M. Jia, C. Huang, J. Yao, *J. Phys. Chem. Solids* **2017**, *102*, 110.

[134] H. Guo, T. Li, W. Chen, L. Liu, X. Yang, Y. Wang, Y. Guo, *Nanoscale* **2014**, *6*, 15168.

[135] J. Yang, H. Ye, Z. Zhang, F. Zhao, B. Zeng, *Sens. Actuators, B* **2017**, *242*, 728.

[136] F. Zheng, D. Zhu, X. Shi, Q. Chen, *J. Mater. Chem. A* **2015**, *3*, 2815.

[137] M. Du, D. He, Y. Lou, J. Chen, *J Energy Chem* **2017**, *26*, 673.

[138] R. Wu, X. Qian, K. Zhou, J. Wei, J. Lou, P. M. Ajayan, *ACS Nano* **2014**, *8*, 6297.

[139] J. Zhao, F. Wang, P. Su, M. Li, J. Chen, Q. Yang, C. Li, *J. Mater. Chem.* **2012**, *22*, 13328.

[140] H. Hu, B. Guan, B. Xia, W. X. Lou, *J. Am. Chem. Soc.* **2015**, *137*, 5590.

[141] X.-W. Hu, S. Liu, B.-T. Qu, X.-Z. You, *ACS Appl. Mater. Interfaces* **2015**, *7*, 9972.

[142] L. Hu, Y. Huang, F. Zhang, Q. Chen, *Nanoscale* **2013**, *5*, 4186.

[143] W. Guo, W. Sun, Y. Wang, *ACS Nano* **2015**, *9*, 11462.

[144] I. Mondal, U. Pal, *Phys. Chem. Chem. Phys.* **2016**, *18*, 4780.

[145] B. Wang, Y. Wang, Y. Cui, Y. Yang, Z. Wang, B. Chen, G. Qian, *Microporous Mesoporous Mater.* **2015**, *203*, 86.

[146] K. E. deKrafft, C. Wang, W. Lin, *Adv. Mater.* **2012**, *24*, 2014.

[147] G. Huang, L. Zhang, F. Zhang, L. Wang, *Nanoscale* **2014**, *6*, 5509.

[148] P. Su, S. Liao, F. Rong, F. Wang, J. Chen, C. Li, Q. Yang, *J. Mater. Chem. A* **2014**, *2*, 17408.

[149] F. Zhang, L. Hao, L. Zhang, X. Zhang, *Int. J. Electrochem. Sci.* **2011**, *6*, 2943.

[150] Y. Chen, Y. Wang, H. Yang, H. Gan, X. Cai, X. Guo, B. Xu, M. Lü, A. Yuan, *Ceram. Int.* **2017**, *43*, 9945.

[151] F. Meng, Z. Fang, Z. Li, W. Xu, M. Wang, Y. Liu, J. Zhang, W. Wang, D. Zhao, X. Guo, *J. Mater. Chem. A* **2013**, *1*, 7235.

[152] R. Wu, X. Qian, X. Rui, H. Liu, B. Yadian, K. Zhou, J. Wei, Q. Yan, X.-Q. Q. Feng, Y. Long, L. Wang, Y. Huang, *Small* **2014**, *10*, 1932.

[153] C. Li, T. Chen, W. Xu, X. Lou, L. Pan, Q. Chen, B. Hu, *J. Mater. Chem. A* **2015**, *3*, 5585.

[154] Q. Lan, Z.-M. Zhang, C. Qin, X.-L. Wang, Y.-G. Li, H.-Q. Tan, E.-B. Wang, *Chem. – A Eur. J.* **2016**, *22*, 15513.

[155] Z. Sun, C. Cao, W. Q. Han, *RSC Adv.* **2015**, *5*, 72825.

[156] R. Wu, X. Qian, F. Yu, H. Liu, K. Zhou, J. Wei, Y. Huang, *J. Mater. Chem. A* **2013**, *1*, 11126.

[157] S. J. Yang, J. H. Im, T. Kim, K. Lee, C. R. Park, *J. Hazard. Mater.* **2011**, *186*, 376.

[158] E. Shamsaei, F. Basquiroto de Souza, K. Sagoe-Crentsil, W. Duan, *Microporous Mesoporous Mater.* **2022**, *332*, 111702.

[159] Z.-X. Li, G. Ye, J. Han, Y. Yang, K.-Y. Zou, X. Wang, X.-L. Wang, X.-F. Gou, *Dalt. Trans.* **2015**, *44*, 9209.

[160] M. Zhong, L. Kong, N. Li, Y.-Y. Liu, J. Zhu, X.-H. Bu, *Coord. Chem. Rev.* **2019**, *388*, 172.

[161] P. Yang, X. Song, C. Jia, H.-S. Chen, *J Ind Eng Chem* **2018**, *62*, 250.

[162] Y. Song, X. Li, C. Wei, J. Fu, F. Xu, H. Tan, J. Tang, L. Wang, *Sci. Rep.* **2015**, *5*, 8401.

[163] Z. Jiang, H. Sun, Z. Qin, X. Jiao, D. Chen, *Chem. Commun.* **2012**, *48*, 3620.

[164] Z. Jiang, Z. Li, Z. Qin, H. Sun, X. Jiao, D. Chen, *Nanoscale* **2013**, *5*, 11770.

[165] H. Liu, G. Xia, R. Zhang, P. Jiang, J. Chen, Q. Chen, *RSC Adv.* **2017**, *7*, 3686.

[166] C. W. Abney, K. M. L. Taylor-Pashow, S. R. Russell, Y. Chen, R. Samantaray, J. V. Lockard, W. Lin, *Chem. Mater.* **2014**, *26*, 5231.

[167] A. Cabrera-García, A. Vidal-Moya, Á. Bernabeu, J. Sánchez-González, E. Fernández, P. Botella, *Dalt. Trans.* **2015**, *44*, 14034.

[168] A. Kondo, A. S. Hall, T. E. Mallouk, K. Maeda, *Chem. – A Eur. J.* **2015**, *21*, 12148.

[169] J. Zhang, Y. Luan, Z. Lyu, L. Wang, L. Xu, K. Yuan, F. Pan, M. Lai, Z. Liu, W. Chen, *Nanoscale* **2015**, *7*, 14881.

[170] D. Cai, B. Liu, D. Wang, L. Wang, Y. Liu, B. Qu, X. Duan, Q. Li, T. Wang, *J. Mater. Chem. A* **2016**, *4*, 183.

[171] F. Zou, X. Hu, Z. Li, L. Qie, C. Hu, R. Zeng, Y. Jiang, Y. Huang, *Adv. Mater.* **2014**, *26*, 6622.

[172] C. Sun, J. Yang, X. Rui, W. Zhang, Q. Yan, P. Chen, F. Huo, W. Huang, X. Dong, *J. Mater. Chem. A* **2015**, *3*, 8483.

[173] D. Yu, B. Wu, L. Ge, L. Wu, H. Wang, T. Xu, *J. Mater. Chem. A* **2016**, *4*, 10878.

[174] J. Tang, R. R. Salunkhe, J. Liu, N. L. Torad, M. Imura, S. Furukawa, Y. Yamauchi, *J. Am. Chem. Soc.* **2015**, *137*, 1572.

[175] H. Zhong, J. Wang, Y. Zhang, W. Xu, W. Xing, D. Xu, Y. Zhang, X. Zhang, *Angew Chem Int Ed Engl* **2014**, *53*, 14235.

[176] Y. Hou, T. Huang, Z. Wen, S. Mao, S. Cui, J. Chen, *Adv. Energy Mater.* **2014**, *4*, 1400337.

[177] C. Wei, X. Li, F. Xu, H. Tan, Z. Li, L. Sun, Y. Song, *Anal. Methods* **2014**, *6*, 1550.

[178] L. He, L. Li, T. Wang, H. Gao, G. Li, X. Wu, Z. Su, C. Wang, *Dalt. Trans.* **2014**, *43*, 16981.

[179] K.-Y. Andrew Lin, F.-K. Hsu, W.-D. Lee, *J. Mater. Chem. A* **2015**, *3*, 9480.

[180] P. Liang, C. Zhang, H. Sun, S. Liu, M. Tadé, S. Wang, *RSC Adv.* **2016**, *6*, 95903.

[181] K.-Y. A. Lin, F.-K. Hsu, *RSC Adv.* **2015**, *5*, 50790.

[182] H. Chen, K. Shen, J. Chen, X. Chen, Y. Li, *J. Mater. Chem. A* **2017**, *5*, 9937.

[183] X. Ge, Z. Li, C. Wang, L. Yin, *ACS Appl. Mater. Interfaces* **2015**, *7*, 26633.

[184] Y. Zhao, X. Li, J. Liu, C. Wang, Y. Zhao, G. Yue, *ACS Appl. Mater. Interfaces* **2016**, *8*, 6472.

[185] Z. Li, C. Li, X. Ge, J. Ma, Z. Zhang, Q. Li, C. Wang, L. Yin, *Nano Energy* **2016**, *23*, 15.

[186] F. Cao, M. Zhao, Y. Yu, B. Chen, Y. Huang, J. Yang, X. Cao, Q. Lu, X. Zhang, Z. Zhang, C. Tan, H. Zhang, *J. Am. Chem. Soc.* **2016**, *138*, 6924.

[187] S. Chen, M. Xue, Y. Li, Y. Pan, L. Zhu, D. Zhang, Q. Fang, S. Qiu, *Inorg. Chem. Front.* **2015**, *2*, 177.

[188] W. Meng, W. Chen, L. Zhao, Y. Huang, M. Zhu, Y. Huang, Y. Fu, F. Geng, J. Yu, X. Chen, C. Zhi, *Nano Energy* **2014**, *8*, 133.

[189] S. Ullah, I. A. Khan, M. Choucair, A. Badshah, I. Khan, M. A. Nadeem, *Electrochim. Acta* **2015**, *171*, 142.

[190] G. C. Li, P. F. Liu, R. Liu, M. Liu, K. Tao, S. R. Zhu, M. K. Wu, F. Y. Yi, L. Han, *Dalt. Trans.* **2016**, *45*, 13311.

[191] X. Cao, B. Zheng, W. Shi, J. Yang, Z. Fan, Z. Luo, X. Rui, B. Chen, Q. Yan, H. Zhang, *Adv. Mater.* **2015**, *27*, 4695.

[192] J. Xu, S. C. Liu, Y. Liu, *RSC Adv.* **2016**, *6*, 52137.

[193] H. Bin Wu, S. Wei, L. Zhang, R. Xu, H. H. Hng, X. W. Lou, *Chem. – A Eur. J.* **2013**, *19*, 10804.

[194] S. J. Yang, S. Nam, T. Kim, J. H. Im, H. Jung, J. H. Kang, S. Wi, B. Park, C. R. Park, *J. Am. Chem. Soc.* **2013**, *135*, 7394.

[195] Z. Wang, X. Li, Y. Yang, Y. Cui, H. Pan, Z. Wang, B. Chen, G. Qian, *J. Mater. Chem. A* **2014**, *2*, 7912.

[196] G. Fang, J. Zhou, C. Liang, A. Pan, C. Zhang, Y. Tang, X. Tan, J. Liu, S. Liang, *Nano Energy* **2016**, *26*, 57.

[197] G. Zhang, S. Hou, H. Zhang, W. Zeng, F. Yan, C. C. Li, H. Duan, *Adv. Mater.* **2015**, *27*, 2400.

[198] S. L. Zhang, B. Y. Guan, H. Bin Wu, X. W. D. Lou, *Nano-Micro Lett.* **2018**, *10*, 1.

[199] X. Cao, B. Zheng, X. Rui, W. Shi, Q. Yan, H. Zhang, *Angew Chem Int Ed Engl* **2014**, *53*, 1404.

[200] P. Qi, Y. Han, J. Zhou, X. Fu, S. Li, J. Zhao, L. Wang, X. Fan, X. Feng, B. Wang, *Chem. Commun.* **2015**, *51*, 12391.

[201] T. Liu, C. Dai, M. Jia, D. Liu, S. Bao, J. Jiang, M. Xu, C. M. Li, *ACS Appl. Mater. Interfaces* **2016**, *8*, 16063.

[202] S. Bala, I. Mondal, A. Goswami, U. Pal, R. Mondal, *J. Mater. Chem. A* **2015**, *3*, 20288.

[203] B. Niu, D. Wu, J. Wang, L. Wang, W. Zhang, *Appl. Surf. Sci.* **2020**, *528*, 146965.

[204] P. Huang, J. Lei, Z. Sun, Xiang Hu, *Chemosphere* **2021**, *268*, 129157.

[205] J. Wang, M. Xu, X. Liang, Y. Zhang, D. Yang, L. Pan, W. Fang, C. G. Zhu, F. Wang, *Sep. Purif. Technol.* **2021**, *263*, 118368.

[206] D. Chen, S. Chen, Y. Jiang, S. Xie, H. Quan, L. Hua, X. Luo, L. Guo, *RSC Adv.* **2017**, *7*, 49024.

[207] J. Tang, J. Wang, *Chem. Eng. J.* **2019**, *375*, 122007.

[208] S. Yang, X. Qiu, P. Jin, M. Dzakpasu, X. C. Wang, Q. Zhang, L. zhang, L. Yang, D. Ding, W. Wang, K. Wu, *Chem. Eng. J.* **2018**, *353*, 329.

[209] X. Cao, C. Tan, M. Sindoro, H. Zhang, *Chem. Soc. Rev.* **2017**, *46*, 2660.

[210] J. Wei, Y. Feng, Y. Liu, Y. Ding, *J. Mater. Chem. A* **2015**, *3*, 22300.

[211] Y. Han, P. Qi, S. Li, X. Feng, J. Zhou, H. Li, S. Su, X. Li, B. Wang, *Chem. Commun.* **2014**, *50*, 8057.

[212] Q. Li, P. Xu, W. Gao, S. Ma, G. Zhang, R. Cao, J. Cho, H.-L. Wang, G. Wu, *Adv. Mater.* **2014**, *26*, 1378.

[213] X.-Y. Yu, L. Yu, H. B. Wu, X. W. (David) Lou, *Angew. Chem., Int. Ed.* **2015**, *54*, 5331.

[214] K. Cho, S.-H. Han, M. P. Suh, *Angew. Chem., Int. Ed.* **2016**, *55*, 15301.

[215] Y. Su, D. Ao, H. Liu, Y. Wang, *J. Mater. Chem. A* **2017**, *5*, 8680.

[216] J.-D. Xiao, H.-L. Jiang, *Small* **2017**, *13*, 1700632.

[217] X. Sun, H. Huang, C. P. Wang, Y. Y. Liu, T. L. Hu, X. H. Bu, *ChemElectroChem* **2018**, *5*, 3639.

[218] S. Jeoung, B. Seo, J. M. Hwang, S. H. Joo, H. R. Moon, *Mater. Chem. Front.* **2017**, *1*, 973.

[219] H. Tabassum, W. Guo, W. Meng, A. Mahmood, R. Zhao, Q. Wang, R. Zou, *Adv. Energy Mater.* **2017**, *7*, 1601671.

[220] Y. J. Tang, M. R. Gao, C. H. Liu, S. L. Li, H. L. Jiang, Y. Q. Lan, M. Han, S. H. Yu, *Angew. Chem., Int. Ed.* **2015**, *54*, 12928.

[221] L. Fan, P. F. Liu, X. Yan, L. Gu, Z. Z. Yang, H. G. Yang, S. Qiu, X. Yao, *Nat. Commun.* **2016**, *7*, 1.

ADVANCED
SCIENCE NEWS

www.advancedsciencenews.com

NANO · MICRO

small

www.small-journal.com

[222] Y. Xu, W. Tu, B. Zhang, S. Yin, Y. Huang, M. Kraft, R. Xu, *Adv. Mater.* **2017**, *29*, 1605957.

[223] S. Ma, G. A. Goenaga, A. V Call, D.-J. Liu, *Chem. – A Eur. J.* **2011**, *17*, 2063.

[224] E. Proietti, F. Jaouen, M. Lefèvre, N. Larouche, J. Tian, J. Herranz, J.-P. Dodelet, *Nat. Commun.* **2011**, *2*, 1.

[225] J. M. Cho, B. G. Kim, G. Y. Han, J. Sun, H. K. Jeong, J. W. Bae, *Fuel* **2020**, *281*, 118779.

[226] C. Zhang, Q. Liu, P. Wang, J. Zhu, D. Chen, Y. Yang, Y. Zhao, Z. Pu, S. Mu, *Small* **2021**, *17*, 2104241.

[227] Q. Wang, T. Su, Y. Wang, Y. Chen, X. Lu, R. Ma, Y. Fu, W. Zhu, *ACS Sustainable Chem. Eng.* **2020**, *8*, 17008.

[228] X. Xu, F. Nosheen, X. Wang, *Chem. Mater.* **2016**, *28*, 6313.

[229] L. Kong, Q. Chen, X. Shen, Z. Xu, C. Xu, Z. Ji, J. Zhu, *Electrochim. Acta* **2018**, *265*, 651.

[230] S. Hu, S. Wang, C. Feng, H. Wu, J. Zhang, H. Mei, *ACS Sustainable Chem. Eng.* **2020**, *8*, 7414.

[231] K. Ye, Z. He, F. Wu, Y. Wang, L. Wang, Y. Cheng, Y.-H. Zhou, *Int. J. Hydrogen Energy* **2021**, *46*, 35319.

[232] Y. Liu, L. Liu, L. Kang, F. Ran, *J. Power Sources* **2020**, *450*, 227687.

[233] R. Wu, D. P. Wang, X. Rui, B. Liu, K. Zhou, A. W. K. Law, Q. Yan, J. Wei, Z. Chen, *Adv. Mater.* **2015**, *27*, 3038.

[234] J. Martí-Rujas, *Dalt. Trans.* **2020**, *49*, 13897.

[235] S. Subudhi, S. P. Tripathy, K. Parida, *Catal. Sci. Technol.* **2021**, *11*, 392.

[236] P. Hirschle, T. Preiß, F. Auras, A. Pick, J. Völkner, D. Valdepérez, G. Witte, W. J. Parak, J. O. Rädler, S. Wuttke, *CrystEngComm* **2016**, *18*, 4359.

[237] F. Gándara, T. D. Bennett, *IUCrJ* **2014**, *1*, 563.

[238] C. E. Wilmer, M. Leaf, C. Y. Lee, O. K. Farha, B. G. Hauser, J. T. Hupp, R. Q. Snurr, *Nat. Chem.* **2012**, *4*, 83.

[239] D. H. O. Ch. Baerlocher, L. B. McCusker, *Atlas of Zeolite Framework Types*, Elsevier Ltd., Cham **2007**.

[240] J. Sun, C. Bonneau, Á. Cantín, A. Corma, M. J. Díaz-Cabãas, M. Moliner, D. Zhang, M. Li, X. Zou, *Nature* **2009**, *458*, 1154.

[241] D. Xie, L. B. McCusker, C. Baerlocher, *J. Am. Chem. Soc.* **2011**, *133*, 20604.

[242] L. Palatinus, *Acta Crystallogr., Sect. B: Struct. Sci., Cryst. Eng. Mater.* **2013**, *69*, 1.

[243] M. Aghajanzadeh, M. Zamani, H. Molavi, H. Khieri Manjili, H. Danafar, A. Shojaei, *J. Inorg. Organomet. Polym. Mater.* **2018**, *28*, 177.

[244] T. A. Vu, G. H. Le, C. D. Dao, L. Q. Dang, K. T. Nguyen, Q. K. Nguyen, P. T. Dang, H. T. K. Tran, Q. T. Duong, T. V. Nguyen, G. D. Lee, *RSC Adv.* **2015**, *5*, 5261.

[245] M. M. Peng, U. J. Jeon, M. Ganesh, A. Aziz, R. Vinodh, M. Palanichamy, H. T. Jang, *Bull. Korean Chem. Soc.* **2014**, *35*, 3213.

[246] A. Yang, P. Li, J. Zhong, *RSC Adv.* **2019**, *9*, 10320.

[247] J. H. Cavka, S. Jakobsen, U. Olsbye, N. Guillou, C. Lamberti, S. Bordiga, K. P. Lillerud, *J. Am. Chem. Soc.* **2008**, *130*, 13850.

[248] A. Altomare, C. Cuocci, C. Giacovazzo, A. Moliterni, R. Rizzi, N. Corriero, A. Falcicchio, *J. Appl. Crystallogr.* **2013**, *46*, 1231.

[249] M. I. Gonzalez, J. A. Mason, E. D. Bloch, S. J. Teat, K. J. Gagnon, G. Y. Morrison, W. L. Queen, J. R. Long, *Chem. Sci.* **2017**, *8*, 4387.

[250] F. Luo, C. Yan, L. Dang, R. Krishna, W. Zhou, H. Wu, X. Dong, Y. Han, T. L. Hu, M. O'Keeffe, L. Wang, M. Luo, R. B. Lin, B. Chen, *J. Am. Chem. Soc.* **2016**, *138*, 5678.

[251] W. Chen, Z. Wang, Q. Wang, K. El-Yanboui, K. Tan, H. M. Barkholtz, D. J. Liu, P. Cai, L. Feng, Y. Li, J. S. Qin, S. Yuan, D. Sun, H. C. Zhou, *J. Am. Chem. Soc.* **2023**, *145*, 4736.

[252] M. Maliuta, I. Senkovska, R. Thümmler, S. Ehrling, S. Becker, V. Romaka, V. Bon, J. D. Evans, S. Kaskel, *Dalt. Trans.* **2023**, *52*, 2816.

[253] Y. Lai, F. Wang, Y. Zhang, P. Ou, P. Wu, Q. Fang, Z. Chen, S. Li, *Chem. Eng. J.* **2019**, *378*, 122069.

[254] X. Li, B. Zhang, Y. Fang, W. Sun, Z. Qi, Y. Pei, S. Qi, P. Yuan, X. Luan, T. W. Goh, W. Huang, *Chem. – A Eur. J.* **2017**, *23*, 4266.

[255] A. Umemura, S. Diring, S. Furukawa, H. Uehara, T. Tsuruoka, S. Kitagawa, *J. Am. Chem. Soc.* **2011**, *133*, 15506.

[256] J. Zhang, N. Cheng, B. Ge, *Adv Phys X* **2022**, *7*, 2046157.

[257] D. Aulakh, L. Liu, J. R. Varghese, H. Xie, T. Islamoglu, K. Duell, C. W. Kung, C. E. Hsiung, Y. Zhang, R. J. Drout, O. K. Farha, K. R. Dunbar, Y. Han, M. Wriedt, *J. Am. Chem. Soc.* **2019**, *141*, 2997.

[258] Y. Li, K. Wang, W. Zhou, Y. Li, R. Vila, W. Huang, H. Wang, G. Chen, G. H. Wu, Y. Tsao, H. Wang, R. Sinclair, W. Chiu, Y. Cui, *Matter* **2019**, *1*, 428.

[259] D. Xu, Y. Pan, M. Chen, Q. Pan, L. Zhu, M. Xue, D. Zhang, Q. Fang, S. Qiu, *RSC Adv.* **2017**, 26377.

[260] D. Xu, D. Zhang, H. Zou, L. Zhu, M. Xue, Q. Fang, *ChemComm* **2016**, 10513.

[261] M. Zahid, M. Bahri, W. R. Heinz, Q. Jia, O. Ersen, T. Kratky, R. A. Fischer, Y. Zhu, Y. Xia, *Microporous Mesoporous Mater.* **2021**, *316*, 110957.

[262] J. Zhang, N. Cheng, B. Ge, *Adv Phys X* **2022**, *7*.

[263] Z. Wang, X. Ke, K. Zhou, X. Xu, Y. Jin, H. Wang, M. Sui, *J. Mater. Chem. A* **2021**, 18515.

[264] C. Ying-Bo, Z. Lin-Fei, W. Biao, H. Xiao-Yu, L. Dong-Qing, Z. Feng-Xiao, Z. Yu-Feng, *Tianjin Gongye Daxue Xuebao* **2016**, *35*, 1.

[265] M. Díaz-García, Á. Mayoral, I. Díaz, M. Sánchez-Sánchez, *Cryst. Growth Des.* **2014**, *14*, 2479.

[266] C. Wiktor, M. Meledina, S. Turner, O. I. Lebedev, R. A. Fischer, *J. Mater. Chem. A* **2017**, *5*, 14969.

[267] C. W., L. Y. Chou, L. Long, X. Si, W. S. Lo, C. K. Tsung, T. Li, *ACS Appl. Mater. Interfaces* **2019**, *11*, 35820.

[268] F. Marpaung, M. Kim, J. H. Khan, K. Konstantinov, Y. Yamauchi, M. S. A. Hossain, J. Na, J. Kim, *Chem. – An Asian J.* **2019**, *14*, 1331.

[269] T. Wang, H. K. Kim, Y. Liu, W. Li, J. T. Griffiths, Y. Wu, S. Laha, K. D. Fong, F. Podjaski, C. Yun, R. V. Kumar, B. V. Lotsch, A. K. Cheetham, S. K. Smoukov, *J. Am. Chem. Soc.* **2018**, *140*, 6130.

[270] R. Brent, P. Cubillas, S. M. Stevens, K. E. Jelfs, A. Umemura, J. T. Gebbie, B. Slater, O. Terasaki, M. A. Holden, M. W. Anderson, *J. Am. Chem. Soc.* **2010**, *132*, 13858.

[271] N. S. John, C. Scherb, M. Shöâeè, M. W. Anderson, M. P. Attfield, T. Bein, *Chem. Commun.* **2009**, *2*, 6294.

[272] P. Y. Moh, P. Cubillas, M. W. Anderson, M. P. Attfield, *J. Am. Chem. Soc.* **2011**, *133*, 13304.

[273] D. Bradshaw, A. Garai, J. Huo, *Chem. Soc. Rev.* **2012**, *41*, 2344.

[274] A. McPherson, Y. G. Kuznetsov, A. Malkin, M. Plomp, *J Struct Biol* **2003**, *142*, 32.

[275] H. H. Teng, P. M. Dove, J. J. De Yoreo, *Geochim. Cosmochim. Acta* **2000**, *64*, 2255.

[276] M. A. Holden, P. Cubillas, M. W. Anderson, *Chem. Commun.* **2010**, *46*, 1047.

[277] P. Cubillas, M. A. Holden, M. W. Anderson, *Cryst. Growth Des.* **2011**, *11*, 3163.

[278] M. Shoaee, M. W. Anderson, M. P. Attfield, *Angew. Chemie – Int. Ed.* **2008**, *47*, 8525.

[279] A. Engel, D. J. Müller, *Nat Struct Biol* **2000**, *7*, 715.

[280] R. García, R. Pérez, *Surf. Sci. Rep.* **2002**, *47*, 197.

[281] C. A. Amo, A. P. Perrino, A. F. Payam, R. Garcia, *ACS Nano* **2017**, *11*, 8650.

[282] M. Liu, W. Zheng, S. Ran, S. T. Boles, L. Y. S. Lee, *Adv. Mater. Interfaces* **2018**, *5*, 1.

[283] R. A. W. Worrall, D. Stephen, Bissett, A. Mark, Attfield, P. Martin, Dryfe, *CrystEngComm* **2018**, *20*, 4421.

[284] L. D. B. Mandemaker, M. Filez, G. Delen, H. Tan, X. Zhang, D. Lohse, B. M. Weckhuysen, *J. Phys. Chem. Lett.* **2018**, *9*, 1838.

[285] M. Damircheli, A. F. Payam, R. Garcia, *Beilstein J. Nanotechnol.* **2015**, 1072.

ADVANCED
SCIENCE NEWS

www.advancedsciencenews.com

NANO · MICRO
small
www.small-journal.com

[286] R. Garcia, *Chem. Soc. Rev.* **2020**, *49*, 5850.

[287] A. F. Payam, Springer, Singapore **2018**, https://doi.org/10.1007/978-981-13-2417-8_2.

[288] M. Shöâeè, J. R. Agger, M. W. Anderson, M. P. Attfield, *CrystEngComm* **2008**, *10*, 646.

[289] P. Cubillas, M. W. Anderson, M. P. Attfield, *Chem. – A Eur. J.* **2012**, *18*, 15406.

[290] S. Chiodini, D. Reinares-Fisac, F. M. Espinosa, E. Gutiérrez-Puebla, A. Monge, F. Gándara, R. Garcia, *Sci. Rep.* **2017**, *7*, 11088.

[291] Y. Sun, Z. Hu, D. Zhao, K. Zeng, *ACS Appl. Mater. Interfaces* **2017**, *9*, 32202.

[292] Z. Zeng, J. C. Tan, *ACS Appl. Mater. Interfaces* **2017**, *9*, 39839.

[293] A. Kumar, K. Banerjee, A. S. Foster, P. Liljeroth, *Nano Lett.* **2018**, *18*, 5596.

[294] J. Sablowski, J. Linnemann, S. Hempel, V. Hoffmann, S. Unz, M. Beckmann, L. Giebeler, *Sci. Rep.* **2018**, *8*, 1.

[295] N. C. Robb, *Biochim Biophys Acta Mol Basis Dis* **2022**, *1868*, 166347.

[296] S. Castelletto, A. Boretti, *Chem. Phys. Impact* **2021**, *2*, 100013.

[297] S. W. Hell, J. Wichmann, *Opt. Lett.* **1994**, *19*, 780.

[298] M. G. L. Gustafsson, *J Microsc* **2000**, *198*, 82.

[299] J. Zhao, I. D. Chremmos, Z. Zhang, Y. Hu, D. Song, P. Zhang, N. K. Efremidis, Z. Chen, *Sci. Bull.* **2015**, *60*, 1157.

[300] M. Ma, A. Gross, D. Zacher, A. Pinto, H. Noei, Y. Wang, R. A. Fischer, N. Metzler-Nolte, *CrystEngComm* **2011**, *13*, 2828.

[301] W. Schrimpf, J. Jiang, Z. Ji, P. Hirschle, D. C. Lamb, O. M. Yaghi, S. Wuttke, *Nat. Commun.* **2018**, *9*, 1.

[302] R. Ameloot, F. Vermoortele, J. Hofkens, F. C. De Schryver, D. E. De Vos, M. B. J. Roeffaers, *Angew. Chemie* **2013**, *125*, 419.

[303] J. Rosário, L. L. da Luz, R. Geris, J. G. S. Ramalho, A. F. da Silva, S. A. Júnior, M. Malta, *Sci. Rep.* **2019**, *9*, 1.

[304] S. Schunter, R. Villa, V. Flynn, J. B. Heidelberger, A. K. Classen, P. Beli, P. B. Becker, *PLoS One* **2017**, *12*, 1.

[305] Y. Z. Chen, B. Gu, T. Uchida, J. Liu, X. Liu, B. J. Ye, Q. Xu, H. L. Jiang, *Nat. Commun.* **2019**, *10*, 1.

[306] M. Mendt, F. Gutt, N. Kavoosi, V. Bon, I. Senkovska, S. Kaskel, A. Pöppl, *J. Phys. Chem. C* **2016**, *120*, 14246.

[307] D. M. Polyukhov, S. Krause, V. Bon, A. S. Poryvaev, S. Kaskel, M. V. Fedin, *J. Phys. Chem. Lett.* **2020**, *11*, 5856.

[308] N.d.

[309] G. Mínguez Espallargas, E. Coronado, *Chem. Soc. Rev.* **2018**, *47*, 533.

[310] A. Kultaeva, T. Biktagirov, J. Bergmann, L. Hensel, H. Krautscheid, A. Pöppl, *Phys. Chem. Chem. Phys.* **2017**, *19*, 31030.

[311] M. Šimenas, M. Kobalz, M. Mendt, P. Eckold, H. Krautscheid, J. Banys, A. Pöppl, *J. Phys. Chem. C* **2015**, *119*, 4898.

[312] M. Thommes, K. A. Cychosz, *Adsorption* **2014**, *20*, 233.

[313] A. J. Howarth, A. W. Peters, N. A. Vermeulen, T. C. Wang, J. T. Hupp, O. K. Farha, *Chem. Mater.* **2017**, *29*, 26.

[314] F. Liu, S. Song, G. Cheng, W. Xiong, L. Shi, Y. Zhang, *Adsorpt. Sci. Technol.* **2018**, *36*, 1550.

[315] O. Pajuelo-Corral, S. Pérez-Yáñez, I. J. Vitorica-Yrezabal, G. Beobide, A. Zabala-Lekuona, A. Rodríguez-Diéguez, J. M. Seco, J. Cepeda, *Mater. Today Chem.* **2022**, *24*.

[316] D. Lenzen, J. Zhao, S. J. Ernst, M. Wahiduzzaman, A. Ken Inge, D. Fröhlich, H. Xu, H. J. Bart, C. Janiak, S. Henninger, G. Maurin, X. Zou, N. Stock, *Nat. Commun.* **2019**, *10*, 1.

[317] C. A. Ponte, M. Química, **2020**.

[318] F. Zhou, J. Zhou, X. Gao, C. Kong, L. Chen, *RSC Adv.* **2017**, *7*, 3713.

[319] B. C. R. Camacho, R. P. P. L. Ribeiro, I. A. A. C. Esteves, J. P. B. Mota, *Sep. Purif. Technol.* **2015**, *141*, 150.

[320] S. Ullah, M. A. Bustam, M. A. Assiri, A. G. Al-Sehemi, M. Sagir, F. A. Abdul Kareem, A. E. I. Elkhalifah, A. Mukhtar, G. Gonfa, *Microporous Mesoporous Mater.* **2019**, *288*, 109569.

[321] K. S. W. Sing, *Adv. Colloid Interface Sci.* **1998**, *76–77*, 3.

[322] J. Bedia, V. Muelas-Ramos, M. Peñas-Garzón, A. Gómez-Avilés, J. J. Rodríguez, C. Belver, *Catalysts* **2019**, *9*, 52.

[323] P. Sinha, A. Datar, C. Jeong, X. Deng, Y. G. Chung, L. C. Lin, *J. Phys. Chem. C* **2019**, *123*, 20195.

[324] B. K. Ku, D. E. Evans, *Aerosol Sci. Technol.* **2012**, *46*, 473.

[325] G. Kupgan, T. P. Liyana-Arachchi, C. M. Colina, *Langmuir* **2017**, *33*, 11138.

[326] Y. H. Tan, J. A. Davis, K. Fujikawa, N. V. Ganesh, A. V. Demchenko, K. J. Stine, *J. Mater. Chem.* **2012**, *22*, 6733.

[327] F. Haghighatju, H. H. Rafsanjani, F. Esmaeilzadeh, *Micro Nano Lett.* **2017**, *12*, 1.

[328] D. Lv, Y. Chen, Y. Li, R. Shi, H. Wu, X. Sun, J. Xiao, H. Xi, Q. Xia, Z. Li, *J. Chem. Eng. Data* **2017**, *62*, 2030.

[329] A. Martinez Joaristi, J. Juan-Alcañiz, P. Serra-Crespo, F. Kapteijn, J. Gascon, *Cryst. Growth Des.* **2012**, *12*, 3489.

[330] Q. Shi, Z. Chen, Z. Song, J. Li, J. Dong, *Angew. Chemie – Int. Ed.* **2011**, *50*, 672.

[331] N. L. Torad, R. R. Salunkhe, Y. Li, H. Hamoudi, M. Imura, Y. Sakka, C. C. Hu, Y. Yamauchi, *Chem. – A Eur. J.* **2014**, *20*, 7895.

[332] M. Afzan, S. M. Shima, Z. Z. Uba, N. T. Ubaidah, S. Bahruddin, *AIP Conf. Proc.* **2022**, *2454*.

[333] X. Zhang, X. Gao, K. Hong, J. Jiang, L. Zhang, J. Chen, Z. Rao, *J. Electroanal. Chem.* **2019**, *852*, 113525.

[334] G. Mercuri, G. Giambastiani, C. Di Nicola, C. Pettinari, S. Galli, R. Vismara, R. Vivani, F. Costantino, M. Taddei, C. Atzori, F. Bonino, S. Bordiga, B. Civalleri, A. Rossin, *Coord. Chem. Rev.* **2021**, *437*, 213861.

[335] D. Wu, J. J. Gassensmith, D. Gouveîa, S. Ushakov, J. F. Stoddart, A. Navrotsky, *J. Am. Chem. Soc.* **2013**, *135*, 6790.

[336] R. Sule, A. K. Mishra, T. T. Nkambule, *Int. J. Energy Res.* **2021**, *45*, 12481.

[337] J. J. Purewal, D. Liu, J. Yang, A. Sudik, D. J. Siegel, S. Maurer, U. Müller, *Int. J. Hydrogen Energy* **2012**, *37*, 2723.

[338] D. Zhao, X. Wang, L. Yue, Y. He, B. Chen, *Chem. Commun.* **2022**, *58*, 11059.

[339] N. Jiang, Z. Deng, S. Liu, C. Tang, G. Wang, *Korean J. Chem. Eng.* **2016**, *33*, 2747.

[340] I. A. Lázaro, *Eur. J. Inorg. Chem.* **2020**, *2020*, 4284.

[341] C. Healy, K. M. Patil, B. H. Wilson, L. Hermanspahn, N. C. Harvey-Reid, B. I. Howard, C. Kleinjan, J. Kolien, F. Payet, S. G. Telfer, P. E. Kruger, T. D. Bennett, *Coord. Chem. Rev.* **2020**, *419*, 213388.

[342] C. C. Wang, Z. L. Huang, Y. Y. Tseng, G. Bin Sheu, S. I. Lu, G. H. Lee, H. S. Sheu, *Crystals* **2020**, *10*, 1.

[343] V. V Butova, M. A. Soldatov, A. A. Guda, K. A. Lomachenko, C. Lamberti, *Russ. Chem. Rev.* **2016**, *85*, 280.

[344] X. Yan, K. Wang, X. Xu, S. Wang, Q. Ning, W. Xiao, N. Zhang, Z. Chen, C. Chen, *Inorg. Chem.* **2018**, *57*, 8033.

[345] Ó. Arnalds, F. Bartoli, P. Buurman, H. Óskarsson, G. Stoops, E. García-Rodeja, *Soils Volcan. Reg. Eur.* **2007**, 1.

[346] H. C. Dong, H. L. Nguyen, H. M. Le, N. Thoai, Y. Kawazoe, D. Nguyen-Manh, *Sci. Rep.* **2018**, *8*, 1.

[347] J. Jia, Y. Wang, M. Xu, M. li Qi, Y. Wu, G. Zhao, *J. Sol-Gel Sci. Technol.* **2020**, *93*, 123.

[348] G. D. Gilliland, *Photoluminescence Spectroscopy of Crystalline Semiconductors* **1997**.

[349] V. Villemot, M. Hamel, R. B. Pansu, I. Leray, G. H. V. Bertrand, *RSC Adv.* **2020**, *10*, 18418.

[350] X. Feng, F. Pan, P. Zhang, X. Wang, H. C. Zhou, Y. Huang, Y. Li, *ChemPhotoChem* **2021**, *5*, 79.

[351] S. Jensen, K. Tan, W. P. Lustig, D. S. Kilin, J. Li, Y. J. Chabal, T. Thonhauser, *Chem. Mater.* **2019**, *31*, 7933.

[352] H. Q. Xu, J. Hu, D. Wang, Z. Li, Q. Zhang, Y. Luo, S. H. Yu, H. L. Jiang, *J. Am. Chem. Soc.* **2015**, *137*, 13440.

ADVANCED
SCIENCE NEWS

www.advancedsciencenews.com

NANO · MICRO
small
www.small-journal.com

[353] J. G. Santaclara, A. I. Olivos-Suarez, I. Du Fossé, A. Houtepen, J. Hunger, F. Kapteijn, J. Gascon, M. A. Van Der Veen, *Faraday Discuss.* **2017**, *201*, 71.

[354] R. Nivetha, P. Kollu, K. Chandar, S. Pitchaimuthu, S. K. Jeong, A. N. Grace, *RSC Adv.* **2019**, *9*, 3215.

[355] G. Su, T. Feng, Z. Huang, Y. Zheng, W. Zhang, G. Liu, W. Wang, H. Wei, L. Dang, *Chem. Eng. J.* **2022**, *436*, 135119.

[356] Y. Hong, Y. Jiang, C. Li, W. Fan, X. Yan, M. Yan, W. Shi, *Appl Catal B* **2016**, *180*, 663.

[357] O. E. Barcia, S. Cattarin, E. D'Elia, I. Frateur, O. R. Mattos, M. Musiani, N. Pébère, B. Tribollet, *Electrochim. Acta* **2006**, *51*, 2096.

[358] M. E. Watson, W. & Orazem, Measurement model program. ECSArXiv, **n.d.**

[359] K. Wang, H. Wang, R. Bi, Y. Chu, Z. Wang, H. Wu, H. Pang, *Inorg. Chem. Front.* **2019**, *6*, 2873.

[360] C. Y. Tay, M. I. Setyawati, J. Xie, W. J. Parak, D. T. Leong, *Adv. Funct. Mater.* **2014**, *24*, 5936.

[361] X. Han, Y. Li, Y. Zhou, Z. Song, Y. Deng, J. Qin, Z. Jiang, *Mater. Des.* **2021**, *204*, 109646.

[362] B. R. Ware, *Adv. Colloid Interface Sci.* **1974**, *4*, 1.

[363] T. Liedl, S. Keller, F. C. Simmel, J. O. Rädler, W. J. Parak, *Small* **2005**, *1*, 997.

[364] T. Pellegrino, L. Manna, S. Kudera, T. Liedl, D. Koktysh, A. L. Rogach, S. Keller, J. Rädler, G. Natile, W. J. Parak, *Nano Lett.* **2004**, *4*, 703.

[365] L. Yu, Y. Lei, Y. Ma, M. Liu, J. Zheng, D. Dan, P. Gao, *Front. Phys.* **2021**, *9*, 644450.

[366] A. Ghosh, G. Das, *New J. Chem.* **2020**, *44*, 1354.

[367] W. Morris, B. Volosskiy, S. Demir, F. Gándara, P. L. McGrier, H. Furukawa, D. Cascio, J. F. Stoddart, O. M. Yaghi, *Inorg. Chem.* **2012**, *51*, 6443.

[368] Y. Chen, T. Hoang, S. Ma, *Inorg. Chem.* **2012**, *51*, 12600.

[369] F. Nouar, J. Eckert, J. F. Eubank, P. Forster, M. Eddaoudi, *J. Am. Chem. Soc.* **2009**, *131*, 2864.

[370] V. V. Krishnan, *Inventions* **2019**, *4*, 1.

[371] K. E. Haslauer, D. Hemmler, P. Schmitt-Kopplin, S. S. Heinzmann, *Anal. Chem.* **2019**, *91*, 11063.

[372] E. Brunner, M. Rauche, *Chem. Sci.* **2020**, *11*, 4297.

[373] K. Daicho, S. Fujisawa, K. Kobayashi, T. Saito, J. Ashida, *J. Wood Sci.* **2020**, *66*, 1.

[374] J. Tang, S. Li, Y. Su, Y. Chu, J. Xu, F. Deng, *J. Phys. Chem. C* **2020**, *124*, 17640.

[375] C. E. Hughes, P. A. Williams, K. D. M. Harris, *Angew. Chemie – Int. Ed.* **2014**, *53*, 8939.

[376] H. C. Hoffmann, M. Debowski, P. Müller, S. Paasch, I. Senkovska, S. Kaskel, E. Brunner, *Materials (Basel)* **2012**, *5*, 2537.

[377] C. L. Jones, C. E. Hughes, H. H. M. Yeung, A. Paul, K. D. M. Harris, T. L. Easun, *Chem. Sci.* **2021**, *12*, 1486.

[378] S. ur Rehman, S. Xu, H. Xu, T. Tao, Y. Li, Z. Yu, K. Ma, W. Xu, J. Wang, *Mater. Today Adv.* **2022**, *16*, 100287.

[379] F. Bonino, C. Lamberti, S. Bordiga, *Chem. Met. Fram. Synth. Charact. Appl.* **2016**, 657.

[380] M. R. Ryder, B. Civalleri, T. Bennett, S. Henke, S. Rudić, G. Cinque, F. Fernandez-Alonso, J. C. Tan, *Phys. Rev. Lett.* **2014**, *113*, 1.

[381] F. Formalik, A. V. Neimark, J. Rogacka, L. Firlej, B. Kuchta, *J. Colloid Interface Sci.* **2020**, *578*, 77.

[382] M. M. Beasley, E. J. Bartelink, L. Taylor, R. M. Miller, *J Archaeol Sci* **2014**, *46*, 16.

[383] K. Hashimoto, V. R. Badarla, A. Kawai, T. Ideguchi, *Nat. Commun.* **2019**, *10*, 1.

[384] H. G. M. Edwards, *Modern Raman Spectroscopy—a Practical Approach.Ewen Smith and Geoffrey Dent*, John Wiley and Sons Ltd, Chichester **2005**, p. 210.

[385] S. Li, Z. Jiang, X. Xiao, W. Chen, X. Tian, X. Hao, Z. J. Jiang, *Ionics (Kiel)* **2019**, *25*, 785.

[386] J. Wang, Z. Wu, L. Han, R. Lin, W. Xiao, C. Xuan, H. L. Xin, D. Wang, *J. Mater. Chem. A* **2016**, *4*, 5678.

[387] S. Sohrabi, S. Dehghanpour, M. Ghalkhani, *J. Mater. Sci.* **2018**, *53*, 3624.

[388] Y. Liu, C. Wang, S. Ju, M. Li, A. Yuan, G. Zhu, *Prog. Nat. Sci.: Mater. Int.* **2020**, *30*, 185.

[389] P. George, R. K. Das, P. Chowdhury, *Microporous Mesoporous Mater.* **2019**, *281*, 161.

[390] B. Wang, J. Shang, C. Guo, J. Zhang, F. Zhu, A. Han, J. Liu, *Small* **2019**, *15*, 1.

[391] D. O. Miles, D. Jiang, A. D. Burrows, J. E. Halls, F. Marken, *Electrochem. Commun.* **2013**, *27*, 9.

[392] L. Liu, F. Yan, K. Li, C. Zhu, Y. Xie, X. Zhang, Y. Chen, *J. Mater. Chem. A* **2019**, *7*, 1083.

[393] J. Noh, Y. Kim, H. Park, J. Lee, M. Yoon, M. H. Park, Y. Kim, M. Kim, *J Ind Eng Chem* **2018**, *64*, 478.

[394] Y. Li, Y. Lin, J. Guo, Z. Xu, B. Wang, T. Zhu, *Environ. Sci. Pollut. Res.* **2022**, *29*, 26599.

[395] K. Li, J. Jiang, *SN Appl Sci* **2021**, *3*, 1.

[396] Y. Chen, S. Li, S. Lv, Y. Huang, *Catal. Commun.* **2021**, *149*, 106215.

[397] Y. Xue, Y. Guo, Q. Zhang, Z. Xie, J. Wei, Z. Zhou, *Nano-Micro Lett.* **2022**, *14*, 1.

[398] K. Kim, K. J. Lopez, H. J. Sun, J. C. An, G. Park, J. Shim, *J. Appl. Electrochem.* **2018**, *48*, 1231.

[399] J. Zhang, Q. Kong, D. Y. Wang, *J. Mater. Chem. A* **2018**, *6*, 6376.

[400] C. Zhao, P. Li, D. Shao, R. Zhang, S. Wang, Z. Zhu, C. Zhao, *Int. J. Hydrogen Energy* **2019**, *44*, 844.

[401] M. V. Kharlamova, C. Kramberger, *Nanomaterials* **2022**, *12*, 42.

[402] R. Elzein, C. M. Chang, I. Ponomareva, W. Y. Gao, S. Ma, R. Schlaf, *ACS Appl. Mater. Interfaces* **2016**, *8*, 31403.

[403] M. M. Beerbom, B. Lägel, A. J. Cascio, B. V. Doran, R. Schlaf, *J Electron Spectros Relat Phenomena* **2006**, *152*, 12.

ADVANCED
SCIENCE NEWS

www.advancedsciencenews.com

NANO · MICRO

small

www.small-journal.com

Amir Farokh Payam is an assistant professor at the Ulster University, UK. His undergraduate and graduate training was undertaken at K. N. Toosi University of Technology, Isfahan University of Technology, and University of Tehran, followed by doctoral/postdoctoral periods at Instituto de Microelectronica de Madrid and Instituto de Ciencia de Materiales de Madrid (ICMM-CSIC), where he worked in Professor Ricardo Garcia's group, Durham University in Professor Kislon Voitchovsky's group and University of Bristol in the solid mechanics group under supervision of Prof David Knowles. His research interests span nanotechnology, materials characterization and surface science, advanced atomic force microscopy, MEMS/NEMS, and sensors.

Sameh Khalil commenced his academic journey at Zagazig University in Egypt, where he graduated with a first-class honors degree in 2012. He then earned his M.Sc. from the same university and was awarded the best thesis in Advanced Engineering Science and Technology, 2017 with the guidance of Prof Ashraf Ali. Currently, Sameh is a Ph.D. Researcher at the School of Engineering, Ulster University. Under the supervision of Dr. Supriya Chakrabarti, he is exploring novel nanoporous structures for efficient solar energy harvesting.

Supriya Chakrabarti is an assistant professor at the School of Engineering, Ulster University, UK. He obtained his B.Sc. and M.Sc. degrees in Physics from Jadavpur University, India in 1998 and 2000, respectively. He completed his Ph.D. in Materials Science from the Indian Association for the Cultivation of Science in 2004. As a postdoctoral fellow, he joined Prof. Yoshikazu Nakayama's group in Japan and worked for Osaka Prefecture University & Osaka Science and Technology Centre (2005–2008), after that he moved to the United States in 2008 and collaborated as a postdoctoral researcher with Prof. Liming Dai, Prof. Vesselin Shanov, and Prof. Mark J Schulz. He also collaborated with Prof. Davide Mariotti, Ulster University as a research associate from 2015 to 2017. His current research interests focus on the synthesis and functionalization of nanomaterials, e.g., carbon nanostructures, graphene, metal oxides, metal–organic frameworks, and derivatives for various applications in clean energy, biomedical technology, sensors, opto-electronic devices, catalysis, and water treatment for providing sustainable engineering solutions to the society.